NASA Technical Paper 2973

1990

Static Investigation of a Two-Dimensional Convergent-Divergent Exhaust Nozzle With Multiaxis Thrust-Vectoring Capability

John G. Taylor
Langley Research Center
Hampton, Virginia

National Aeronautics and Space Administration
Office of Management
Scientific and Technical Information Division

Summary

An investigation was conducted in the static test facility of the Langley 16-Foot Transonic Tunnel to determine the internal performance of two-dimensional convergent-divergent nozzles designed to have simultaneous pitch and yaw thrust-vectoring capability. This concept utilized divergent flap rotation for thrust vectoring in the pitch plane and deflection of flat yaw flaps hinged at the end of the sidewalls for yaw thrust vectoring. The hinge location of the yaw flaps was varied at four positions from the nozzle exit plane to the throat plane. The yaw flaps were designed to contain the flow laterally independent of power setting. In order to eliminate any physical interference between the yaw flap deflected into the exhaust stream and the divergent flaps, the downstream corners of both upper and lower divergent flaps were cut off to allow for up to 30° of yaw-flap deflection. This investigation studied the impact of varying the nozzle pitch vector angle, throat area, yaw-flap hinge location, yaw-flap length, and yaw-flap deflection angle on nozzle internal performance characteristics. High-pressure air was used to simulate the jet exhaust at nozzle pressure ratios up to 7.0.

Static results indicated that configurations with the yaw-flap hinge located upstream of the exit plane provided relatively high levels of thrust-vectoring efficiency without causing large losses in resultant thrust ratio. Therefore, these configurations represent a viable concept for providing simultaneous pitch and yaw thrust vectoring.

Introduction

Mission requirements for the next-generation fighter will probably require future combat aircraft to have short takeoff and landing characteristics in order to operate from bomb-damaged runways and to be able to cruise at supersonic speeds. These future aircraft will probably also possess an increased level of maneuverability at transonic and supersonic speeds and be able to operate at higher angles of attack than current fighters. Several investigations have shown that significant advantages in air combat are gained with the ability to perform transient maneuvers at high angles of attack including brief excursions into post-stall conditions (low speed, high angle of attack). (See refs. 1 to 3.) However, maneuverability at high angles of attack can be limited because of degraded stability characteristics and inadequate aerodynamic control power.

One method of providing large control moments that do not decrease at post-stall angles of attack (as do moments generated by aerodynamic controls) is vectoring of the engine exhaust. Studies have shown that the control power provided by 15° of simultaneous pitch and yaw thrust vectoring can significantly enhance aircraft agility in the stall and below-stall angle-of-attack range (refs. 4 to 6). Since thrust vectoring provides control moments that are essentially uncoupled from airframe aerodynamics, its use might allow for an increase in control power or a reduction in (or elimination of) the aerodynamic control surfaces and, therefore, a reduction in aircraft weight and drag.

Several research programs at the NASA Langley Research Center have shown that thrust vectoring can be provided from nonaxisymmetric multifunction nozzles. Most of the early research focused on vectoring of the thrust in the longitudinal plane of the nozzle. (See the discussion of pitch vectoring in refs. 7 to 12.) Several recent investigations have included lateral thrust-vectoring (yaw-vectoring) concepts in addition to pitch thrust vectoring (refs. 13 to 18). One of several nonaxisymmetric nozzles that have been modified for thrust vectoring is the two-dimensional convergent-divergent (2-D C-D) nozzle.

Internal contours of a 2-D C-D nozzle provide for compression and expansion of the flow with upper and lower convergent and divergent flaps, respectively. Nozzle sidewalls are flat internally and restrain the flow in the lateral plane until they terminate, usually at the nozzle exit plane. Typically, the upper and lower divergent flaps are rotated in the same direction to provide vectoring of the thrust in the pitch plane. Without some modifications, however, yaw thrust vectoring using the sidewalls is not as simple; deflection of the sidewalls about some vertical hinge would cause interference with the upper and lower divergent flaps. In order to avoid this interference, one investigation has studied flat yaw vanes attached to the nozzle sidewalls at the exit plane (extending downstream) and deflected into and away from the exhaust about a vertical hinge at the end of the sidewalls. This concept was called post-exit vanes and has been reported in reference 17. Another yaw-vectoring concept used the internal geometry of the nozzle at dry power (maximum nonaugmented), low expansion ratio, and forward-thrust conditions to size yaw flaps installed in the sidewalls and deflected about a hinge at the nozzle throat plane. These yaw flaps were flush with the sidewalls when stowed, and when deployed they were deflected symmetrically into and out of the exhaust stream (referred to as the downstream yaw-flap concept in ref. 13).

The post-exit vane concept generated thrust vector angles up to 70 percent of the yaw-vane deflection angle, but deflection of these vanes mounted at the nozzle exit plane caused large losses in

resultant thrust ratio (up to a 1-percent loss per degree of resultant yaw vector angle). These large thrust losses were attributed to the location of the vanes which were turning supersonic flow. The downstream yaw-flap concept generated large thrust vector angles without causing large losses in resultant thrust ratio. However, increasing the expansion ratio (nozzle exit area) and/or power setting (throat area) decreased the efficiency and effectiveness of this concept. Since the flaps were sized to be deployed between the divergent flaps and fully contain the flow at dry power, low-expansion-ratio conditions, increasing the throat and/or exit area allowed some internal flow to pass over and under the yaw flap deflected into the exhaust without being turned. Additionally, the flap deflected into the internal flow could not be deployed when the divergent flaps were pitch vectored because of physical interference. Therefore, this concept did not represent a viable multiaxis (combined pitch and yaw) thrust-vectoring concept.

Employing lessons learned from these two previous studies, a simultaneous pitch and yaw thrust-vectoring concept has been investigated in the static test facility of the Langley 16-Foot Transonic Tunnel. This concept utilized divergent flap rotation for thrust vectoring in the pitch plane and deflection of flat yaw flaps hinged at the end of the sidewalls for yaw thrust vectoring. The hinge location of the yaw flaps was varied at four positions from the exit plane of the nozzle (similar to the post-exit vane concept of ref. 17) to the throat plane (similar to the downstream flap concept of ref. 13). However, the yaw flaps were not sized to be deflected between the divergent flaps, but instead they were designed to contain the flow laterally independent of operating conditions. In order to eliminate any physical interference between the yaw flap deflected into the exhaust stream and the divergent flaps, the downstream corners of both upper and lower divergent flaps were cut off to allow for up to 30° of yaw-flap deflection. This divergent flap cutout was necessary for hinge locations upstream of the exit plane and for the lower divergent flaps on the pitch-vectored nozzles for the hinge location at the exit plane. This investigation studied the impact of varying the nozzle pitch vector angle, throat area, yaw-flap hinge location, yaw-flap length, and yaw-flap deflection angle on nozzle internal performance characteristics. High-pressure air was used to simulate the jet exhaust at nozzle pressure ratios up to 7.0, and there was no external flow (the Mach number was 0).

Symbols

All forces (with the exception of resultant gross thrust) and all resultant thrust vector angles are referred to the model centerline (body axis). A detailed discussion of the data reduction and calibration procedures can be found in references 19 and 20. Definitions of forces, angles, and propulsion relationships used in this report can be found in reference 20.

AR	measured nozzle throat aspect ratio, w_t/h_t
A_e	nominal nozzle exit area, in^2
A_e/A_t	nozzle expansion ratio
A_t	measured nozzle throat area, in^2
C_d	nozzle discharge coefficient, w_p/w_i
F	measured thrust along body axis, lbf
F/F_i	internal thrust ratio
F_i	ideal isentropic gross thrust, lbf, $w_p\sqrt{\frac{2\gamma R_j}{(\gamma-1)g}}\sqrt{(T_{t,j}+459.67)\left[1-\left(\frac{1}{\mathrm{NPR}}\right)^{\frac{\gamma-1}{\gamma}}\right]}$
F_N	measured normal force, lbf
F_r	resultant gross thrust, $\sqrt{F^2+F_N^2+F_S^2}$, lbf
F_r/F_i	resultant thrust ratio
F_S	measured side force, lbf
g	acceleration due to gravity ($1g \approx 32.174$ ft/sec^2)
h_e	nominal nozzle exit height, in.
h_t	nominal nozzle throat height, in.
l_s	axial length from nozzle throat to exit station (fig. 2)
l_y	length of yaw flap (figs. 3 and 5), in.
NPR	nozzle pressure ratio, $p_{t,j}/p_a$
$(\mathrm{NPR})_d$	design nozzle pressure ratio (NPR for fully expanded flow at nozzle exit)
p_a	atmospheric pressure, psi
$p_{t,j}$	jet total pressure, psi
R_j	jet gas constant, 53.3643 ft/°R
$T_{t,j}$	jet total temperature, °F
w_i	ideal weight-flow rate, lbf/sec, $A_t p_{t,j}\left(\frac{2}{\gamma+1}\right)^{\frac{\gamma+1}{2(\gamma-1)}}\sqrt{\frac{\gamma g}{R_j(T_{t,j}+459.67)}}$
w_p	measured weight-flow rate, lbf/sec
w_t	nominal nozzle throat width, 4.0 in.

x_e axial distance from nozzle connect station to nozzle exit (fig. 2), 4.55 in.

x_s axial distance from nozzle connect station to yaw-flap hinge location (also where sidewalls end and divergent flap cutout begins (fig. 2)), in.

x_t axial distance from nozzle connect station to nozzle throat (fig. 2), in.

γ ratio of specific heats, 1.3997 for air

δ_p resultant pitch thrust vector angle, $\tan^{-1}\frac{F_N}{F}$, deg

δ_r resultant thrust vector angle due to combined pitch and yaw thrust vectoring, $\sqrt{\delta_p^2+\delta_y^2}$, deg

$\delta_{v,p}$ geometric pitch vector angle measured from model centerline (positive for downward deflection angles), based on average rotation of upper and lower flaps, deg

$\delta_{v,y}$ geometric yaw vector angle, flap deflection about hinge location (positive to left looking upstream), deg

δ_y resultant yaw thrust vector angle, $\tan^{-1}\frac{F_S}{F}$, deg

$\eta_{r_{\delta_r}}$ vectoring performance-effectiveness parameter for simultaneous pitch and yaw thrust vectoring, $[(F_r/F_i)_{\text{unvectored}}-(F_r/F_i)_{\text{vectored}}]/\delta_r$, per degree

$\eta_{r_{\delta_y}}$ vectoring performance-effectiveness parameter for yaw thrust vectoring, $[(F_r/F_i)_{\text{unvectored}}-(F_r/F_i)_{\text{vectored}}]/|\delta_y|$, per degree

Abbreviations:

A/B afterburning

approx. approximate

Conf. configuration

Conv. convergent

Div. divergent

Sta. model station, in.

2-D C-D two-dimensional convergent-divergent

Apparatus and Methods

Description of Static Test Facility

Model testing was conducted in the static test facility of the Langley 16-Foot Transonic Tunnel (ref. 19). The model was located in a large room where the jet exhaust from a simulated single-engine propulsion system was vented to the atmosphere. This facility utilized the same clean, dry air supply as that used in the 16-Foot Transonic Tunnel and a similar air control system, which included valving, filters, and a heat exchanger (used to maintain a constant temperature in the high-pressure plenum). (See fig. 1(a).) A remotely located control room contained the controls for the airflow valves and a closed-circuit television to observe the model when the jet was operating.

Single-Engine Propulsion Simulation System

A sketch is presented in figure 1(a) of the single-engine air-powered nacelle model on which the various nozzle configurations with pitch and yaw thrust-vectoring capability were tested. A photograph of the propulsion simulation system is shown in figure 1(b) with a typical unvectored, dry power 2-D C-D configuration installed.

An external high-pressure air system provided a continuous flow of clean, dry air at a controlled temperature of approximately 85°F. The pressure was varied during jet simulation to provide a nozzle pressure ratio up to 7.0 (or until balance limits were reached). The model was secured on a dolly mounted support strut through which the pressurized air was routed. The air traveled through tubing in the strut into a high-pressure plenum chamber. From there the air was discharged perpendicularly into the low-pressure plenum through eight multiholed, equally spaced sonic nozzles located around the high-pressure plenum. (See fig. 1(a).) This airflow system was designed to minimize any forces incurred during the transfer of axial momentum as the air is passed from the nonmetric (not on the balance) high-pressure plenum to the metric (on the balance) low-pressure plenum. A pair of flexible metal bellows (shown in fig. 1(c)) sealed the air system between the metric and nonmetric parts of the model and compensated for any axial force caused by pressurization. The low-pressure air then passed from the circular low-pressure plenum through a circular-to-rectangular transition section, a multiple-orifice rectangular choke plate (flow straightener), and a rectangular instrumentation section, which was common for all nozzle models tested. The instrumentation section was common in geometry to the nozzle airflow entrance (nozzle connect section). All nozzle configurations were attached to the instrumentation section at model station (Sta.) 41.13.

Nozzle Design

At unvectored conditions, 2-D C-D nozzles consist of two pairs of symmetric upper and lower flaps. The flow is compressed and accelerated at subsonic speeds by the convergent flaps. Once the flow is choked at the throat, it is expanded by the divergent flaps. At the design nozzle pressure ratio $(NPR)_d$, the flow is fully expanded at the exit plane of the nozzle. (The static pressure at the exit is equal to the ambient static pressure.) The sidewalls are flat and contain the flow laterally. To achieve positive thrust vectoring in the pitch plane, the divergent flaps are rotated downward (the upper flap toward the nozzle centerline). A schematic of a typical 2-D C-D nozzle in the forward-thrust (no pitch) and positive pitch thrust-vectored modes is shown in figure 2(a).

Four baseline nozzle configurations were tested. Two of the baseline nozzles simulated a dry power setting and two represented afterburning (A/B) power. Both forward-thrust (no pitch) and pitch thrust-vectored modes were examined for each power setting. The forward-thrust ($\delta_{v,p} = 0°$) dry power baseline nozzle used in the current test (fig. 2(b)) had previously been investigated. (See refs. 12 (configuration C1) and 13 (configuration S1).) The pitch thrust-vectored baseline nozzle shown in figure 2(c) had not been previously tested. It was designed using the geometry of the forward-thrust nozzle and assumed a constant length from the center of flap rotation at the throat plane to the trailing edge of the divergent flap. (See fig. 2(a).) Using the geometry of the forward-thrust nozzle, this line was rotated downward 20° from its original inclination to the horizontal. Because of the design of the flap, a nominal deflection of 20° caused the upper divergent flap to be rotated downward by 19.33° and the lower divergent flap to be rotated downward by 19.73° from the common starting divergence angle of 1.17°. (Note that the divergent flap length changed.) The average of these rotations resulted in a geometric pitch vector angle $\delta_{v,p}$ of 19.53°.

The A/B power baseline nozzle ($\delta_{v,p} = 0°$) had also been investigated previously with nozzle internal performance reported in references 10 (configuration A1) and 13 (configuration S9). The geometry for this nozzle is presented in figure 2(d). Similarly, the geometry for the A/B pitch thrust-vectored baseline nozzle ($\delta_{v,p} = 20.26°$) is given in figure 2(e). The nozzle internal performance for this configuration is documented in references 10 (configuration A1V20) and 13 (configuration S15). All four of the baseline nozzles had full divergent flaps and sidewalls that ended at the (unvectored) nozzle exit plane, that is, $(x_s - x_t)/l_s = 1.00$. The reduction in measured throat area from the forward-thrust nozzles to the pitch-vectored nozzles (dry and A/B power) was caused by changes in the nozzle internal geometry due to rotation of the divergent flaps. As noted in figures 2(b) to 2(e), each baseline nozzle geometry had three derivatives corresponding to the three hinge locations upstream of the exit plane. This was necessary because of the varying amount of divergent flap cutout associated with each hinge location.

In this investigation, thrust vectoring in the yaw plane was accomplished by deflecting full-sidewall-height yaw flaps about a vertical hinge line. As shown in figure 3, one flap was vectored into the internal exhaust flow and the other flap was vectored the same amount away from the exhaust. The yaw flaps were tested at four hinge locations illustrated in figure 4, starting at the nozzle exit (Sta. 45.68) and progressing upstream in equal increments. The nondimensional term $(x_s - x_t)/l_s$ describes this yaw-flap hinge location as a percentage of the nozzle divergent flap length, where $(x_s - x_t)/l_s = 1.00$ denotes the hinge at the nozzle exit, $(x_s - x_t)/l_s = 0$ denotes the hinge at the throat plane of the dry power $\delta_{v,p} = 0°$ baseline nozzle, and the other two values (0.67 and 0.33) denote locations between the exit and the throat. Although the axial positions of the four hinge locations (x_s) were fixed throughout the test, the A/B power nozzles had a different throat location ($x_t = 2.35$ in. as seen in fig. 2(d)). The difference in throat location caused a change in the value of l_s because the exit plane location was fixed. Therefore, the values of hinge location for the A/B power nozzles are slightly different from the values for the dry power nozzles. (See fig. 4.) For the A/B power nozzles, the values of hinge location were $(x_s - x_t)/l_s = 1.00, 0.66, 0.31$, and -0.03. A hinge location of -0.03 implies that the hinge is located just upstream of the throat plane.

In order to allow for yaw-flap deflection at the three hinge locations upstream of the exit plane, portions of both upper and lower divergent flaps had to be cut out (fig. 4). This cutout was made on both sides of the upper and lower flaps to allow for both positive and negative yaw vector angles. The cutout started at the edge of the upper and lower flaps where the yaw-flap hinge was located (at the end of the sidewall) and ended at the exit plane. Enough divergent flap was removed to allow for a maximum of 30° of yaw-flap deflection in either direction at both forward-thrust and pitch thrust-vectored conditions. (It is important to note that the cutout, once designed into a full-scale nozzle, would not vary. The aircraft would always fly with this divergent flap cutout, and the yaw-flap length would remain fixed. Installed performance studies would be

required to fix the yaw-flap hinge location and flap length.)

Three different lengths of sidewall yaw flaps were used in this investigation (fig. 5), the longest of which was equal to the axial length from the throat to the exit plane of the dry power baseline nozzle (l_y = 2.27 in.). (In this case, l_y/l_s = 1.00 for dry power, and 1.03 for A/B power.) The second and third sets were two-thirds (l_y/l_s = 0.67 for dry power and 0.69 for A/B power) and one-third (l_y/l_s = 0.33 for dry power and 0.34 for A/B power) the length of the long set, respectively. Each of these three different sets of yaw flaps could be vectored at yaw angles of 0°, −20°, and −30°. Not all yaw flaps were tested at each hinge location. Table I shows the combinations of yaw-flap hinge location, flap length, and flap deflection angle for which data are available.

Figure 6(a) shows photographs of four dry power nozzle configurations with the same yaw-flap length (l_y/l_s = 0.67 and $\delta_{v,y}$ = 0°) installed at the four different hinge locations. Sketches of these configurations are presented in figure 6(b) and are typical of sketches used throughout the data presentation to aid the reader in recognizing the yaw-flap hinge location, flap length, and flap deflection angle. Figure 7 shows photographs of some typical yaw-vectoring configurations with the trailing edge of the yaw flaps ending at the exit plane. Three hinge locations and yaw-flap lengths are shown.

Instrumentation

The weight-flow rate of the high-pressure air supplied to the model was determined from temperature and pressure measurements in the high-pressure plenum and was calibrated with standard axisymmetric nozzles. (See ref. 21.) Nine total-pressure probes were attached to three rakes located in the instrumentation section. A thermocouple was also positioned in the instrumentation section to measure the jet total temperature. (See fig. 1(a).) An area-weighted average of the nine jet total-pressure measurements was used for the jet total pressure. Measured values of the temperature and pressure in the instrumentation section, along with the measured throat area, were used to compute the ideal weight-flow rate. Details of the measured and ideal weight-flow rate calculations can be found in reference 20.

A six-component strain-gauge balance was used to measure the forces and moments on the model downstream of station 20.50. The balance-moment reference center was located at station 26.54. The accuracy of force balance readings is quoted at ±0.5 percent of full-scale values. The full-scale values for the balance used in this investigation are as follows: axial force, 500 lb; normal force, ±500 lb; and side force, ±350 lb.

Data Reduction

All data were recorded on magnetic tape and taken in ascending order of $p_{t,j}$. Fifty frames of data, taken at a rate of 10 frames per second, were used to compute an average steady-state value for each data point. The basic performance parameters used in the presentation of results were internal thrust ratio F/F_i, resultant thrust ratio F_r/F_i, resultant pitch thrust vector angle δ_p, resultant yaw thrust vector angle δ_y, and discharge coefficient C_d.

The internal thrust ratio F/F_i is the ratio of measured nozzle thrust along the body axis to ideal thrust, where ideal thrust is based upon measured weight-flow rate w_p, jet total temperature $T_{t,j}$, and nozzle pressure ratio NPR. The balance axial-force measurement, from which the actual nozzle thrust F is subsequently obtained, is initially corrected for balance interactions. Although the bellows arrangement was designed to eliminate pressure and momentum interactions with the balance, small bellows tares on the six balance components still exist. These tares result from a small pressure difference between the ends of the bellows when internal velocities are high and from small differences in the spring constants of the forward and aft bellows when the bellows are pressurized. These bellows tares were determined by testing standard axisymmetric calibration nozzles with known performance over a range of expected longitudinal and lateral forces and moments. The balance data were then corrected in a manner similar to that discussed in reference 7 to obtain thrust along the body axis F, normal force F_N, and side force F_S. The resultant thrust ratio F_r/F_i, resultant pitch vector angle δ_p, and resultant yaw vector angle δ_y were then determined from these corrected balance data. A more detailed discussion of the data reduction process can be found in references 19 and 20.

The resultant thrust ratio F_r/F_i is the resultant gross thrust divided by the ideal isentropic gross thrust. Resultant gross thrust is obtained from the measured axial (thrust along the body axis), normal, and side components of the jet resultant force. As long as the exhaust flow is unvectored in either the longitudinal or lateral direction, F/F_i and F_r/F_i are equal. From the definitions of F and F_r, it is obvious that the thrust along the body axis F includes losses that result from turning the thrust vector away from the axial direction, whereas the resultant gross thrust F_r does not. The losses included in both thrust terms F and F_r are caused by friction and pressure drags associated with the

thrust-vectoring hardware. Resultant thrust vector angles in the longitudinal (pitch) plane δ_p and the lateral (yaw) plane δ_y are presented for evaluating the exhaust-flow turning capability of the various thrust-vectored nozzle configurations.

The nozzle discharge coefficient C_d is the ratio of measured weight-flow rate to ideal weight-flow rate, where ideal weight-flow rate is dependent upon jet total pressure $p_{t,j}$, jet total temperature $T_{t,j}$, and measured nozzle throat area A_t. The nozzle discharge coefficient reflects the ability of a nozzle to pass weight flow and is reduced by any momentum and vena contracta losses (ref. 22).

In order to compare the results from the current investigation with the results obtained from previous investigations, several thrust-vectoring performance-effectiveness parameters defined in reference 16 were used. These parameters, $\eta_{r_{\delta_y}}$ (for pure yaw thrust-vectoring concepts) and δ_r and $\eta_{r_{\delta_r}}$ (for simultaneous pitch and yaw thrust-vectoring concepts), were computed from data obtained as close to $(\mathrm{NPR})_d$ as possible. They serve as figures of merit by indicating the effectiveness of a thrust-vectoring concept; that is, they provide a value for the loss in resultant thrust ratio per degree of resultant thrust vector angle.

Presentation of Results

A list of configurations along with an index to the internal performance data figures are contained in table I. Performance comparisons are presented in the following figures:

Results and Discussion

Baseline Nozzles

The basic data for the four baseline nozzles (dry and A/B power, both forward-thrust and pitch thrust-vectored modes) are presented in figure 8. The internal thrust ratio, resultant thrust ratio (for the pitch-vectored nozzles only), discharge coefficient, resultant pitch thrust vector angle, and resultant yaw thrust vector angle are shown as a function of nozzle pressure ratio. The peak thrust performance of the forward-thrust dry power nozzle (see fig. 8(a)) occurred near a design nozzle pressure ratio of 3.0 ($(\mathrm{NPR})_d = 2.98$). Recall that the design nozzle pressure ratio is the nozzle pressure ratio for fully expanded flow inside the nozzle. As mentioned earlier, the forward-thrust dry power baseline nozzle had been tested previously (refs. 12 and 13). Results of the current investigation are compared with those of reference 13 in figure 8(a). Results from reference 12 are similar. The discharge coefficient is slightly higher than previous values but is generally within 0.7 percent. (Accuracy is typically within ±0.5 percent.) The internal thrust ratio duplicated earlier data. As expected, both resultant thrust vector angles (δ_p and δ_y) remain near 0° over the range of nozzle pressure ratio tested.

The internal performance data for the dry power pitch-vectored baseline nozzle are presented in figure 8(b). (Note that this baseline had not previously

been tested.) The peak of the resultant thrust ratio curve occurred between a nozzle pressure ratio of 4.0 and 5.0 ($(NPR)_d$ = 4.42). A comparison of these two baseline nozzles (vectored and unvectored) shows less than a 0.5-percent decrease in peak resultant thrust ratio because of turning losses associated with pitch vectoring. (For the forward-thrust nozzle, the internal thrust ratio equals the resultant thrust ratio.) Static pressure data from several earlier investigations on pitch thrust-vectored 2-D C-D nozzles have shown that the throat plane rotates from the unvectored position to a location where it is nearly perpendicular to the upper divergent flap, where the minimum geometric cross-sectional area occurs. (See the geometry in fig. 2 and also see refs. 7 and 11.) Consequently, the internal flow is turned at subsonic speeds which proves to be efficient, as can be seen by the small loss in peak resultant thrust ratio between these two nozzles.

At low nozzle pressure ratios, the resultant pitch vector angle for the dry power pitch-vectored baseline nozzle is higher than the design pitch vector angle of 19.53°. Overturning at low nozzle pressure ratios is typical of pitch thrust-vectored 2-D C-D nozzles at dry power operating conditions. This turning angle decreases with increasing pressure ratio to values below the design ("metal") angle. As noted in reference 10, this change in thrust angularity with increasing nozzle pressure ratio is common in nonaxisymmetric nozzles whenever one flap is longer than the other with respect to the flow centerline. (See fig. 2(c).) This difference in flap length provides surfaces of unequal length for the flow to expand upon so that one side of the internal flow is contained longer by a flap while the other side of the exhaust flow is unbounded.

There was a 1.5-percent decrease in discharge coefficient due to pitch vectoring the dry power nozzle from 0° to 19.53°. These losses are associated with changes in throat position when the nozzle was pitch vectored.

Both A/B power baseline nozzles had been tested previously, and their internal performance is documented in references 10 and 13. Because of limitations on the force balance, data were not obtained for values of NPR at and above peak performance levels. The internal performance of the A/B power forward-thrust baseline nozzle is presented in figure 8(c) and compared with results from reference 13. Although $(NPR)_d = 4.54$ for this nozzle, data presented at the maximum NPR of 4.5 do not indicate that the performance peak has been attained. In fact, results from reference 13 indicate that peak performance occurred at NPR = 5.0. Results from the current investigation for internal thrust ratio and discharge coefficient agree with those of reference 13. As expected, both resultant thrust vector angles remain near 0° for the NPR range tested.

The internal performance of the A/B power pitch-vectored baseline nozzle is compared with results from reference 10 in figure 8(d). Data below NPR = 4.0 are similar, but slight differences occur in F/F_i, F_r/F_i, and δ_p for the data points above NPR = 4.0. As discussed in reference 10, this nozzle experiences flow separation on the lower divergent flap at nozzle pressure ratios below design ($(NPR)_d$ = 6.33), and reattachment (which occurs between NPR = 3.5 and 4.0) of the exhaust to the lower flap did not occur at the same pressure ratio as before. A difference of approximately 1 percent in F/F_i and 1° in δ_p can be seen in figure 8(d). It is likely that this flow separation on the lower divergent flap at a low NPR is caused in part by the large angle that the flow is turned on the lower flap. As the pressure gradient increases between the upper and lower divergent flaps with increasing NPR (see ref. 10), the internal flow is forced to turn more in the direction of the lower divergent flap surface. Between an NPR of 3.5 and 4.0, the flow reattaches to the lower flap resulting in larger turning angles. This reattachment causes a large drop in F/F_i (over 5 percent) because the exhaust flow is being turned farther away from the axial direction. Concurrently, there is an increase of 7° in δ_p. As expected, resultant yaw vector angles remain near 0° over the range of pressure ratios tested.

Effects of Divergent Flap Cutout

The effects of divergent flap cutout on nozzle internal performance for forward-thrust and pitch thrust-vectored nozzles are presented in figures 9(a) and 9(b) for dry power configurations and in figures 9(c) and 9(d) for A/B power configurations. The hinge location has been successively moved back to the throat while holding the yaw-flap trailing edge at the exit such that $[(x_s - x_t)/l_s] + l_y/l_s = 1.00$. (See the symbol key in fig. 9.) Note that the yaw flaps were undeflected.

Dry power nozzles. As discussed previously, hinge locations upstream of the exit plane required a cutout of the downstream corners of the divergent flaps for yaw-vectoring capability. Moving the hinge back to $(x_s - x_t)/l_s = 0.33$ had no effect on nozzle internal thrust performance. However, locating the hinge at the throat ($(x_s - x_t)/l_s = 0$) resulted in a 0.5-percent loss in internal thrust ratio near the baseline $(NPR)_d$ of 2.98. This loss in thrust ratio increases as nozzle pressure ratio increases and is due to a portion of the exhaust flow expanding through the

cutout in the divergent flaps (less efficiently). Moving the hinge back to the throat (denoted by triangular symbols) also resulted in a decrease in the effective expansion ratio A_e/A_t since the peak performance is occurring at a lower nozzle pressure ratio. Therefore, at higher values of NPR, this configuration is also experiencing increased underexpansion losses because it is operating farther from the design nozzle pressure ratio. These results are similar to those of reference 23 for an axisymmetric convergent-divergent nozzle with slots in the divergent flaps. It is important to note that these forward-thrust configurations represent the nozzle position during cruise (which is generally the majority of an aircraft flight profile). As always, performance/weight trades exist, and the adverse effect of a small loss in thrust ratio (as measured for the largest cutout) due to divergent flap cutout might be offset by a decrease in the nozzle weight and internal nozzle surface area to be cooled.

A decrease in discharge coefficient of 0.6 percent can be seen from the baseline (circular symbols) to configurations with divergent flap cutout (yaw flaps hinged upstream of the exit). It is not understood what caused this decrease in C_d, but two possible reasons are presented below. The decrease in C_d might be due to a small change in geometry upstream of the nozzle throat in the convergent region of the nozzle. Evidence of this can be seen in the repeatability of data for the three configurations with increasing divergent flap cutout. However, removal of the downstream corners of the divergent flaps might have also affected C_d by altering the position and, therefore, the area of the throat.

The pitch thrust-vectored configurations (fig. 9(b)) show a decreasing trend in resultant thrust ratio due to increasing divergent flap cutout. Locating the yaw-flap hinge at $(x_s - x_t)/l_s = 0$ results in a 2.4-percent loss in resultant thrust ratio at a nozzle pressure ratio of 4.0 (fig. 9(b)). Again, it is probable that these losses are occurring because a portion of the exhaust flow is expanding through the cutout in the divergent flaps, and the nozzle has less divergent flap surface area on which the expanding flow can produce thrust. It is again evident that the effective expansion ratio has decreased because the nozzle pressure ratio at which peak performance occurs has decreased.

Increased divergent flap cutout causes increased internal thrust ratio and decreased resultant pitch vector angle at low nozzle pressure ratios (and also decreased thrust ratio and increased vector angle at higher nozzle pressure ratios) when compared with results from the baseline nozzle. The results from reference 11 for a pitch-vectored nozzle with a similar geometry (to the current baseline nozzle) show similar data trends, but the effect was caused by sidewall cutback instead of divergent flap cutout. The increased thrust ratio at lower nozzle pressure ratios in reference 11 was due in part to a slight increase in static pressure due to sidewall cutback that was greater on the lower divergent flap than on the upper flap. In this configuration, as is the case in the current investigation, at positive pitch-vectored conditions (lower flap down) the upper flap was a forward-facing surface and the lower flap was a rearward-facing surface. The increase in pressure on the upper flap caused a loss in axial force that was overcome by a gain in axial force due to a larger increase in pressure on the lower flap. The result was an overall increased internal thrust ratio. This slight pressure increase also caused a reduction in normal force which, when coupled with the increased axial force, produced a lower resultant pitch thrust vector angle. Although no static pressures were measured in the current investigation, the results of reference 11 are similar to those presented in figure 9(b), and it is possible that this same pressure phenomenon is occurring at low nozzle pressure ratios because of venting of the exhaust flow.

In the current investigation, the loss in axial force at higher nozzle pressure ratios due to a portion of the flow expanding through the divergent flap cutout results in a reduced internal thrust ratio. However, this loss in axial force, when coupled with an increase in normal force, gives a larger resultant pitch thrust vector angle. The reason for this increase in normal force is not known.

There is very little change in discharge coefficient due to the divergent flap cutout of the pitch-vectored nozzle for hinge locations downstream of the throat. The yaw-flap hinge location at $(x_s - x_t)/l_s = 0$ is believed to be upstream of the baseline pitch-vectored nozzle throat, and consequently there is a change in C_d for this configuration as seen in figure 9(b). This increase in C_d is probably a result of differences in measured and actual physical throat areas. It is likely that the throat plane for this configuration is not as skewed to the nozzle centerline (as the baseline throat was) because of ventilation through the cutout in the upper divergent flap. As a result, the actual throat area is probably larger than the measured value of A_t used to compute w_i. Therefore, C_d may be artificially high. If the true physical throat area could be measured, C_d would likely be lower than the values shown.

A/B *power nozzles.* The effect of the divergent flap cutout on unvectored A/B nozzle internal performance is presented in figure 9(c). As discussed previously (and noted in several references), increasing

nozzle ventilation, by either sidewall cutback or divergent flap cutout (as in this paper), tends to reduce the effective expansion ratio. At lower values of NPR, overexpansion losses are simply reduced by ventilation. Therefore, the highest internal performance (at lower values of NPR) would be expected for the configuration with the largest cutout. Conversely, at higher values of NPR the most ventilated configurations are operating farther from the design nozzle pressure ratio; increased underexpansion losses drive these configurations to lower performance levels. A close examination of the internal performance data would also suggest that peak performance levels decrease slightly with increasing cutout. These losses are probably associated with local changes in flap static pressure distribution resulting from flap cutout. A divergent flap cutout of the forward-thrust A/B power nozzle for a hinge location slightly upstream of the throat resulted in a loss of approximately 1 percent when compared with the baseline at an overexpanded nozzle pressure ratio of 4.5.

Pitch-vectored nozzle performance for A/B power configurations with varying amounts of divergent flap cutout is presented in figure 9(d). All data are at overexpanded flow conditions, and therefore these configurations have not reached their peak performance levels. Data trends for F/F_i and δ_p at an NPR below that for peak performance indicate that increasing flap cutout causes an increase in F/F_i and a decrease in δ_p when compared with results from the baseline nozzle. Flap cutout corresponding to a hinge location of -0.03 probably prevents reattachment of the separated flow on the lower divergent flap (as discussed earlier and as indicated by the lower values of δ_p). At NPR = 4.0 (near where reattachment occurs on the baseline nozzle), this continued flow separation leads to increased F/F_i and decreased δ_p because the exhaust is not being turned away from the axial direction as much as before. Resultant thrust ratios at a nozzle pressure ratio near 5.0 (the nozzle is overexpanded at this NPR) are not affected by flap cutout.

Although a slight increase in discharge coefficient can be seen for this hinge location upstream of the throat, values are generally within data-measurement accuracy.

Effects of Yaw-Flap Deflection

Performance characteristics for yaw thrust-vectored configurations and combined pitch and yaw thrust-vectored configurations are presented in figures 10 to 17 for the dry power nozzles and in figures 18 to 25 for the A/B power nozzles. Each figure presents the effects of yaw-flap deflection on nozzle internal performance data for a constant hinge location with yaw flaps of different lengths.

Dry power nozzles. In general, both internal thrust ratio F/F_i and resultant thrust ratio F_r/F_i were significantly decreased by yaw-flap deflection. The losses experienced in F/F_i are certainly expected because flow is being directed away from the axial direction by the yaw flaps. Losses in F_r/F_i indicate that the yaw flaps are not 100 percent efficient at turning the exhaust flow. It is important to note that the magnitude of these turning losses did not necessarily increase with increasing $\delta_{v,y}$. In fact, for configurations with the yaw flaps hinged upstream of the exit, the $\delta_{v,y} = -30°$ deflections generally provided higher resultant thrust ratios than the $-20°$ yaw-flap-deflection cases. (See fig. 11(a), for example.) Further insight into the reasons for this increase in performance can be gained by examination of the nozzle discharge coefficient data.

For all post-exit yaw-vectoring situations (figs. 10 and 14) and one pitch thrust-vectored configuration with the yaw-flap hinge located just upstream of the exit (fig. 15), the nozzle discharge coefficient was independent of yaw-flap deflection. However, in general, yaw-flap deflection about a hinge location upstream of the exit plane caused losses in nozzle discharge coefficient. (See fig. 13, for example.) Losses in C_d ranged from 0 to 3 percent for the $\delta_{v,y} = -20°$ cases and up to 14 percent when the yaw flap was deflected $-30°$. These losses in C_d for the yaw-vectored configurations were caused by a shift in the physical throat location from the expected location (fig. 2(b)) to a position farther downstream and skewed relative to the nozzle centerline. Obviously, the effective physical throat area was much smaller than the nominal unvectored throat area used to compute ideal weight-flow rate. For a given nozzle pressure ratio, a smaller effective throat area reduces the amount of weight flow that can pass through the throat. Therefore, the discharge coefficient, that is, the ratio of measured to ideal weight-flow rate, was decreased.

As a result of this rotation (skewing) of the throat plane, it is likely that an increased amount of the internal flow was turned at subsonic speeds. Since subsonic flow turning is more efficient than supersonic flow turning (and based on the nozzle discharge coefficient data shown in figs. 10 to 17), it is believed that the $-30°$ yaw-flap deflection provides much more subsonic flow turning (in the side-force direction) than the $-20°$ deflection. As a result, the $\delta_{v,y} = -30°$ case could be expected to be the more efficient yaw-vectoring case (higher F_r/F_i).

In addition, increasing the yaw-flap deflection from $-20°$ to $-30°$ should eliminate some flow ventilation (present on the $\delta_{v,y} = -20°$ case) out of the gap between the yaw flap and the upper and lower divergent flaps. This ventilation, as discussed previously, is believed to result in some thrust loss. It also appears that deflection of the yaw flaps to $-30°$ resulted in a decrease in the effective expansion ratio (A_e/A_t) of a yaw thrust-vectored configuration because peak performance (F_r/F_i) for this case generally occurred at a lower nozzle pressure ratio than with the $\delta_{v,y} = 0°$ configuration.

Resultant pitch and yaw thrust vector angles are also presented in figures 10 to 17. As seen, yaw-flap deflection had little effect on resultant pitch vector angle for the unvectored configurations ($\delta_{v,p} = 0°$) and the post-exit, yaw-flap pitch-vectored configurations (figs. 10 to 14), but it caused decreases in δ_p on the combined pitch and yaw vectoring cases with hinge locations upstream of the exit. These decreases became larger as $\delta_{v,y}$ was increased. It would appear that the yaw flaps are generating side force at the expense of both normal force and axial force on these combined pitch and yaw thrust-vectored configurations. The yaw flaps generally do provide the last flow-turning mechanism to affect the flow, and hence the above result might be expected. Resultant yaw vector angle was obviously affected by yaw-flap deflection angle. Increases in $\delta_{v,y}$ did provide increased δ_y. In all cases, however, measured yaw vector angles were less than the geometric deflection angles. The largest resultant yaw vector angle ($-24.3°$) is shown in figure 17(c) for a combined pitch and yaw thrust-vectored configuration with a yaw-flap hinge location of $(x_s - x_t)/l_s = 0$ and a yaw-flap length of $l_y/l_s = 1.00$.

A/B *power nozzles.* Results similar to the dry power nozzle data can be seen for the A/B power configurations in figures 18 to 25. However, it is important to note that all data for these A/B configurations are at overexpanded flow conditions because of limitations on the force balance. In general, yaw-flap deflection caused losses in internal thrust ratio F/F_i and resultant thrust ratio F_r/F_i at nozzle pressure ratios below design. Several configurations showed an increase in F_r/F_i (up to 2 percent) because of yaw-flap deflection at overexpanded nozzle pressure ratios. (See fig. 20.) This result might be due in part to a decrease in the effective expansion ratio of the nozzle, thereby decreasing the overexpansion losses since the nozzle is operating closer to peak F_r/F_i. Additionally, configurations tested with yaw-flap deflection angles of $-20°$ and $-30°$ (figs. 21, 24(b), and 25(c)) that also showed a decrease in nozzle discharge coefficient indicated an increase in F_r/F_i as the flap was deflected from $-20°$ to $-30°$. This result is attributed to an increase in the amount of subsonic flow turning in the side-force direction because of a skewing of the nozzle throat plane (discussed previously).

Pitch thrust-vectored A/B configurations exhibited changes in resultant pitch vector angle because of yaw-flap deflection. In general, δ_p for the yaw-flap-deflected configurations was increased at low NPR and decreased at high NPR when compared with the undeflected yaw flaps. In figure 25(c), data at NPR = 1.8 show an increase of 5° in the resultant pitch vector angle associated with deflection of the yaw flaps from 0° to $-30°$. The generation of side force (by yaw-flap deflection) resulted in an increase in measured normal force and a decrease in measured axial force. Again, the reasons for the increase in normal force are not known.

Resultant yaw vector angle increased with increasing yaw-flap deflection, as expected. However, resultant yaw vector angle was always less than the geometric metal (design) angle. The largest resultant yaw vector angle ($-20.9°$) is shown in figure 21 for a yaw-vectored configuration (no pitch) with a hinge location $(x_s - x_t)/l_s$ of -0.03 and a yaw-flap length l_y/l_s of 1.03.

Figure 26 summarizes the effects of yaw-flap deflection on resultant thrust ratio and resultant pitch vector angle (pitch-vectored nozzles only) for dry power configurations from the current investigation at a constant nozzle pressure ratio. Data are shown at values of NPR near design for undeflected and fully deflected yaw flaps. (No data are shown for yaw-flap deflections $\delta_{v,y}$ of $-20°$ because of the lack of configurations tested. The A/B power configurations have been intentionally left out because of a lack of data at nozzle pressure ratios near peak performance.) For all configurations shown, losses experienced in F_r/F_i due to yaw-flap deflection decreased as the yaw-flap hinge location was moved upstream from the exit plane toward the throat (decreasing values of $(x_s - x_t)/l_s$). This result might be due to a decrease in the velocity of the flow that is being turned in the side-force direction as the hinge location is moved upstream. Note the significant resultant thrust ratio losses on all the post-exit yaw-vectoring configurations ($(x_s - x_t)/l_s = 1.00$). In general, δ_p was decreased by yaw-flap deflection on dry power pitch-vectored nozzle configurations at an NPR near design (fig. 26(b)).

Effects of Varying Yaw-Flap Length and Yaw-Flap Hinge Location

The effects of increasing the length of undeflected yaw flaps on the thrust and turning performance of

forward-thrust and pitch thrust-vectored nozzles at dry and A/B power are presented in figure 27. A constant hinge location of $(x_s - x_t)/l_s = 1.00$ has been chosen as representative of the four hinge locations investigated to illustrate the effects of increasing the yaw-flap length. Note that data for these configurations have been presented earlier in the section entitled "Effects of Yaw-Flap Deflection." Increasing the length of the undeflected yaw flaps held at a constant hinge location caused little or no change in the nozzle internal performance characteristics. Losses were less than 0.5 percent for those configurations shown in figures 27(a), 27(b), and 27(c), and they are considered to be within measurement accuracy of the balance. Only the data shown at a nozzle pressure ratio of 4.0 for the A/B power pitch-vectored nozzle (fig. 27(d)) exhibit a significant change in nozzle performance because of increasing the yaw-flap length. It is obvious that the flow reattachment phenomenon on the lower divergent flap of this nozzle (discussed earlier) has been delayed. It is highly likely that the differences are simply a function of the reattachment location. Note that the data at other pressure ratios presented in figure 27(d) show less than a ±0.5-percent change due to increased yaw-flap length. For this nozzle, increasing the length of undeflected yaw flaps has no effect on discharge coefficient or resultant yaw thrust vector angle.

Nozzle thrust performance and resultant thrust vector angles are presented in figure 28 for varying the yaw-flap length at a constant hinge location for yaw thrust-vectored nozzles (yaw flaps deflected to −30°). As before, dry and A/B power nozzles with and without pitch thrust vectoring are shown for a constant hinge location ($(x_s - x_t)/l_s = 0.33$ for dry power and 0.31 for A/B power). Data for the hinge location shown are typical (of the other hinge locations tested) and indicate that increasing the yaw-flap length decreased the internal and resultant thrust ratios. Increasing the flap length always increased the resultant yaw vector angle. These trends are due to an increase in side force and a decrease in axial force associated with increased yaw-flap length. (This is true for all test data at or near NPR = 4.0.) Increasing yaw-flap length at the three hinge locations upstream of the exit decreased δ_p on the dry power configurations. Losses in discharge coefficient appear to be more a function of hinge location than of yaw-flap length, as is shown in figure 29.

Figure 29 presents data for varying the hinge location of a constant-length yaw flap on yaw-vectored nozzle thrust performance and resultant thrust vector angles for dry power and A/B power nozzles with and without pitch thrust vectoring. A flap length l_y/l_s of 1.00 for dry power configurations (1.03 for A/B power configurations) has been chosen as representative of the three lengths investigated. Configurations with yaw flaps deflected about a hinge at the exit plane exhibited the lowest resultant thrust ratio and lowest resultant yaw vector angle. For all configurations tested, moving the yaw-flap hinge upstream of the exit plane reduced the losses in resultant thrust ratio F_r/F_i due to yaw vectoring. These losses are due in part to the turning of supersonic flow. As the hinge location is moved upstream from the exit, the flow is turned at a lower supersonic velocity (or possibly at subsonic speeds when the throat is skewed to the nozzle centerline), and therefore flow-turning losses caused by the vectored yaw flaps decrease. As discussed previously, a result of the reduction in effective throat area (due to the skewing of the throat plane) is the decrease in discharge coefficient seen in figure 29. This loss in discharge coefficient occurs for all three yaw-flap lengths on both dry and A/B power nozzles.

Figure 30 summarizes resultant thrust ratio and resultant thrust vector angles (except that δ_p is not shown for the $\delta_{v,p} = 0°$ configurations) as a function of yaw-flap hinge location for the three different yaw-flap lengths. (Note that the data presented here constitute one point at a single nozzle pressure ratio for each yaw thrust-vectored configuration tested in this investigation. Although dry power data are presented at an NPR close to peak performance, A/B power data are at overexpanded conditions. However, the data are the highest NPR data available on the A/B power configurations.) Internal performance data are presented in figures 30(a) and 30(b) for the dry power nozzle and in figures 30(c) and 30(d) for the A/B power nozzle.

Conclusions from figure 30 are generally made from dry power data since not enough A/B power data are available for all the trends to be compared. Yaw vectoring from flaps deflected about a hinge location at the exit ($(x_s - x_t)/l_s = 1.00$) causes larger losses in resultant thrust ratio and produces lower resultant yaw vector angles than vectoring from flaps deflected about the other three hinge locations (upstream of the exit). It is also apparent that reductions in nozzle performance (F_r/F_i) as a function of yaw-flap length are much larger for yaw flaps hinged at the exit than for the hinge locations upstream of the exit. Upon further inspection of figures 30(a) and 30(b), it becomes apparent that the maximum resultant yaw vector angle for a constant yaw-flap length is produced by flaps that normally have their trailing edge ending in the exit plane; i.e., the $l_y/l_s = 0.33$ flaps give maximum turning when hinged at $(x_s - x_t)/l_s = 0.67$, the $l_y/l_s = 0.67$ flaps

give maximum turning when hinged at $(x_s - x_t)/l_s = 0.33$, and the $l_y/l_s = 1.00$ flaps give maximum turning when hinged at $(x_s - x_t)/l_s = 0$. This would seem to indicate that for maximum thrust-vectoring capability, the hinge location and yaw-flap length need to be chosen in such a way that $[(x_s - x_t)/l_s] + l_y/l_s = 1.00$. (See fig. 7.)

An examination of data trends for a pure yaw thrust-vectored configuration and combined pitch and yaw thrust-vectored configurations presented in figures 30(a) and 30(b), respectively, leads to the following hypothesis. A pair of yaw flaps hinged between $(x_s - x_t)/l_s = 0.33$ and 0 with the trailing edge extending to the exit would provide a compromise that would probably produce values of resultant thrust ratio slightly lower than those of flaps hinged at $(x_s - x_t)/l_s = 0$ for a pure yaw thrust-vectored configuration and slightly higher than those of flaps hinged at 0 on a combined pitch and yaw thrust-vectored configuration. This hypothetical nozzle would, in return, generate a compromised value of resultant pitch thrust vector angle while maintaining a large resultant yaw thrust vector angle that would be slightly lower than that of flaps hinged at the throat. Note that in comparison with the dry power forward-thrust baseline nozzle (no divergent flap cutout), this hypothetical combined pitch and yaw thrust-vectored nozzle would have a resultant thrust ratio that is 2 to 3 percent below that of the forward-mode nozzle and yet be capable of generating approximately 14° of resultant pitch thrust vector angle and −20° of resultant yaw thrust vector angle.

Although only limited data exist for A/B power nozzles (figs. 30(c) and 30(d)), it does appear from observations of figure 30(d) that the "best" configuration at A/B power also has a hinge location between $(x_s - x_t)/l_s = 0.31$ and −0.03.

The effect of pitch thrust vectoring on yaw-vectored configurations is summarized in figure 31, where resultant thrust ratio and resultant yaw thrust vector angle are shown as a function of yaw-flap hinge location. Data are shown at a nozzle pressure ratio near peak performance for dry power configurations (NPR near design) in figure 31(a) and at over-expanded conditions for A/B power cases (NPR less than design) in figure 31(b). Pitch vectoring a yaw-vectored nozzle decreased the resultant thrust ratio, and this decrease was larger for the A/B nozzles. Pitch thrust vectoring had very little effect on the resultant yaw vector angle. Recall from the previous discussion, however, that yaw-flap deflection generally decreased the resultant pitch vector angle. Ideally from a controls standpoint, it would be desirable to have no cross coupling between the thrust-vectoring processes.

Comparison of Thrust-Vectoring Concepts

The performance of pure yaw thrust vectoring (no pitch) and combined pitch and yaw thrust-vectoring dry power configurations from the current investigation is compared with the performance of the other vectoring-nozzle concepts in figures 32 and 33, respectively. Data in these figures are presented at a nozzle pressure ratio near design for each concept shown and therefore represent peak performance levels. Data on the vertical axes are presented in the form of a ratio such that a value of 1.0 indicates a measured resultant vector angle equal to the geometric ("metal") vector angle. The vertical axes then represent vectoring efficiency of the configurations. The horizontal axes parameters indicate the loss in resultant thrust ratio (relative to the unvectored case) per degree of resultant thrust vector angle generated. A value of 0 indicates that there are no resultant thrust ratio losses due to thrust vectoring. Note that the data presented here from the current investigation are for the $\delta_{v,y} = -30°$ configurations, which produced less thrust loss per degree of flow turning than the $\delta_{v,y} = -20°$ configurations.

A comparison of the performance of several 2-D C-D thrust-vectoring concepts in a yaw thrust-vectored mode (open symbols) with several concepts from the current investigation (solid symbols) is presented in figure 32, where yaw thrust-vectoring efficiency $\delta_y/\delta_{v,y}$ is shown as a function of a vectoring performance-effectiveness parameter $\eta_{r_{\delta_y}}$. The sidewall round-port concept produced both large losses in resultant thrust ratio per degree of yaw vector angle generated and relatively low levels of yaw-vectoring efficiency. As discussed in reference 13, these losses are probably a result of momentum losses incurred while attempting to turn subsonic flow through 90°. (The port was located upstream of the nozzle primary throat.) Low levels of yaw-vectoring efficiency were attributed to the small open area of the port. The powered rudder and post-exit flap concepts show large values of vectoring performance-effectiveness parameter because the yaw-vectoring devices are acting on a supersonic stream. Similar results can be seen for the best and worst cases of post-exit yaw-flap vectoring from the current investigation. (See the solid symbols.) Note that on these configurations, increasing yaw-flap length not only increases yaw thrust-vectoring efficiency but also increases resultant thrust ratio losses per degree of vectoring. As seen, losses in F_r/F_i per degree of vectoring are on the same order as those of reference 17 for a similar post-exit flap concept.

The highest levels of yaw-vectoring efficiency and the lowest levels of vectoring performance-effectiveness parameter were attained by the twin-engine canted-nozzles concept of reference 15 and the downstream-flaps concept of reference 13. Since simple pitch deflection of the upper and lower divergent flaps of the canted-nozzles concept can provide both pitch and yaw vectoring, thrust losses associated with this method are small. When the nozzles are differentially deflected, the normal-force vectors created by the two nozzles cancel out, and the side-force vectors add together to give large resultant yaw vector angles while resultant thrust ratio losses are kept at a minimum. It should be noted that $\delta_{v,y}$ was simply a geometric function of nozzle cant angle. Flaps stowed in the sidewalls of the downstream-flaps concept and sized to fit between the divergent flaps at dry power turned the internal nozzle flow at subsonic speeds, and therefore they were efficient and effective. However, the flap turned into the exhaust could not be deployed when the divergent flaps were pitch vectored, and therefore this concept was not as efficient for combined pitch and yaw vectoring. (See configuration F23 in fig. 33.) Lower values of yaw-vectoring efficiency were obtained from the downstream-flaps concept of reference 14 because of the sizing constraints placed on these flaps which allowed some exhaust to pass the internally deflected flap without being turned.

Other cases presented from the current investigation are configurations with yaw flaps hinged upstream of the exit plane and configurations with the trailing edge ending at the exit plane ($[(x_s - x_t)/l_s] + l_y/l_s = 1.00$). These cases were chosen because they provided the lowest resultant thrust ratio losses per degree of resultant yaw vector angle. Resultant thrust ratio losses for these yaw-vectoring configurations were slightly larger than the downstream-flaps concept of reference 14. However, for the two cases presented where $(x_s - x_t)/l_s \leq 0.33$, values for yaw-vectoring efficiency were higher. Although not shown, increasing flap length for each of these hinge locations improves yaw-vectoring efficiency significantly. As mentioned previously, however, resultant thrust ratio losses were larger for the configurations where $[(x_s - x_t)/l_s] + l_y/l_s \neq 1.00$.

The performance of combined pitch and yaw thrust-vectoring configurations from the current investigation is compared with the performance of previous concepts in figure 33. The vectoring performance-effectiveness parameter $\eta_{r_{\delta_r}}$ in this case is equal to the loss in resultant thrust ratio per degree of resultant thrust vector angle δ_r. (See the Symbols section.) Thus, a concept that is theoretically ideal in pitch thrust-vectoring efficiency ($\delta_p/\delta_{v,p} = 1.0$) will be penalized by poor yaw thrust vectoring and vice versa. The previously tested concepts that provide a high level of pitch thrust-vectoring efficiency tend to provide lower levels of yaw thrust-vectoring efficiency. The twin-engine canted-nozzles concept, for example, which had good performance for pure yaw thrust vectoring (as it would for pure pitch), shows a significant drop in pitch and yaw thrust-vectoring efficiency when used for simultaneous pitch and yaw thrust vectoring. The reason for this performance decrease is that only one nozzle is deflected to obtain both pitch and yaw thrust vectors; thus, only half of the available thrust is used to generate a combined thrust-vectoring capability. (Remember that the resultant thrust vector angles are a function of the ratio of measured normal force or side force to measured axial force. The measured axial force for this configuration includes that generated by the unvectored nozzle as well as that by the vectored one.)

Configurations presented from the current investigation for post-exit flaps produce relatively high values of vectoring performance-effectiveness parameters (large thrust losses) that become larger with increasing flap length. Yaw thrust-vectoring efficiency increases with increasing flap length, whereas pitch thrust-vectoring efficiency remains nearly unchanged. As mentioned previously, concepts are also presented in which the yaw-flap hinge is located upstream of the exit plane and the trailing edge ends at the exit. Generally, configurations from the current investigation, with yaw flaps hinged upstream of the exit and the trailing edge ending at the exit, provided lower values of pitch-vectoring efficiency and higher values of yaw-vectoring efficiency than the previously tested concepts presented in figure 33. In conclusion, a comparison of the current configurations with previous results indicates that these multiaxis thrust-vectoring nozzles produce reasonably high levels of thrust-vectoring efficiency without causing large losses in resultant thrust ratio per degree of resultant thrust vector angle, and hence they represent a promising simultaneous pitch and yaw thrust-vectoring concept.

Conclusions

A static investigation has been conducted to determine the nozzle internal performance and flow-turning characteristics of two-dimensional convergent-divergent (2-D C-D) nozzles modified to provide simultaneous thrust vectors in both the normal-force and side-force planes. This concept utilized divergent flap rotation for thrust vectoring in the pitch plane and deflection of flat yaw flaps hinged at the end of the sidewalls for yaw thrust vectoring. The hinge location of the yaw flaps was varied at

four positions from the exit plane of the nozzle to the throat plane. The yaw flaps were designed to contain the flow laterally independent of operating conditions. In order to eliminate any physical interference between the yaw flap deflected into the exhaust stream and the divergent flaps, the downstream corners of both upper and lower divergent flaps were cut off to allow for up to 30° of yaw-flap deflection. This divergent flap cutout was necessary for the three hinge locations upstream of the exit plane on all four nozzles and for the lower divergent flaps on the pitch-vectored nozzles for the hinge location at the exit plane. This investigation studied the impact of varying the nozzle pitch vector angle, throat area, yaw-flap hinge location, yaw-flap length, and yaw-flap deflection angle on nozzle internal performance characteristics. High-pressure air was used to simulate the jet exhaust at nozzle pressure ratios up to 7.0. Data trends lead to the following conclusions:

1. Results indicate that from an internal performance viewpoint, a 2-D C-D nozzle configuration with yaw flaps hinged at the end of the sidewalls and with the hinge located upstream of the exit plane (and downstream corners of the divergent flaps cut off) is a viable simultaneous pitch and yaw thrust-vectoring concept.

2. The removal of the downstream corners of the divergent flaps for a yaw-flap hinge location at the throat plane had very little effect on internal thrust ratio for a low-expansion-ratio forward-thrust nozzle (less than 0.5 percent at a nozzle pressure ratio near design). At afterburning (A/B) power, divergent flap cutout on a forward-thrust nozzle resulted in a loss of approximately 1 percent in internal thrust ratio at a nozzle pressure ratio (NPR) near design for a hinge location slightly upstream of the throat.

3. Thrust vectoring from yaw flaps hinged at the exit plane caused large losses in resultant thrust ratio and produced low resultant yaw thrust vector angles.

4. Dry power configurations in which the yaw-flap hinge is located upstream of the exit and the trailing edge ends at the exit of the nozzle produced larger resultant yaw vector angles than configurations with yaw flaps that end upstream or downstream of the exit plane.

5. Generally, yaw vectoring of the dry power nozzle to the maximum deflection angle about a hinge location upstream of the exit plane caused the throat to rotate in the nozzle and decrease in effective area, thereby decreasing the discharge coefficient. This result led to an increased amount of subsonic flow turning and consequently an increase in resultant thrust ratio.

6. Pitch thrust vectoring of a yaw-vectored nozzle had little effect on resultant yaw vector angle.

7. In general, yaw thrust vectoring of the pitch-vectored nozzle decreased the resultant pitch vector angle.

NASA Langley Research Center
Hampton, VA 23665-5225
February 8, 1990

References

1. Herbst, W. B.: Future Fighter Technologies. *J. Aircr.*, vol. 17, no. 8, Aug. 1980, pp. 561–566.
2. Well, K. H.; Faber, B.; and Berger, E.: Optimization of Tactical Aircraft Maneuvers Utilizing High Angles of Attack. *J. Guid., Control, & Dyn.*, vol. 5, no. 2, Mar.–Apr. 1982, pp. 131 137.
3. Skow, Andrew M.; Hamilton, William L.; and Taylor, John H.: Advanced Fighter Agility Metrics. AIAA-85-1779, Aug. 1985.
4. Nelson, B. D.; and Nicolai, L. M.: Application of Multi-Function Nozzles to Advanced Fighters. AIAA-81-2618, Dec. 1981.
5. Pennington, J. E.; and Meintel, A. J., Jr.: Performance and Human Factors Results From Thrust Vectoring Investigations in Simulated Air Combat. *Proceedings of the 1980 Joint Automatic Control Conference, Volume 1*, IEEE: 80CH1580-0, American Automatic Control Council, c.1980, Paper TA1-A.
6. Lacey, David W.: Air Combat Advantages From Reaction Control Systems. SAE Tech. Paper Ser. 801177, Oct. 1980.
7. Capone, Francis J.: *Static Performance of Five Twin-Engine Nonaxisymmetric Nozzles With Vectoring and Reversing Capability.* NASA TP-1224, 1978.
8. Capone, Francis J.; and Maiden, Donald L.: *Performance of Twin Two-Dimensional Wedge Nozzles Including Thrust Vectoring and Reversing Effects at Speeds up to Mach 2.20.* NASA TN D-8449, 1977.
9. Capone, Francis J.; and Reubush, David E.: *Effects of Varying Podded Nacelle-Nozzle Installations on Transonic Aeropropulsive Characteristics of a Supersonic Fighter Aircraft.* NASA TP-2120, 1983.
10. Re, Richard J.; and Leavitt, Laurence D.: *Static Internal Performance Including Thrust Vectoring and Reversing of Two-Dimensional Convergent-Divergent Nozzles.* NASA TP-2253, 1984.
11. Bare, E. Ann; and Reubush, David E.: *Static Internal Performance of a Two-Dimensional Convergent-Divergent Nozzle With Thrust Vectoring.* NASA TP-2721, 1987.
12. Berrier, Bobby L.; and Re, Richard J.: *Effect of Several Geometric Parameters on the Static Internal Performance of Three Nonaxisymmetric Nozzle Concepts.* NASA TP-1468, 1979.
13. Mason, Mary L.; and Berrier, Bobby L.: *Static Investigation of Several Yaw Vectoring Concepts on Nonaxisymmetric Nozzles.* NASA TP-2432, 1985.

14. Capone, Francis J.; and Bare, E. Ann: *Multiaxis Control Power From Thrust Vectoring for a Supersonic Fighter Aircraft Model at Mach 0.20 to 2.47.* NASA TP-2712, 1987.

15. Capone, Francis J.; and Mason, Mary L.: *Multiaxis Aircraft Control Power From Thrust Vectoring at High Angles of Attack.* NASA TM-87741, 1986.

16. Berrier, Bobby L.; and Mason, Mary L.: *Static Performance of an Axisymmetric Nozzle With Post-Exit Vanes for Multiaxis Thrust Vectoring.* NASA TP-2800, 1988.

17. Mason, Mary L.; and Berrier, Bobby L.: *Static Performance of Nonaxisymmetric Nozzles With Yaw Thrust-Vectoring Vanes.* NASA TP-2813, 1988.

18. Reubush, David E.; and Berrier, Bobby L.: *Effects of the Installation and Operation of Jet-Exhaust Yaw Vanes on the Longitudinal and Lateral-Directional Characteristics of the F-14 Airplane.* NASA TP-2769, 1987.

19. Peddrew, Kathryn H., compiler: *A User's Guide to the Langley 16-Foot Transonic Tunnel.* NASA TM-83186, 1981.

20. Mercer, Charles E.; Berrier, Bobby L.; Capone, Francis J.; Grayston, Alan M.; and Sherman, C. D.: *Computations for the 16-Foot Transonic Tunnel--NASA, Langley Research Center, Revision 1.* NASA TM-86319, 1987. (Supersedes NASA TM-86319, 1984.)

21. Stratford, B. S.: The Calculation of the Discharge Coefficient of Profiled Choked Nozzles and the Optimum Profile for Absolute Air Flow Measurement. *J. Royal Aeronaut. Soc.*, vol. 68, no. 640, Apr. 1964, pp. 237 245.

22. Shapiro, Ascher H.: *The Dynamics and Thermodynamics of Compressible Fluid Flow, Volume I.* Ronald Press Co., c.1953.

23. Leavitt, Laurence D.; and Bangert, Linda S.: *Performance Characteristics of Axisymmetric Convergent-Divergent Exhaust Nozzles With Longitudinal Slots in the Divergent Flaps.* NASA TP-2013, 1982.

Table I. Index to Data Figures

(a) Dry power forward-thrust nozzle with $\delta_{v,p} = 0°$

$(x_s - x_t)/l_s$	l_y/l_s	$\delta_{v,y}$, deg	Internal performance figures
1.00	0	0	8(a), 9(a), 27(a)
	.33	0	10(a), 27(a)
	.33	−30	10(a)
	.67	0	10(b), 27(a)
	.67	−30	10(b)
	1.00	0	10(c), 27(a)
	1.00	−20	10(c)
	1.00	−30	10(c), 29(a)
0.67	0.33	0	9(a), 11(a)
	.33	−20	11(a)
	.33	−30	11(a)
	.67	0	11(b)
	.67	−30	11(b)
	1.00	0	11(c)
	1.00	−30	11(c), 29(a)
0.33	0.33	0	12(a)
	.33	−30	12(a), 28(a)
	.67	0	9(a), 12(b)
	.67	−20	12(b)
	.67	−30	12(b), 28(a)
	1.00	0	12(c)
	1.00	−30	12(c), 28(a), 29(a)
0	0.33	0	13(a)
	.33	−30	13(a)
	.67	0	13(b)
	.67	−30	13(b)
	1.00	0	9(a), 13(c)
	1.00	−20	13(c)
	1.00	−30	13(c), 29(a)

(b) Dry power pitch-vectored nozzle with $\delta_{v,p} = 19.53°$

$(x_s - x_t)/l_s$	l_y/l_s	$\delta_{v,y}$, deg	Internal performance figures
1.00	0	0	8(b), 9(b), 27(b)
	.33	0	14(a), 27(b)
	.33	−30	14(a)
	.67	0	14(b), 27(b)
	.67	−30	14(b)
	1.00	0	14(c), 27(b)
	1.00	−20	14(c)
	1.00	−30	14(c), 29(b)
0.67	0.33	0	9(b), 15(a)
	.33	−20	15(a)
	.33	−30	15(a)
	.67	0	15(b)
	.67	−30	15(b)
	1.00	0	15(c)
	1.00	−30	15(c), 29(b)
0.33	0.33	0	16(a)
	.33	−30	16(a), 28(b)
	.67	0	9(b), 16(b)
	.67	−20	16(b)
	.67	−30	16(b), 28(b)
	1.00	0	16(c)
	1.00	−30	16(c), 28(b), 29(b)
0	0.33	0	17(a)
	.33	−30	17(a)
	.67	0	17(b)
	.67	−30	17(b)
	1.00	0	9(b), 17(c)
	1.00	−20	17(c)
	1.00	−30	17(c), 29(b)

Table I. Concluded

(c) A/B power forward-thrust nozzle with $\delta_{v,p} = 0°$

$(x_s - x_t)/l_s$	l_y/l_s	$\delta_{v,y}$, deg	Internal performance figures
1.00	0	0	8(c), 9(c), 27(c)
	1.03	0	18, 27(c)
	1.03	−30	18, 29(c)
0.66	0.34	0	9(c), 19
	.34	−30	19
0.31	0.34	0	20(a)
	.34	−30	20(a), 28(c)
	.69	0	9(c), 20(b)
	.69	−30	20(b), 28(c)
	1.03	0	20(c)
	1.03	−30	20(c), 28(c), 29(c)
−0.03	1.03	0	9(c), 21
	1.03	−20	21
	1.03	−30	21, 29(c)

(d) A/B power pitch-vectored nozzle with $\delta_{v,p} = 20.26°$

$(x_s - x_t)/l_s$	l_y/l_s	$\delta_{v,y}$, deg	Internal performance figures
1.00	0	0	8(d), 9(d), 27(d)
	1.03	0	22, 27(d)
	1.03	−20	22
	1.03	−30	22, 29(d)
0.66	0.34	0	9(d), 23
	.34	−20	23
	.34	−30	23
0.31	0.34	0	24(a)
	.34	−30	24(a), 28(d)
	.69	0	9(d), 24(b)
	.69	−20	24(b)
	.69	−30	24(b), 28(d)
	1.03	0	24(c)
	1.03	−30	24(c), 28(d), 29(d)
−0.03	0.34	0	25(a)
	.34	−30	25(a)
	.69	0	25(b)
	.69	−30	25(b)
	1.03	0	9(d), 25(c)
	1.03	−20	25(c)
	1.03	−30	25(c), 29(d)

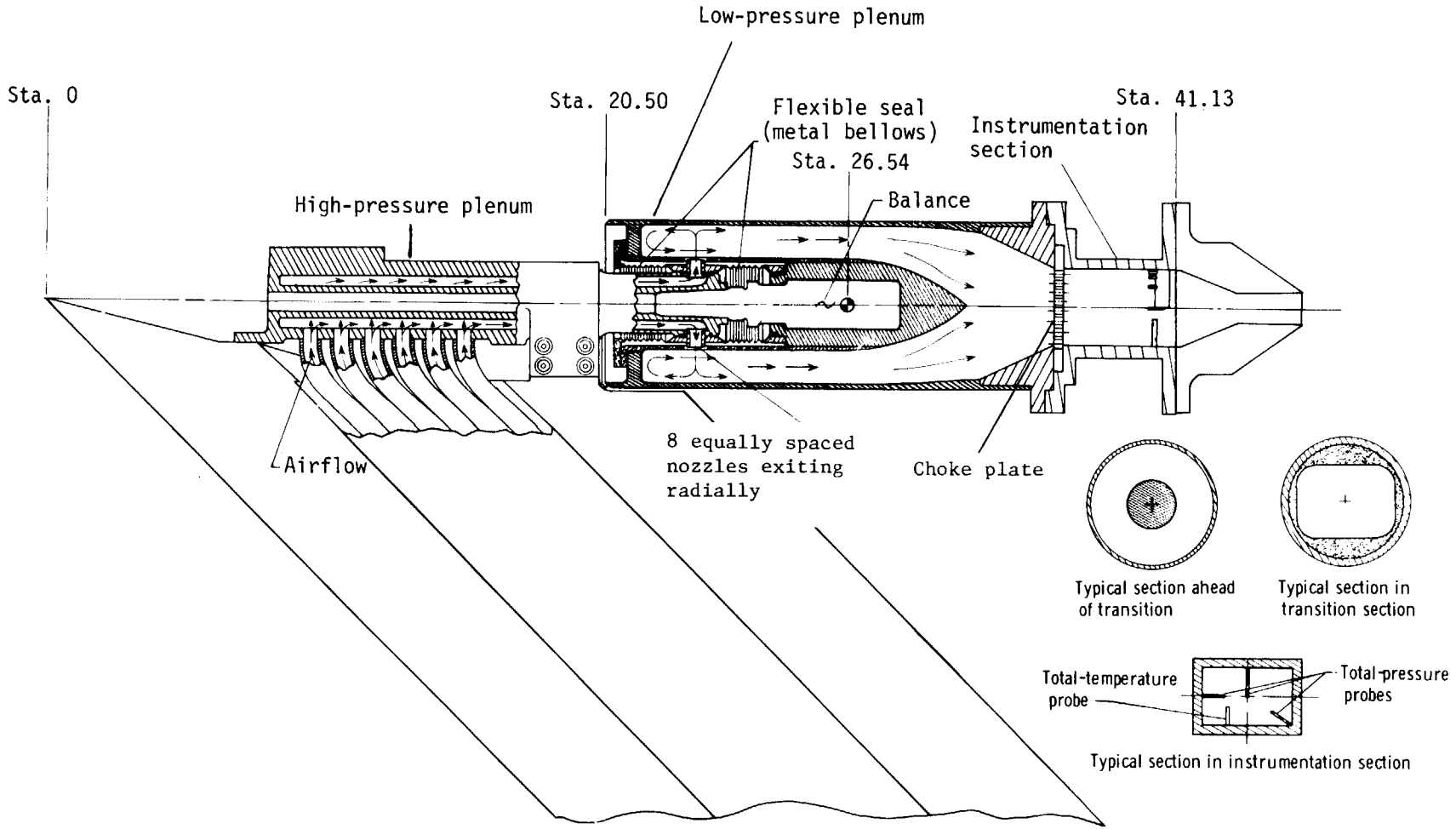

(a) Sketch.

Figure 1. Air-powered nacelle test apparatus with typical 2-D C-D nozzle test configuration installed.

ORIGINAL PAGE
BLACK AND WHITE PHOTOGRAPH

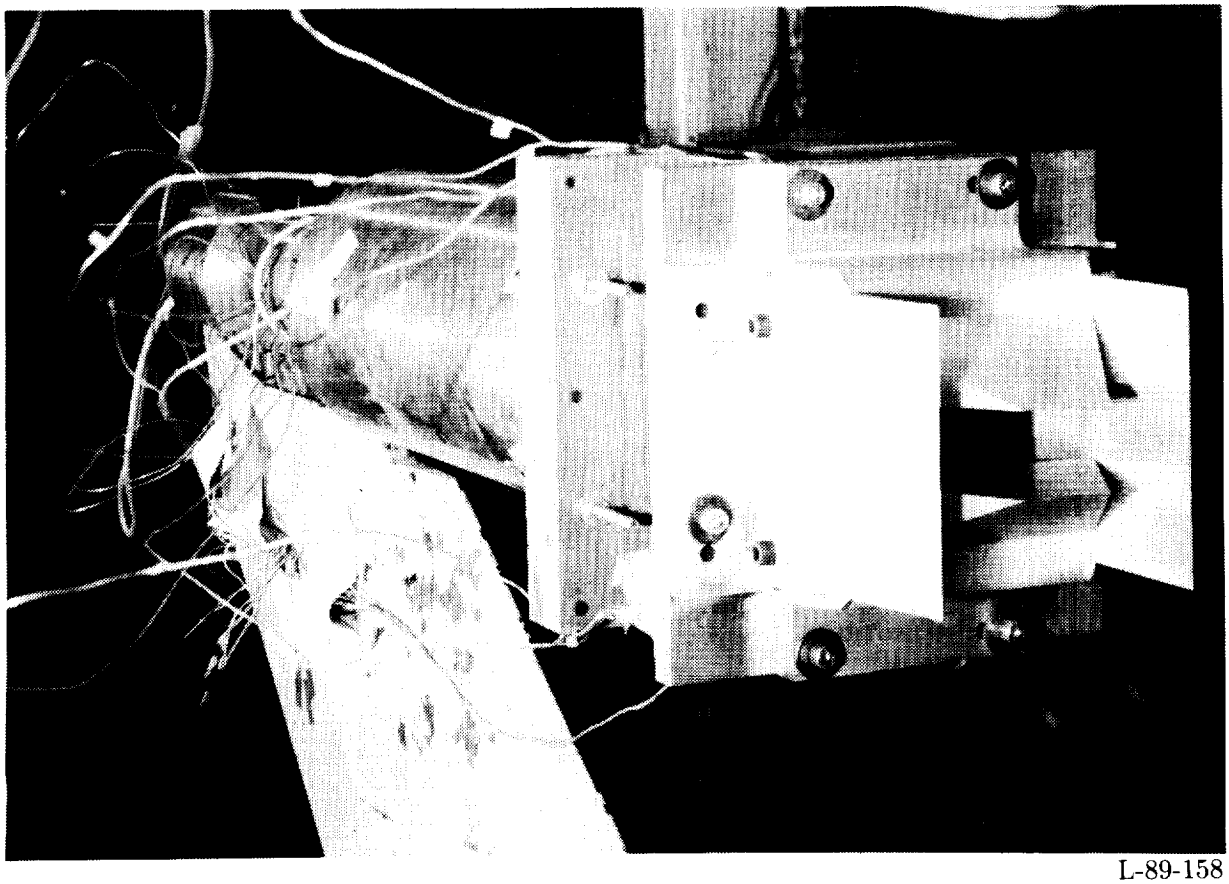

L-89-158

(b) Photograph.

Figure 1. Continued.

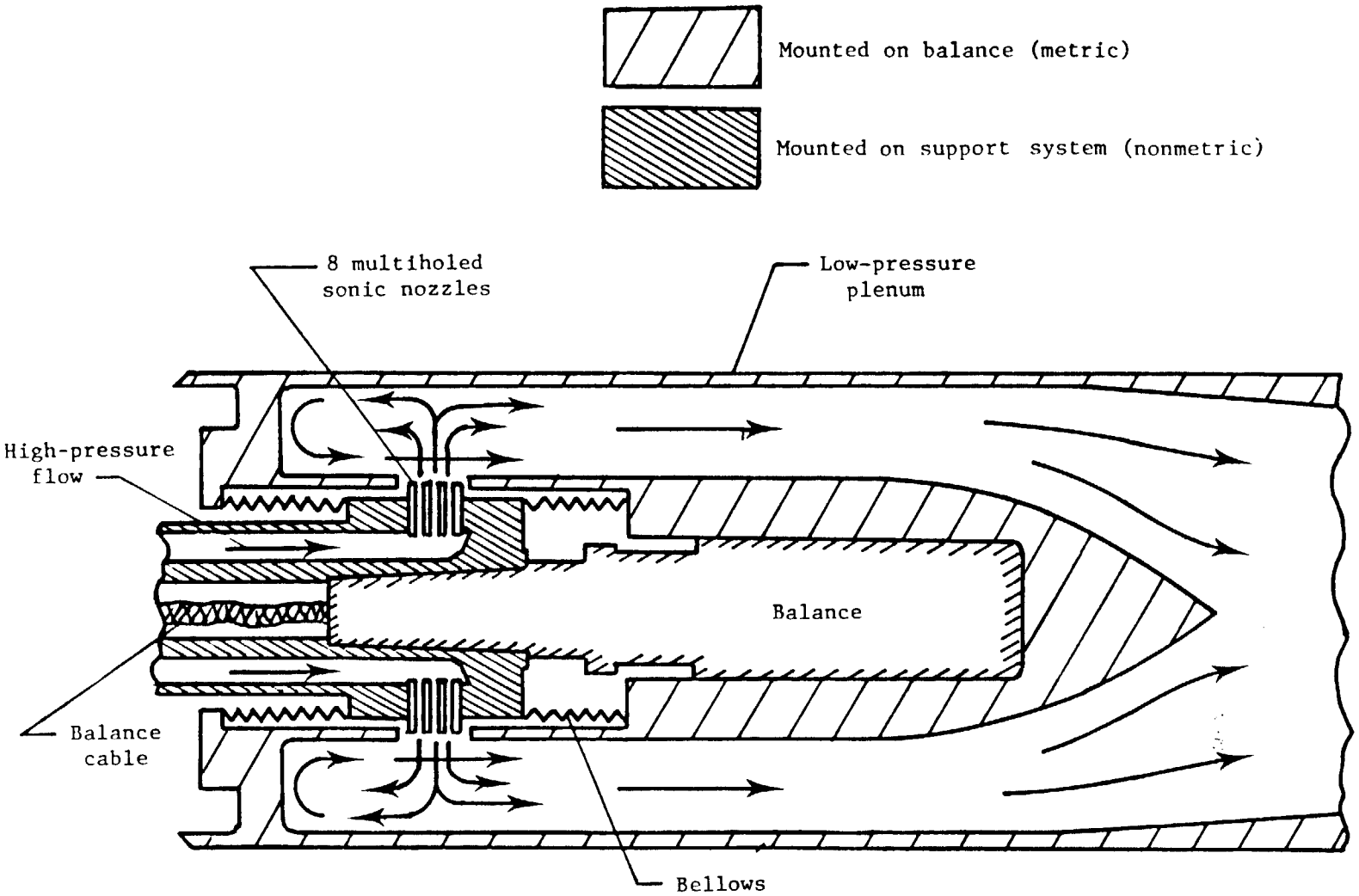

(c) Schematic cross section of flow transfer system.

Figure 1. Concluded.

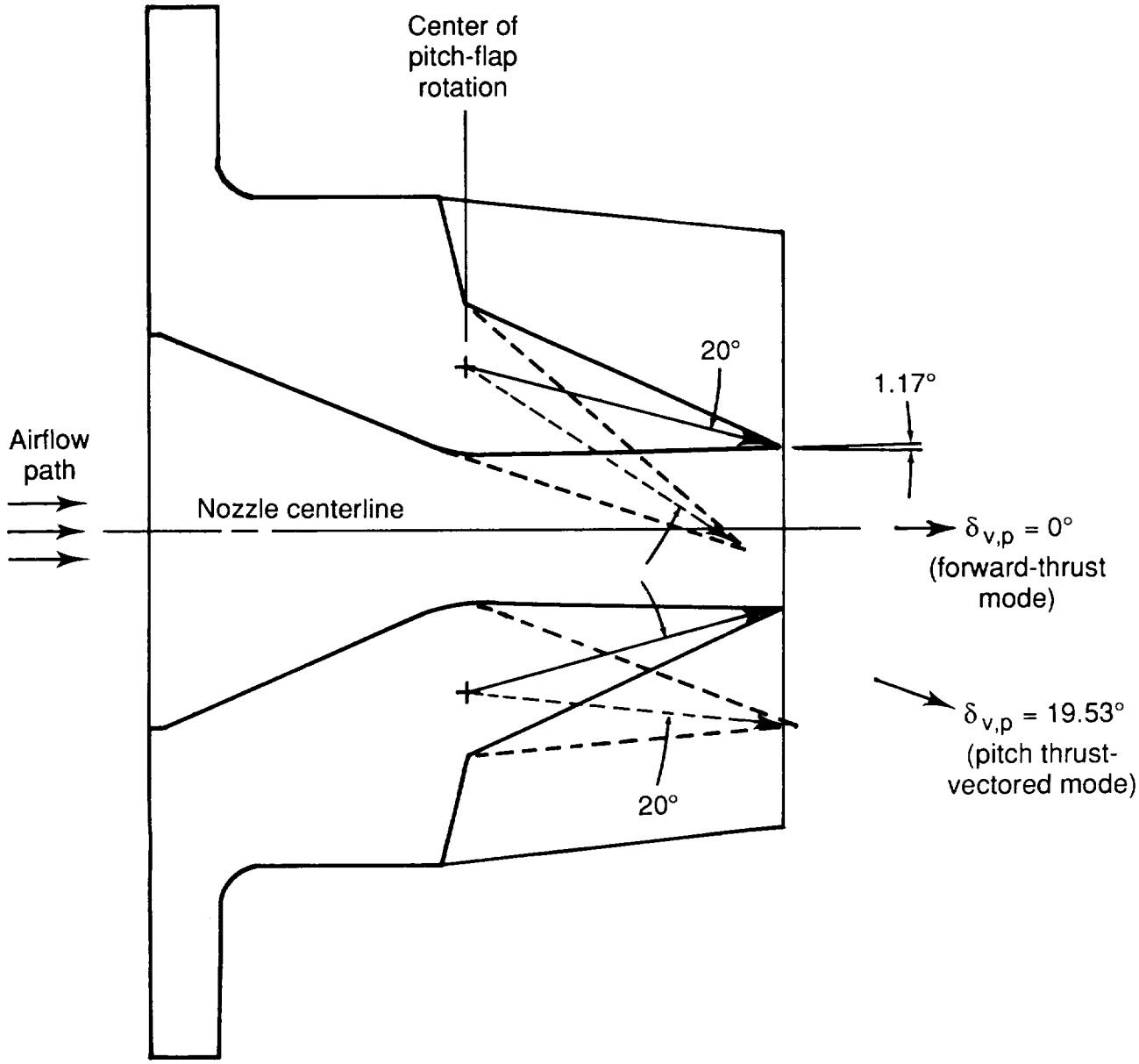

(a) Side view sketch of dry power baseline nozzles.

Figure 2. Nozzle geometry with one sidewall removed. Linear dimensions are in inches.

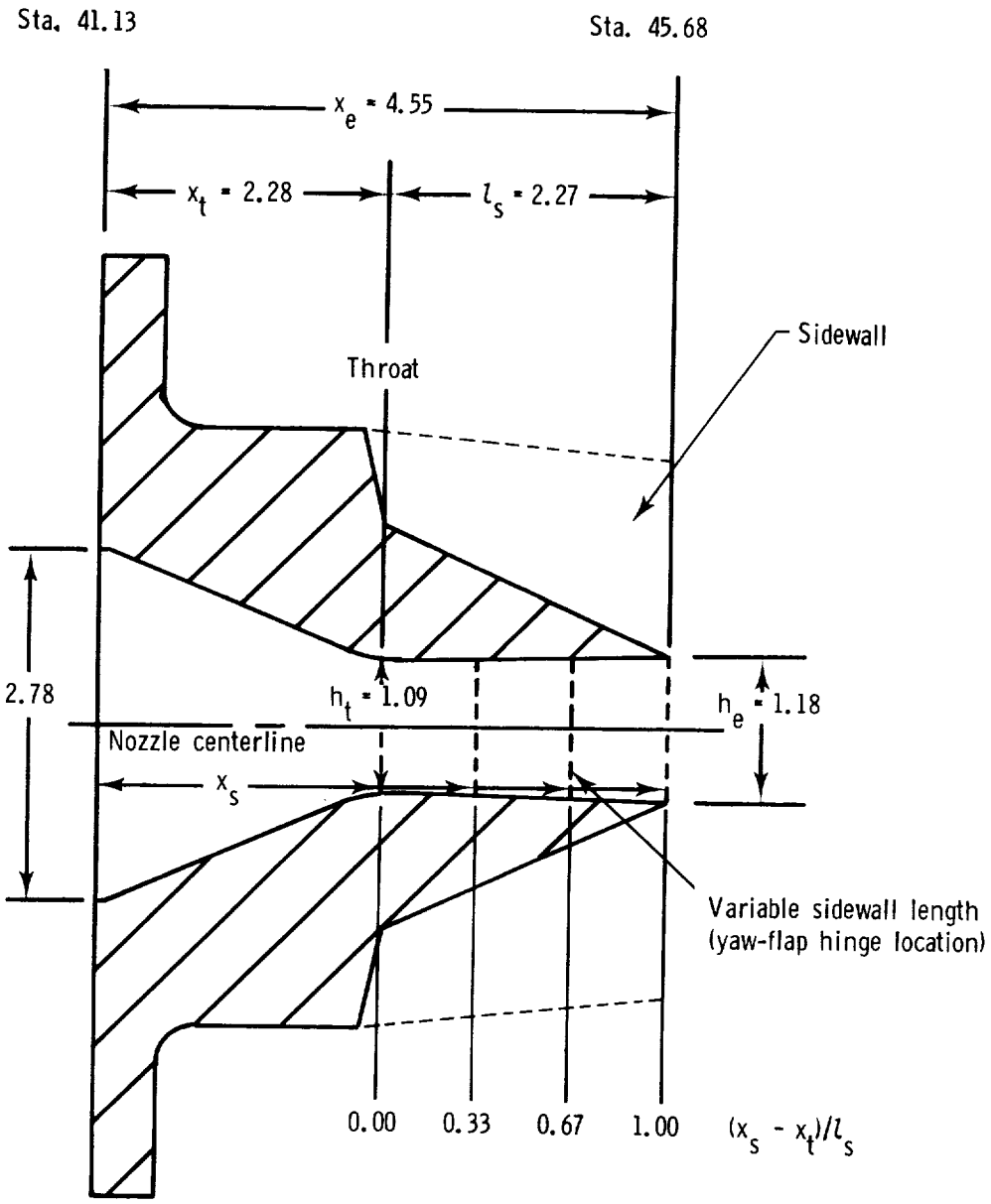

x_s, in.	$(x_s - x_t)/l_s$	A_t, in^2	A_e, in^2	A_e/A_t	AR
4.55	1.00	4.33	4.72	1.09	3.70
3.79	.67	4.41			3.64
3.03	.33	4.42			3.63
2.28	0	4.40			3.64

(b) Dry power nozzle with $\delta_{v,p} = 0°$.

Figure 2. Continued.

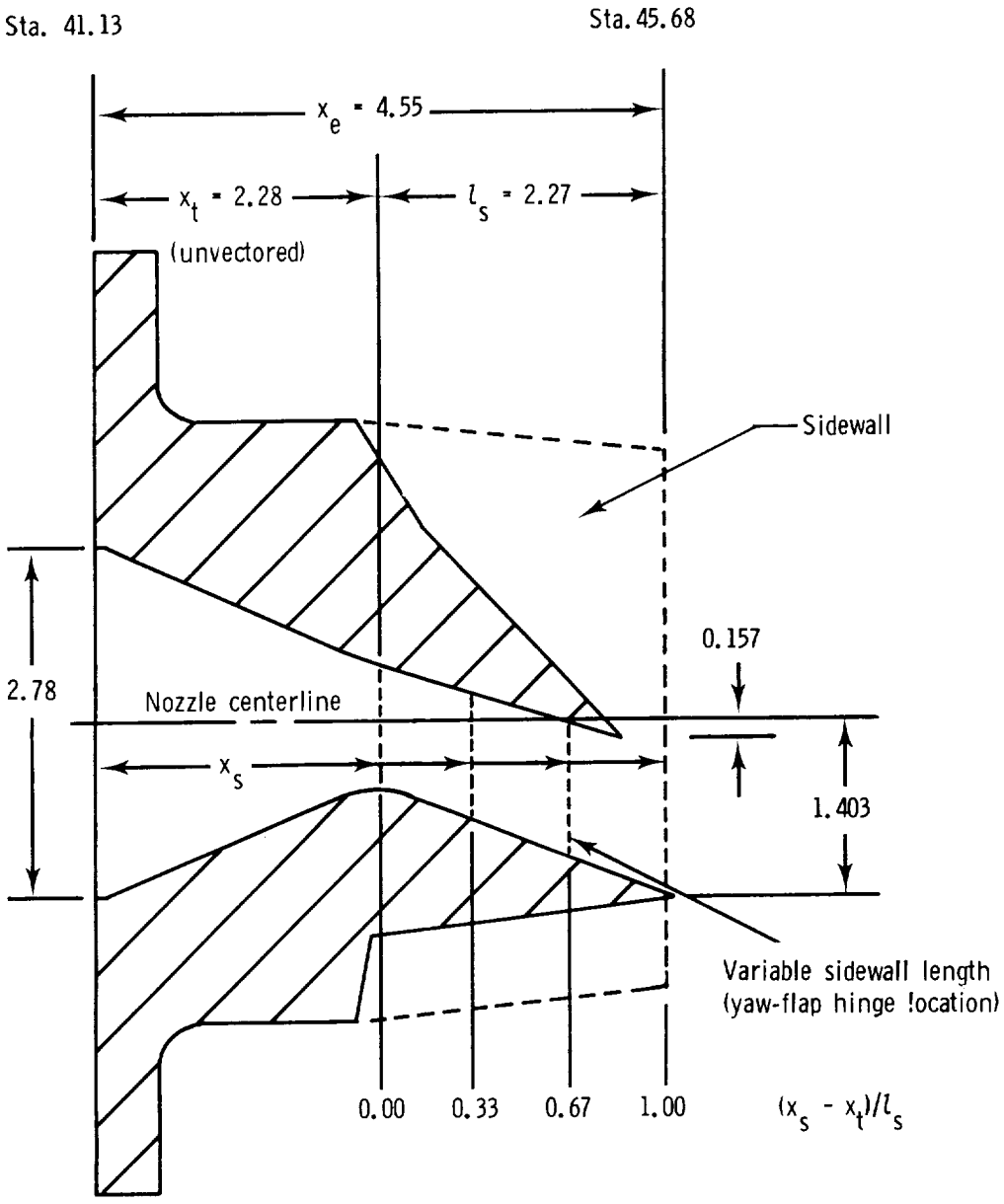

x_s, in.	$(x_s - x_t)/l_s$	A_t, in^2	A_e, in^2	A_e/A_t	AR
4.55	1.00	3.91	4.98	1.27	4.10
3.79	.67	3.92			4.10
3.03	.33	3.91			4.09
2.28	0	3.91			4.09

(c) Dry power nozzle with $\delta_{v,p} = 19.53°$.

Figure 2. Continued.

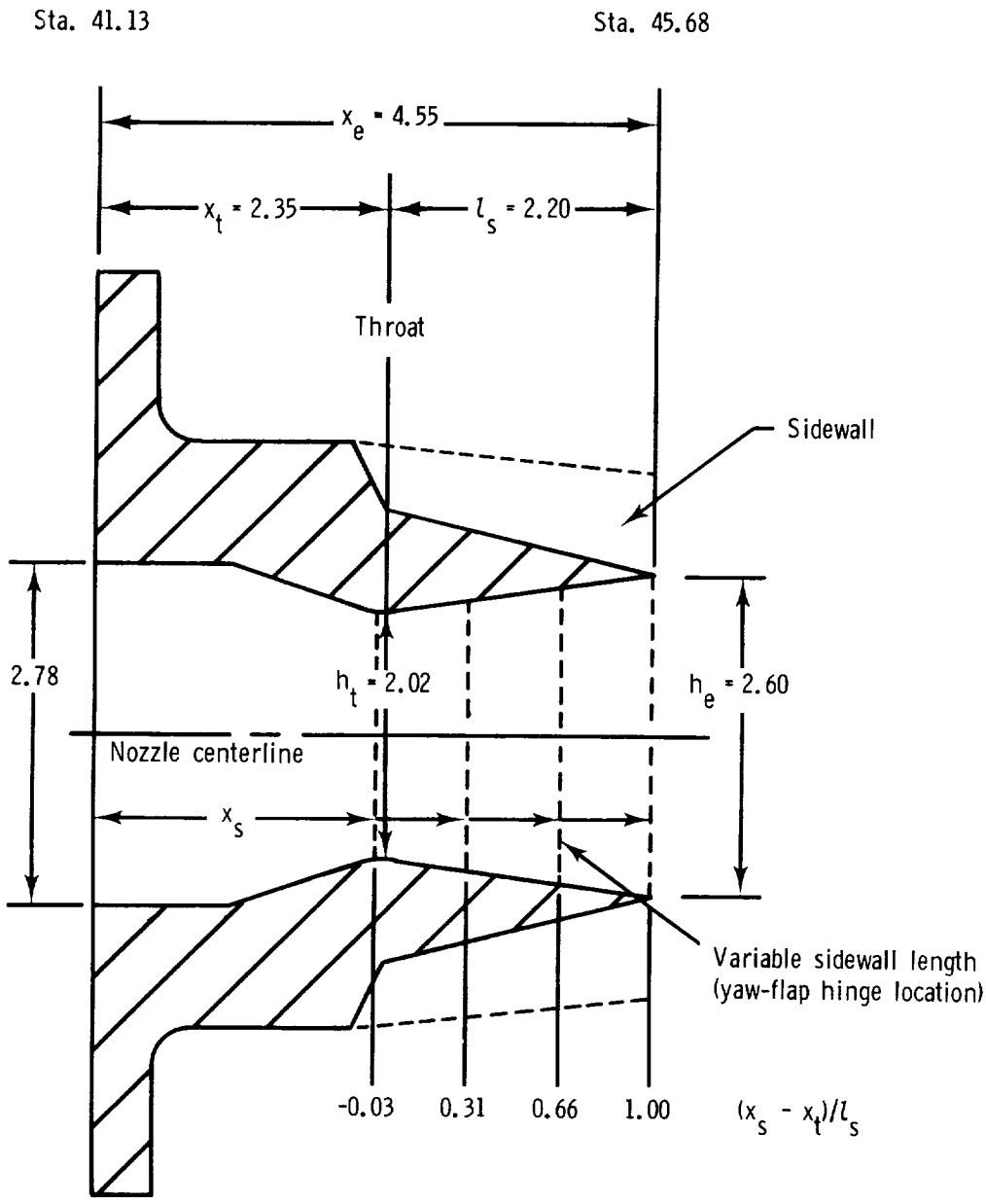

x_s, in.	$(x_s - x_t)/l_s$	A_t, in^2	A_e, in^2	A_e/A_t	AR
4.55	1.00	8.05	10.40	1.29	1.99
3.79	.66	8.11			1.97
3.03	.31	8.12			1.97
2.28	-.03	8.11			1.97

(d) A/B nozzle with $\delta_{v,p} = 0°$.

Figure 2. Continued.

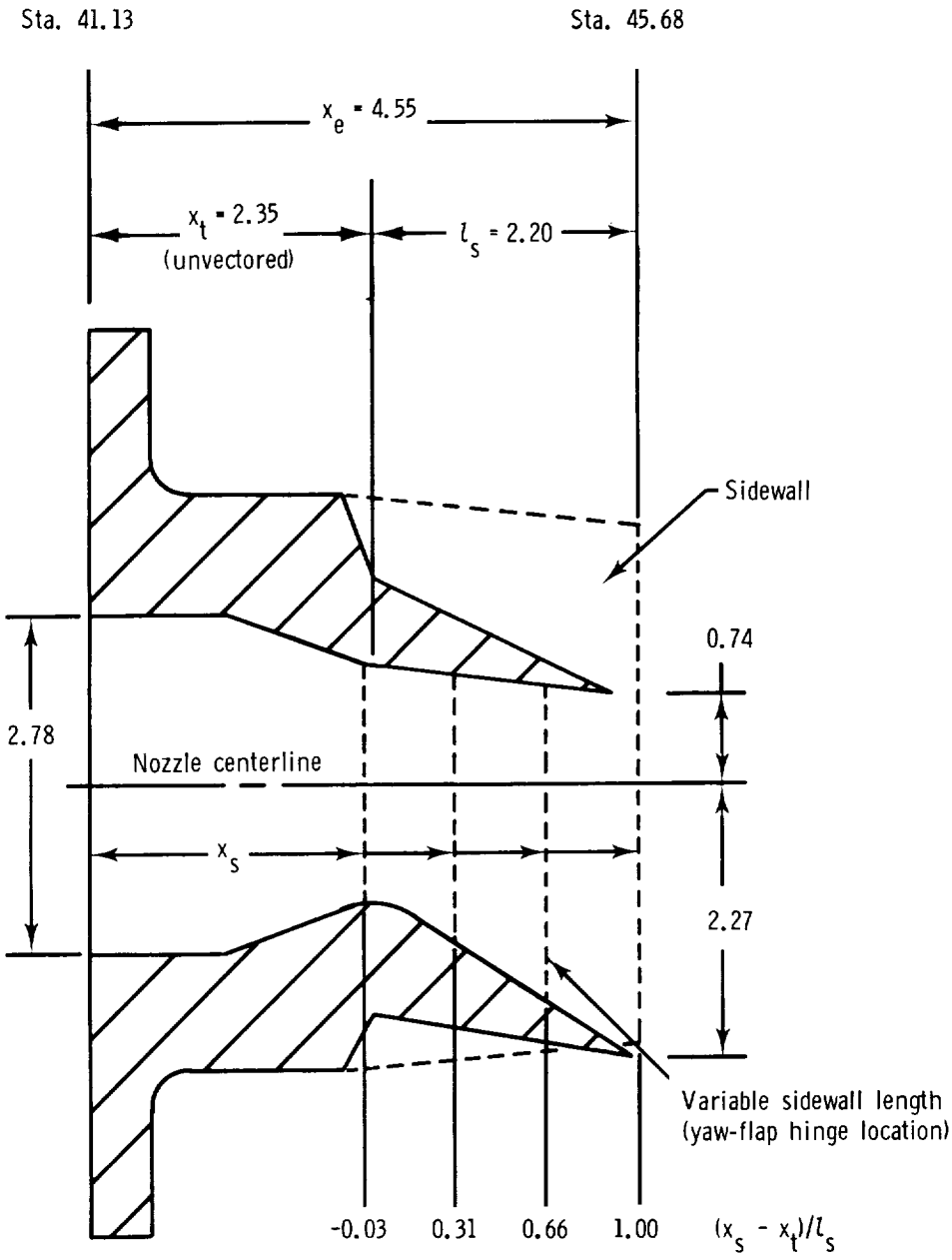

x_s, in.	$(x_s - x_t)/l_s$	A_t, in^2	A_e, in^2	A_e/A_t	AR
4.55	1.00	7.97	12.04	1.51	2.01
3.79	.66	7.98			2.01
3.03	.31	7.99			2.00
2.28	.03	8.00			2.00

(e) A/B nozzle with $\delta_{v,p} = 20.26°$.

Figure 2. Concluded.

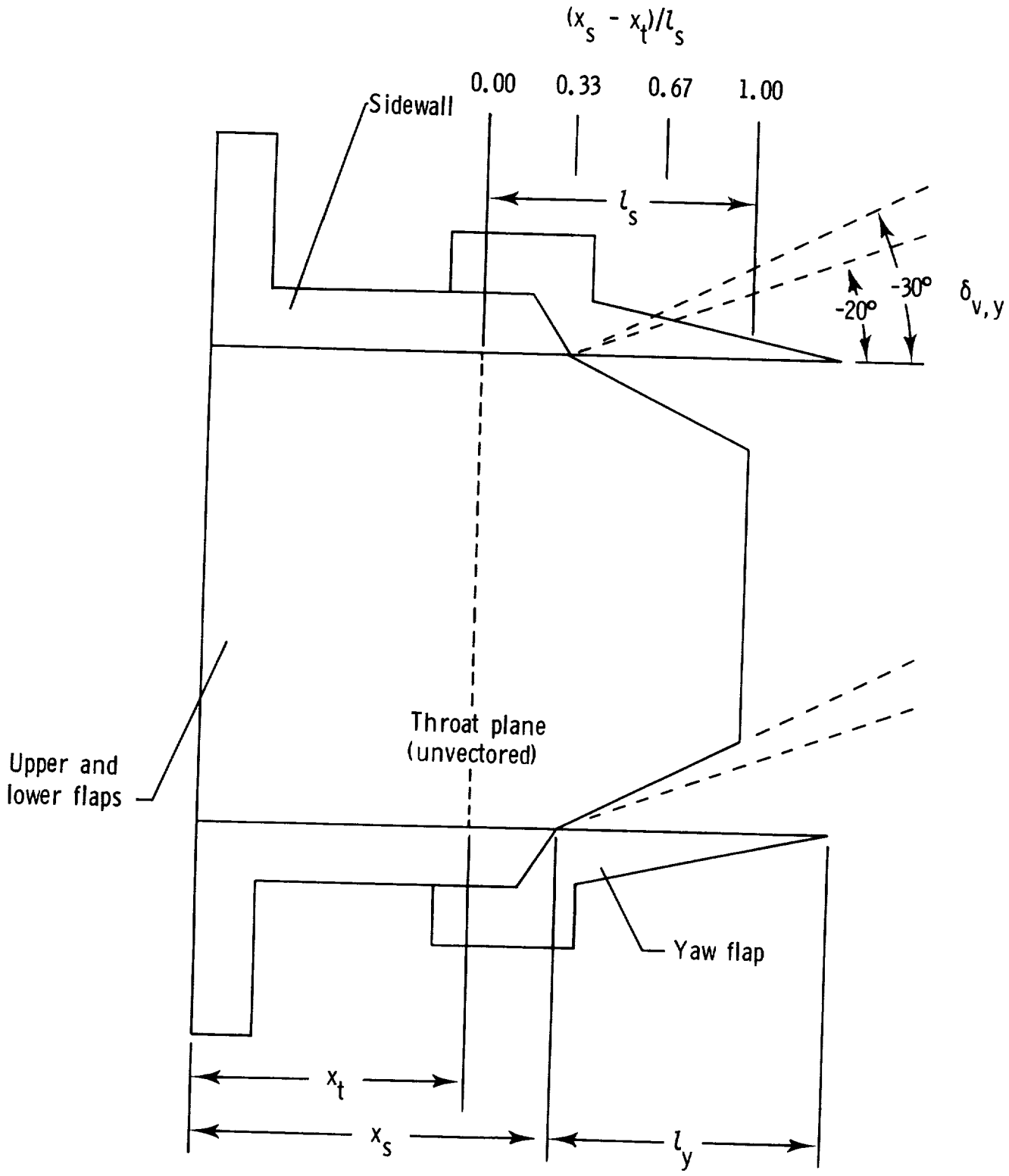

Figure 3. Top view sketch of typical dry power configuration.

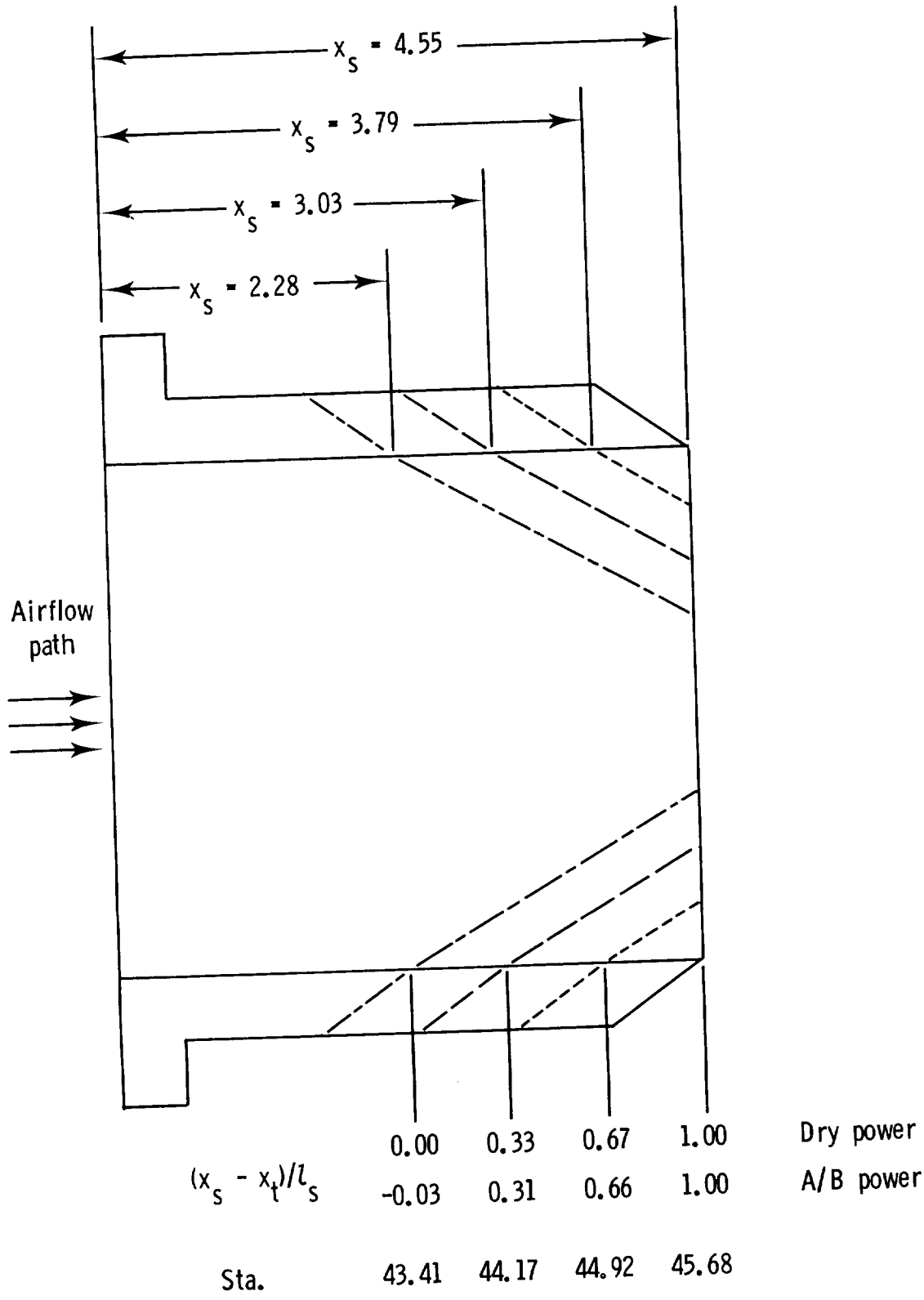

Figure 4. Top view sketch of yaw-flap hinge locations. Linear dimensions are in inches.

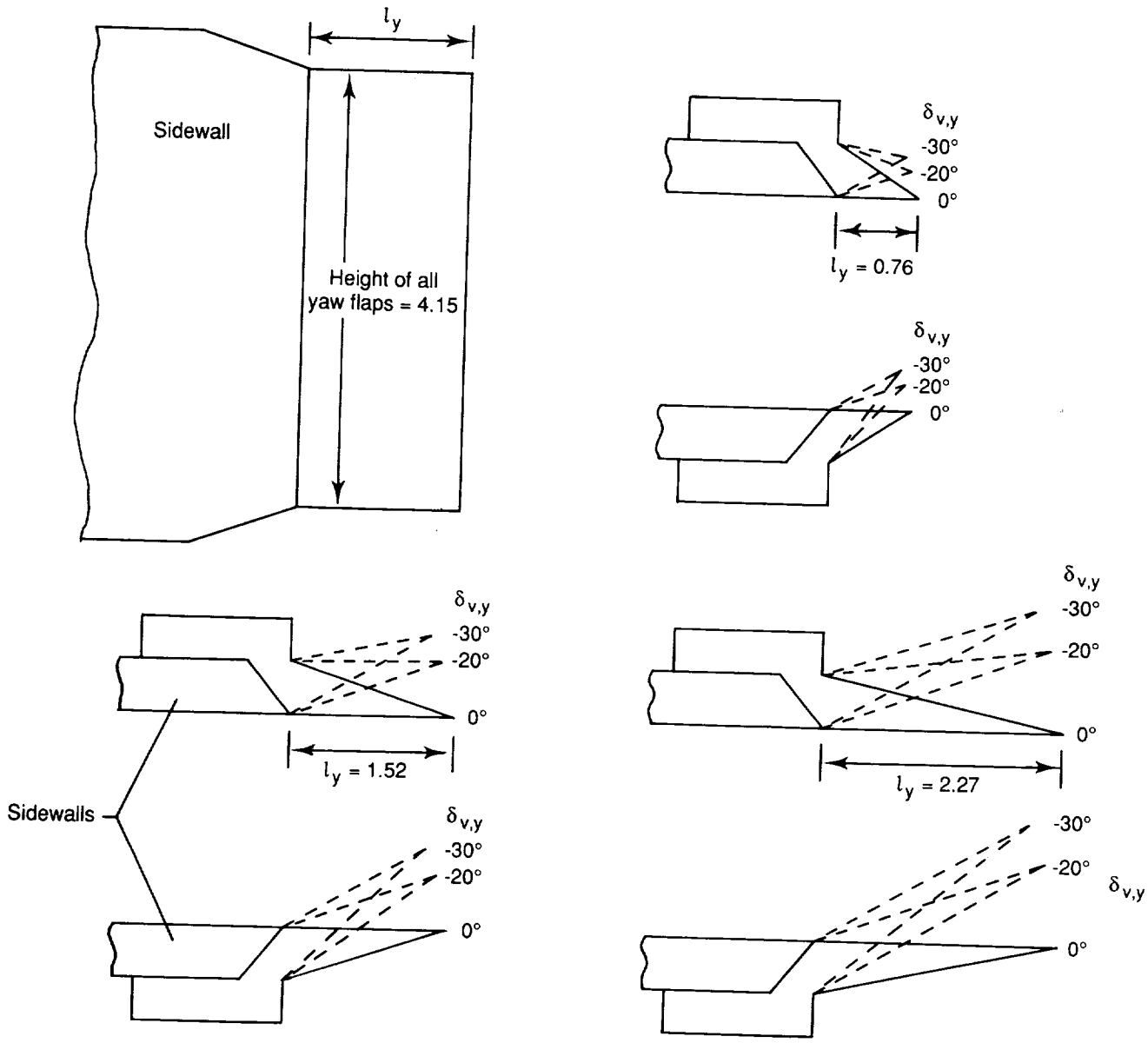

Figure 5. Sketch of yaw-flap geometry. Linear dimensions are in inches.

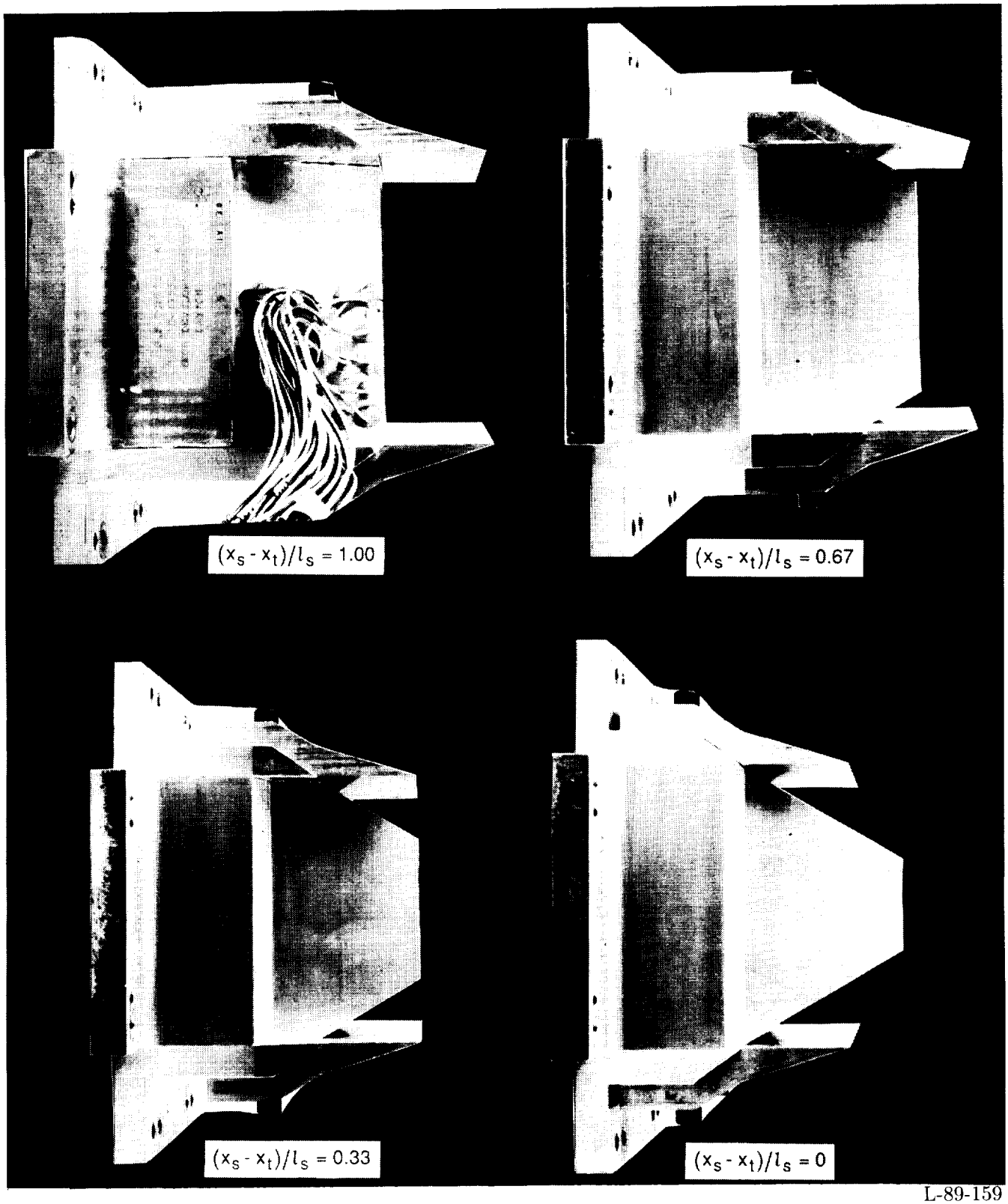

L-89-159

(a) Photographs.

Figure 6. Details of dry power nozzle configurations ($\delta_{v,p} = 0°$) with the same set of yaw flaps at four different hinge locations. $l_y/l_s = 0.67$.

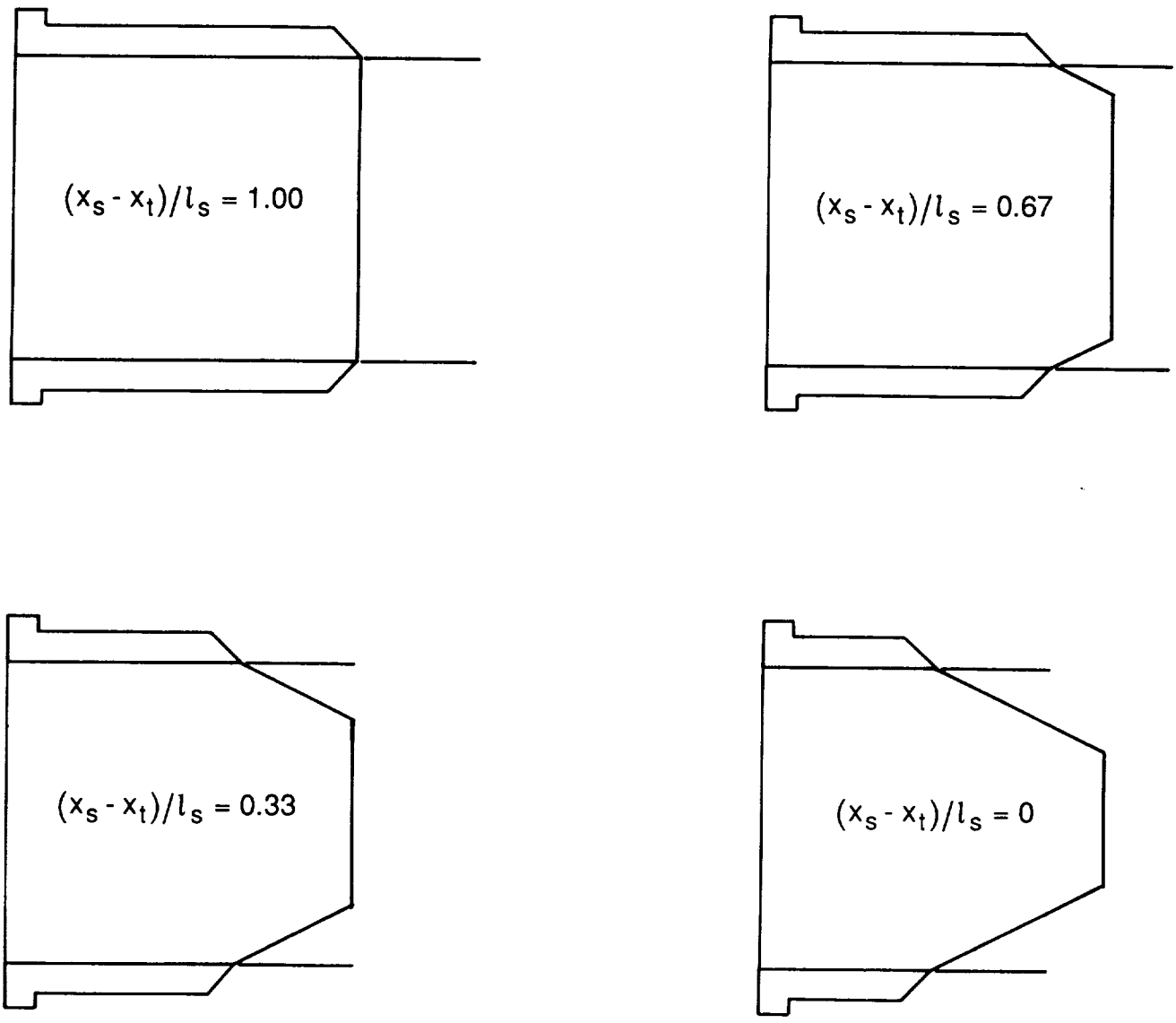

(b) Sketches. $\delta_{v,p} = 0°$; $\delta_{v,y} = 0°$; $l_y/l_s = 0.67$.

Figure 6. Concluded.

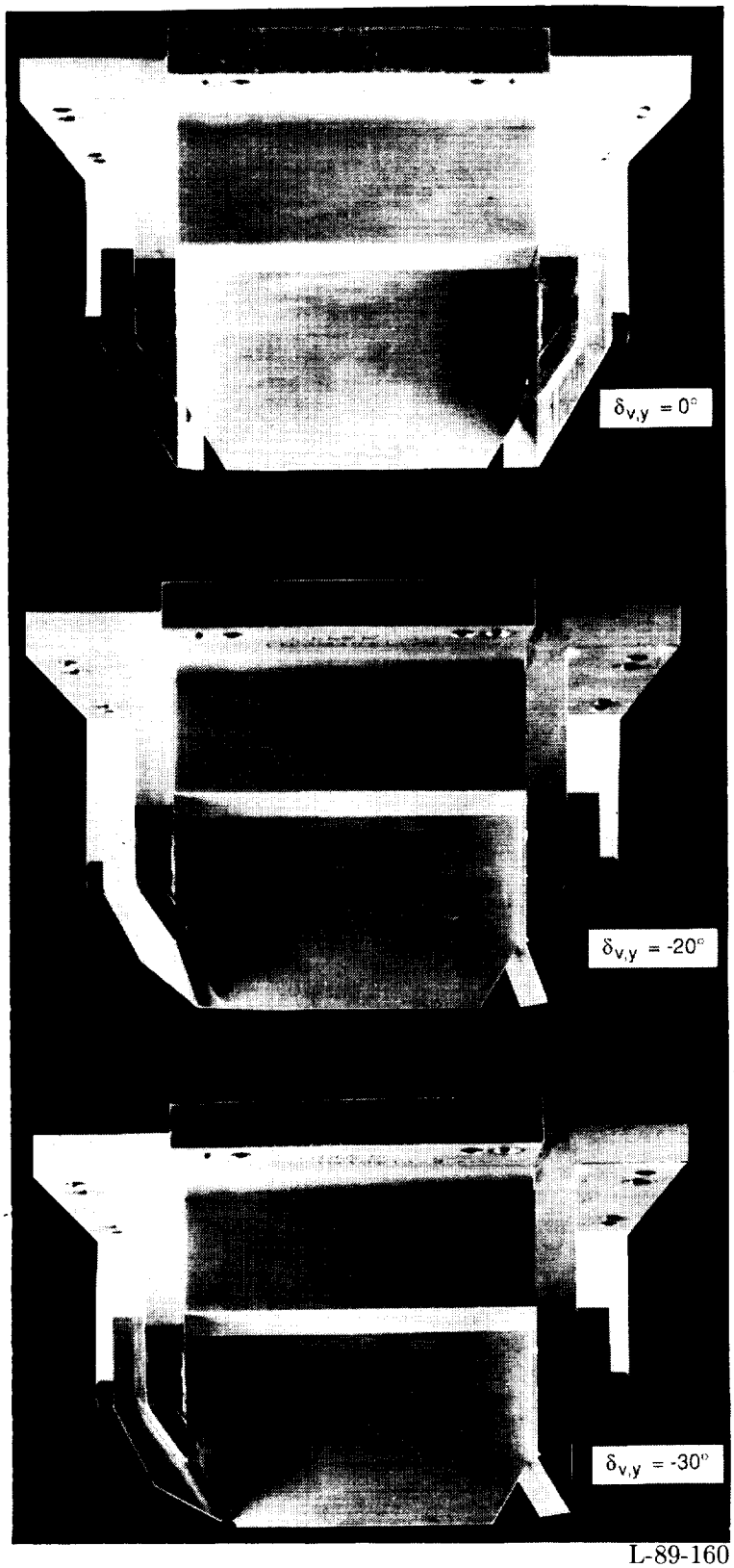

L-89-160

(a) $(x_s - x_t)/l_s = 0.67$; $l_y/l_s = 0.33$.

Figure 7. Photographs of dry power nozzle configurations ($\delta_{v,p} = 0°$) with different yaw-flap deflection angles at a constant hinge location.

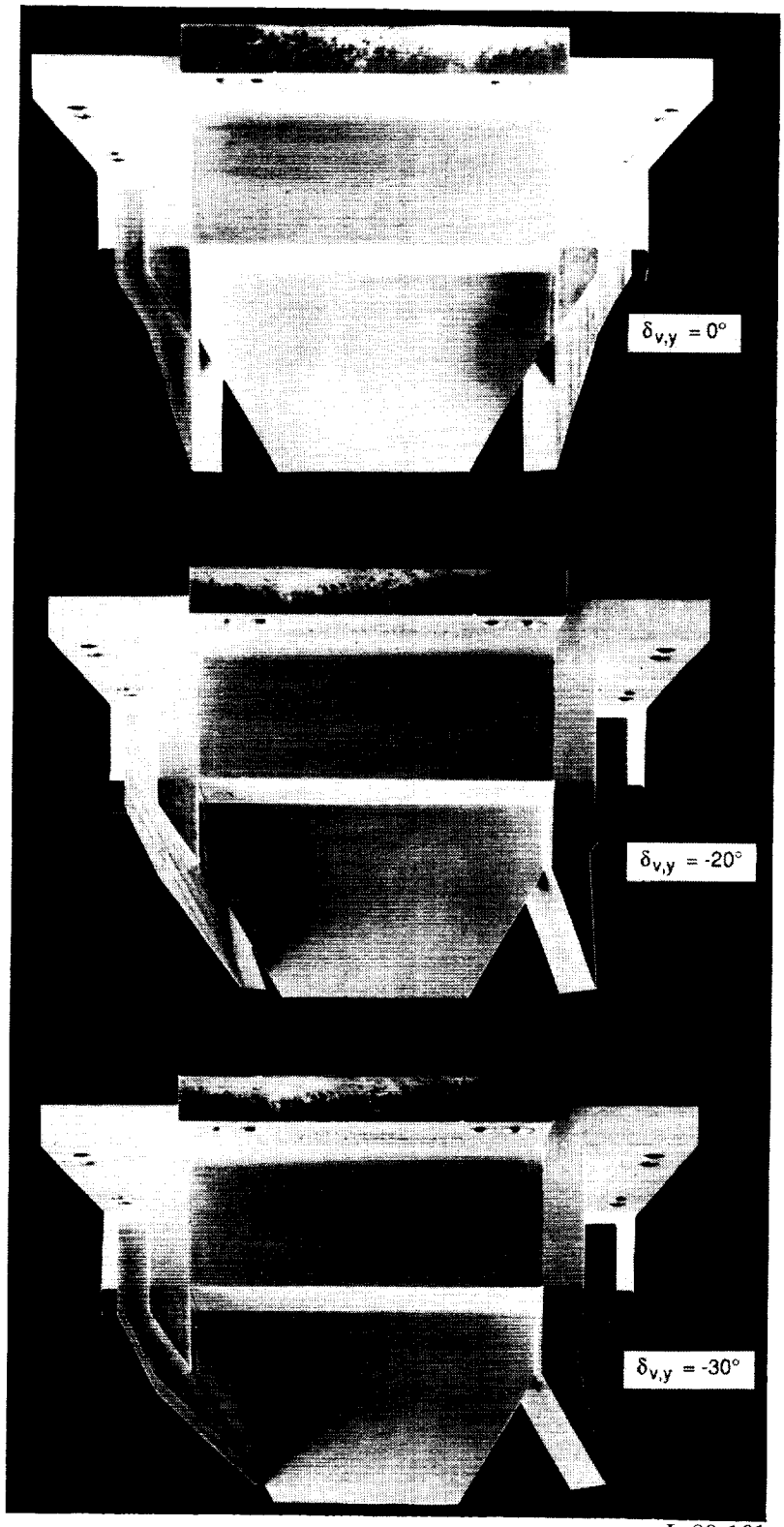

L-89-161

(b) $(x_s - x_t)/l_s = 0.33$; $l_y/l_s = 0.67$.

Figure 7. Continued.

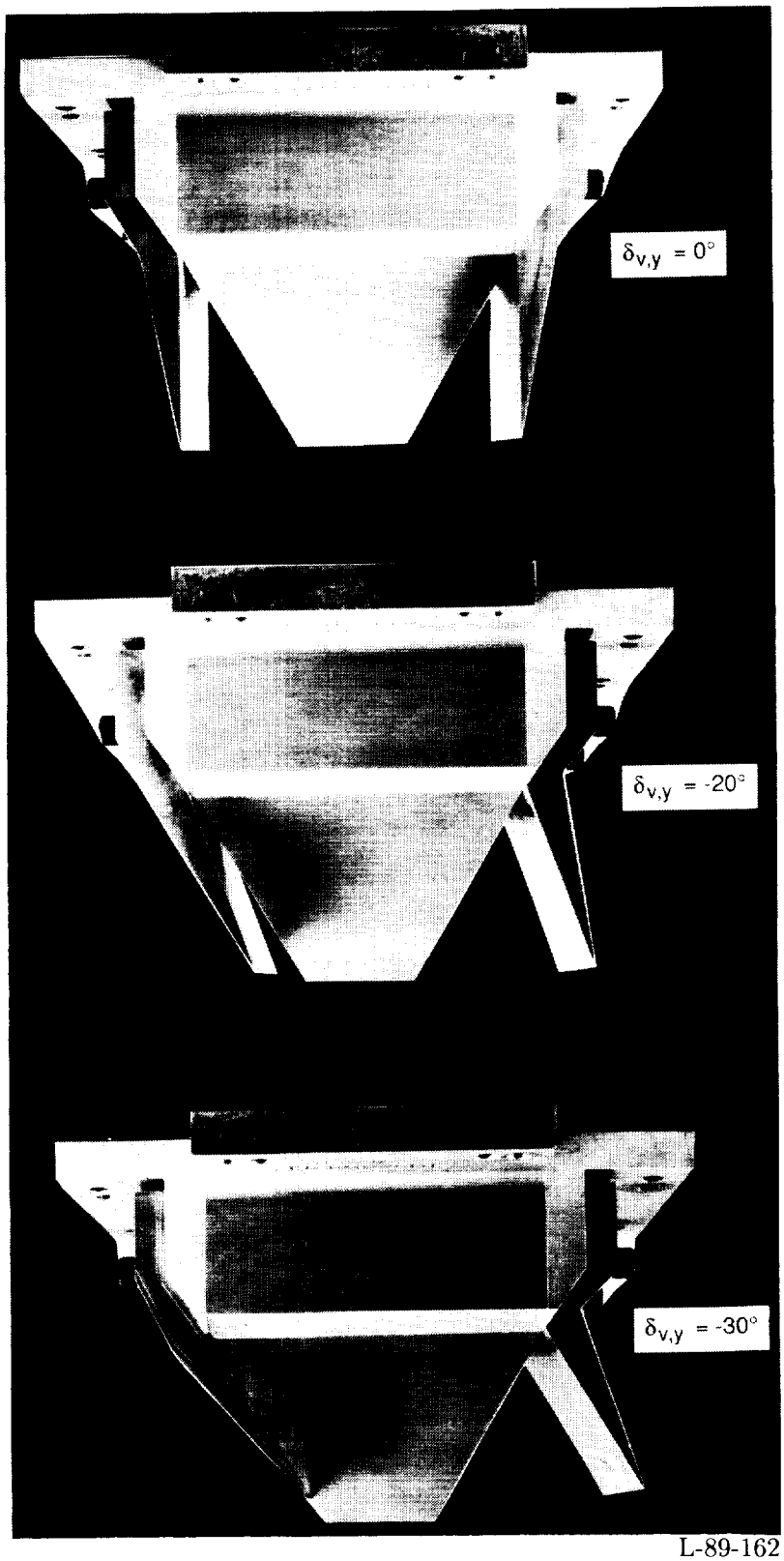

L-89-162

(c) $(x_s - x_t)/l_s = 0$; $l_y/l_s = 1.00$.

Figure 7. Concluded.

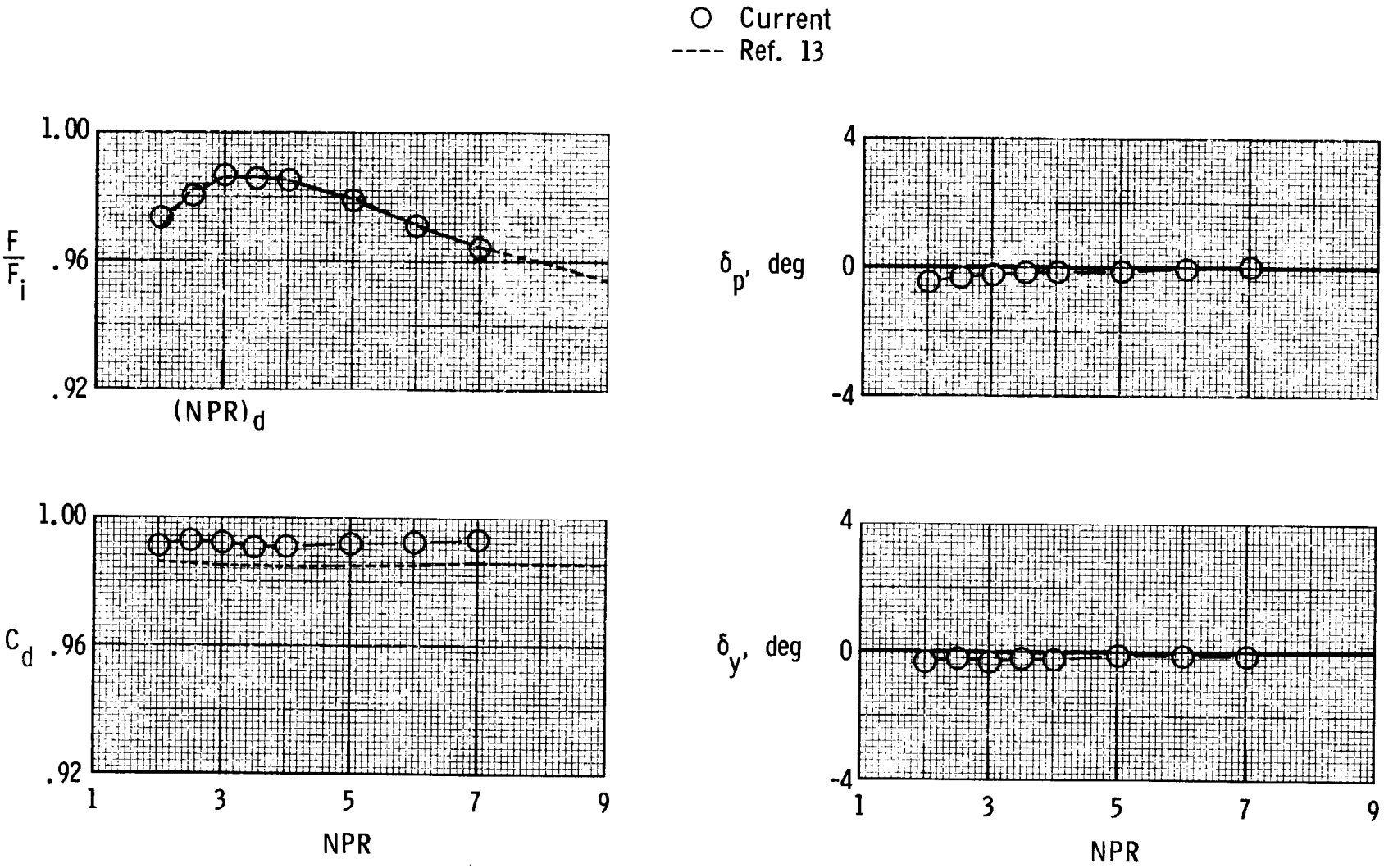

(a) Dry power; $\delta_{v,p} = 0°$.

Figure 8. Variation of internal performance characteristics with nozzle pressure ratio for the baseline nozzles.

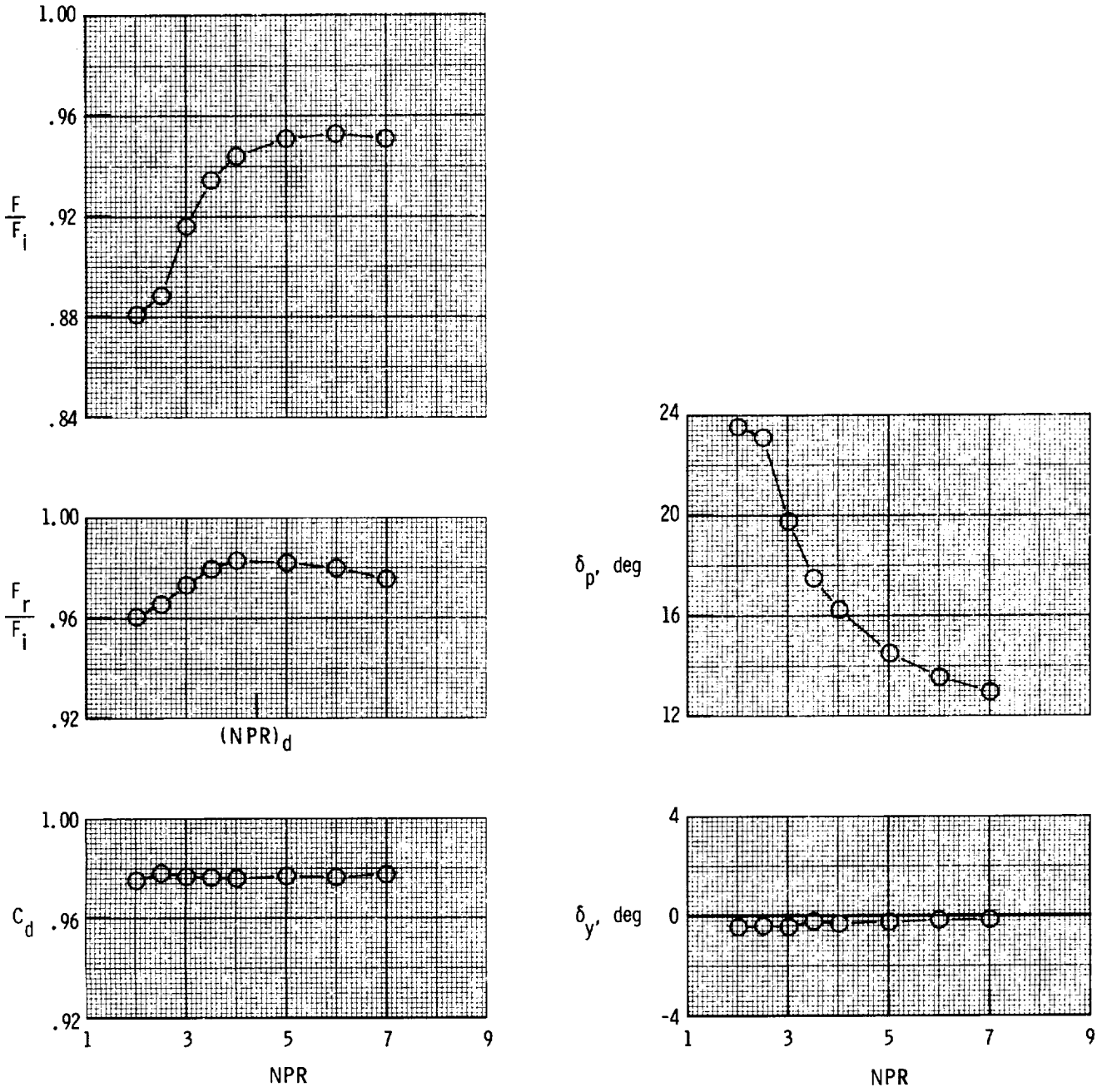

(b) Dry power; $\delta_{v,p} = 19.53°$.

Figure 8. Continued.

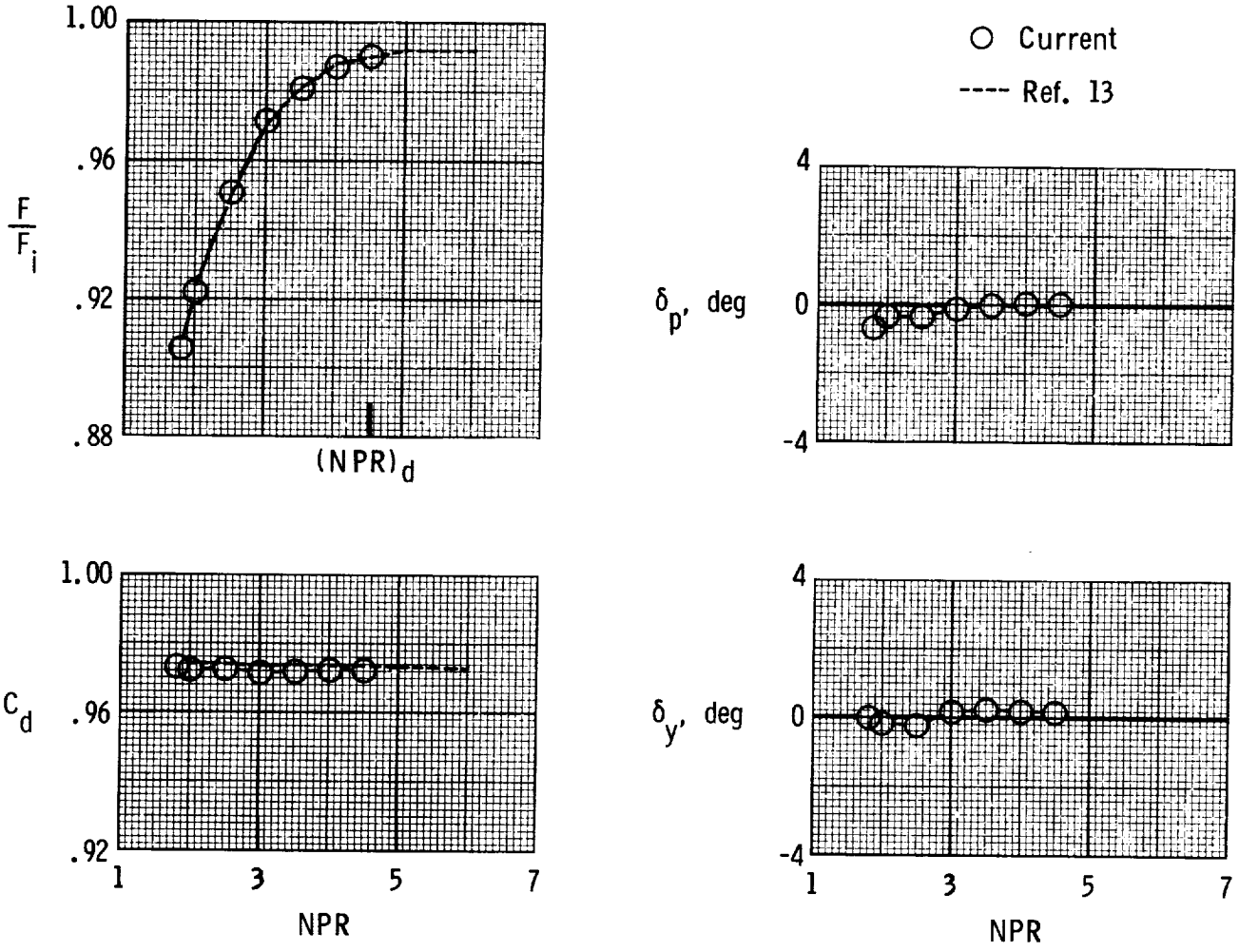

(c) A/B power; $\delta_{v,p} = 0°$.

Figure 8. Continued.

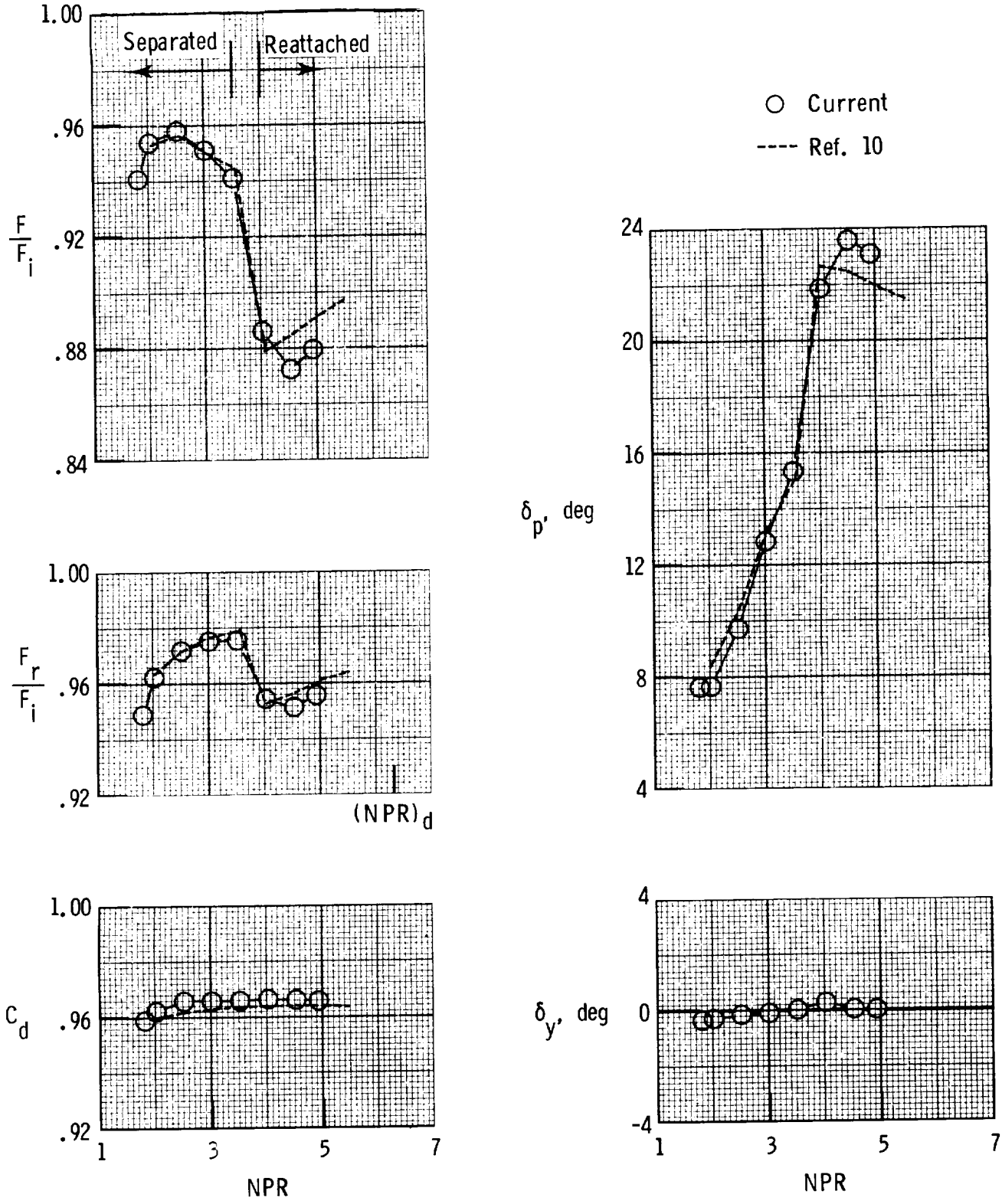

(d) A/B power; $\delta_{v,p} = 20.26°$.

Figure 8. Concluded.

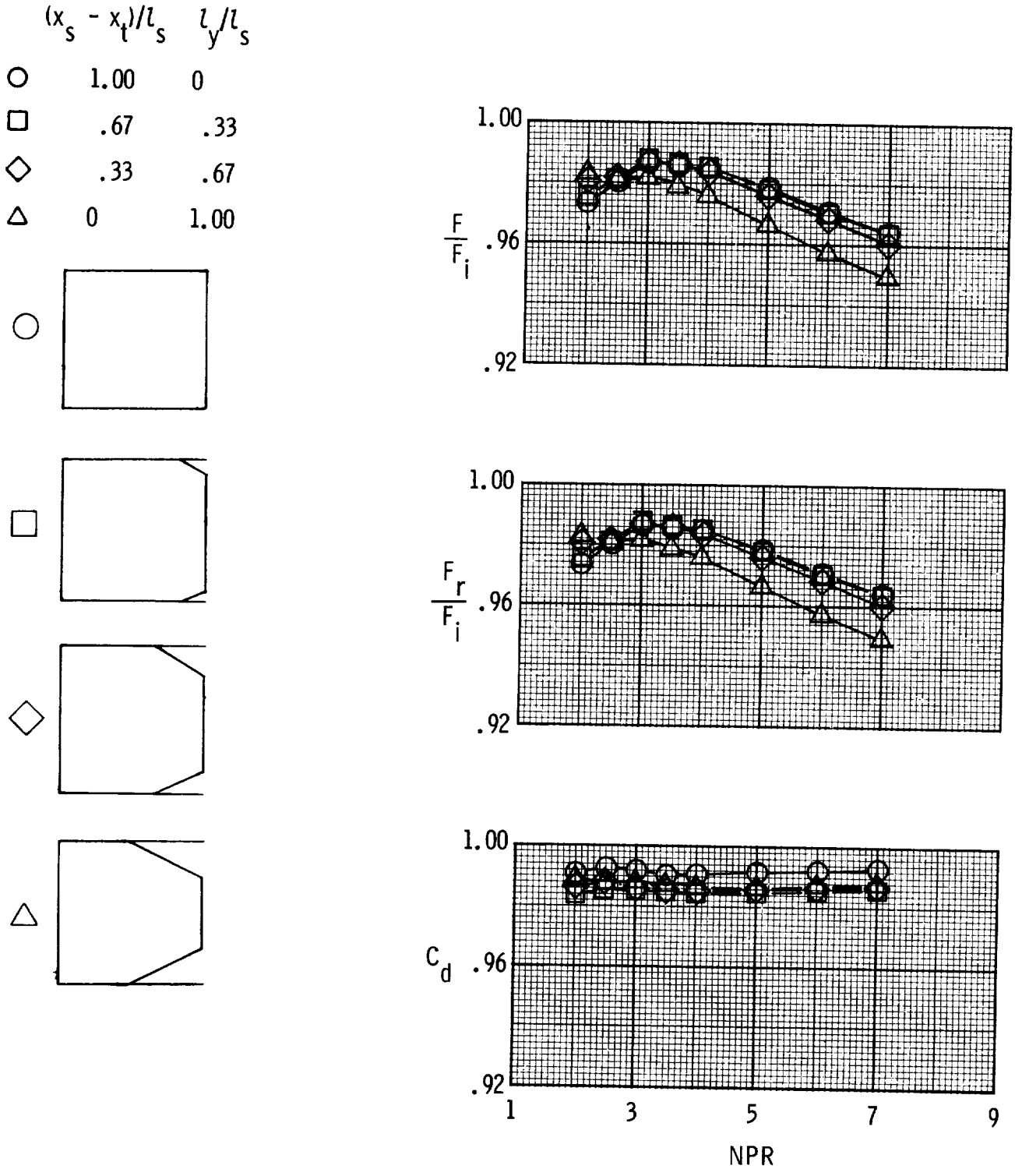

(a) Dry power; $\delta_{v,p} = 0°$.

Figure 9. Effect of divergent flap cutout on nozzle internal performance characteristics for $\delta_{v,y} = 0°$.

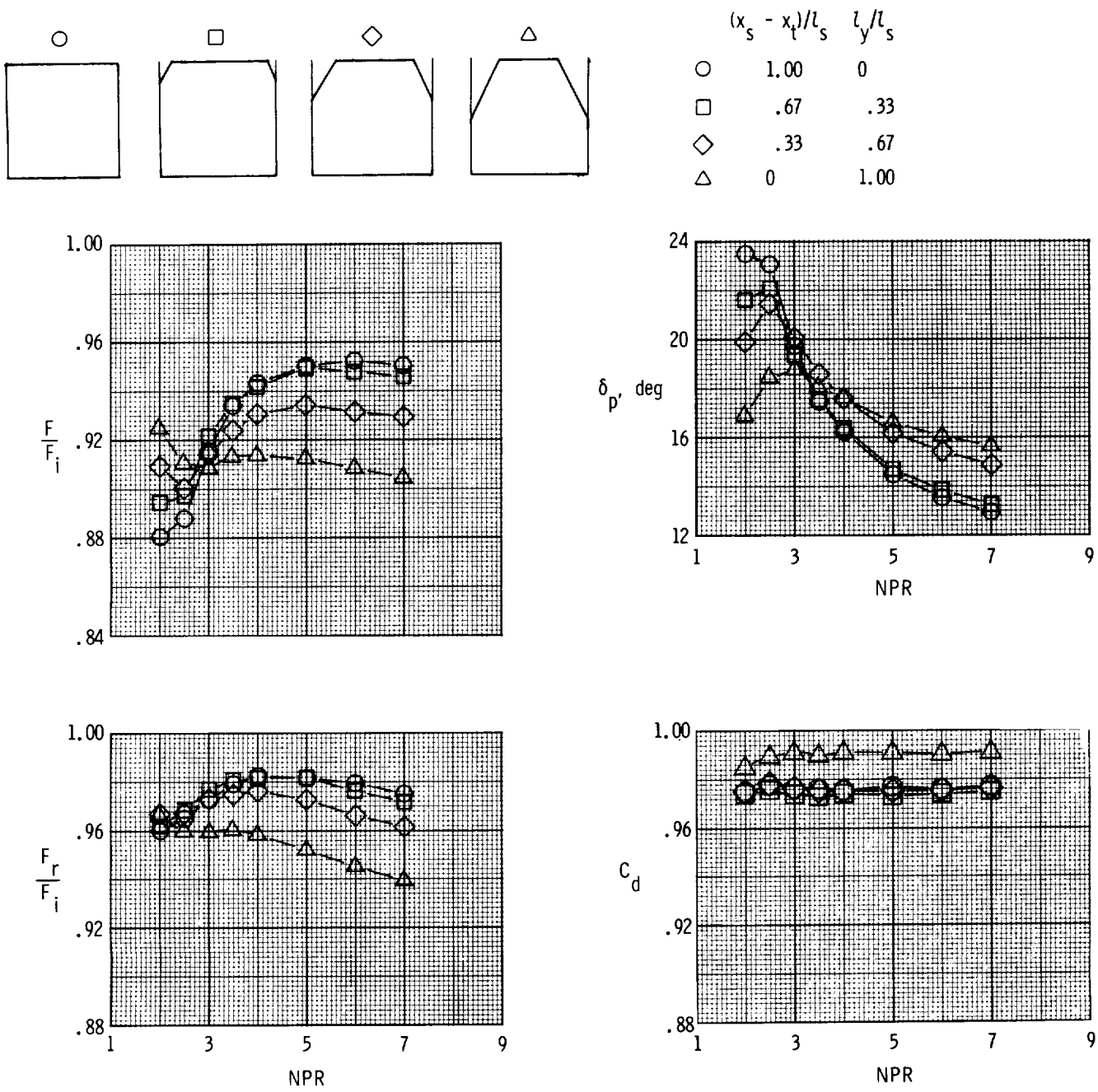

(b) Dry power; $\delta_{v,p} = 19.53°$.

Figure 9. Continued.

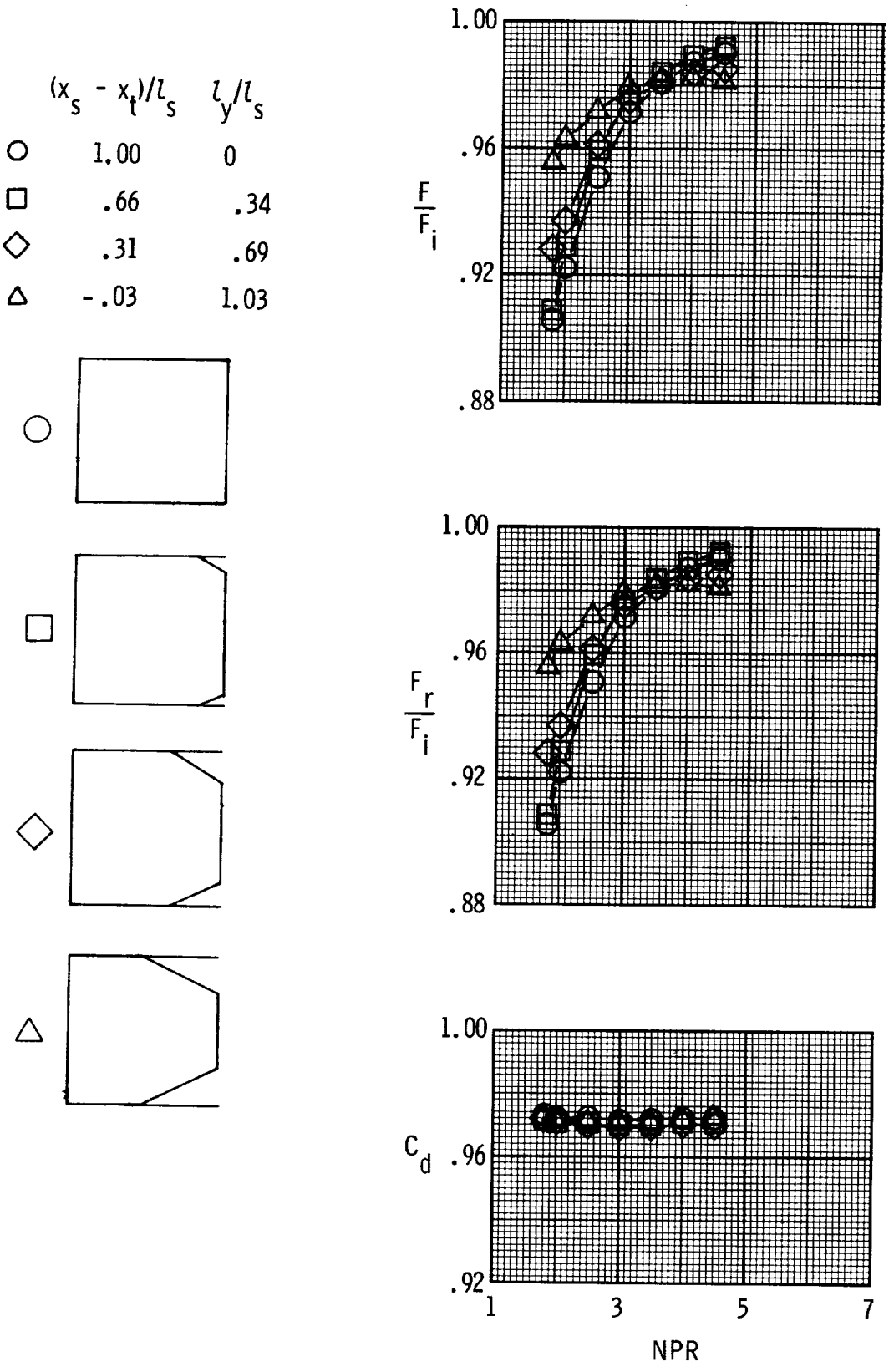

(c) A/B power; $\delta_{v,p} = 0°$.

Figure 9. Continued.

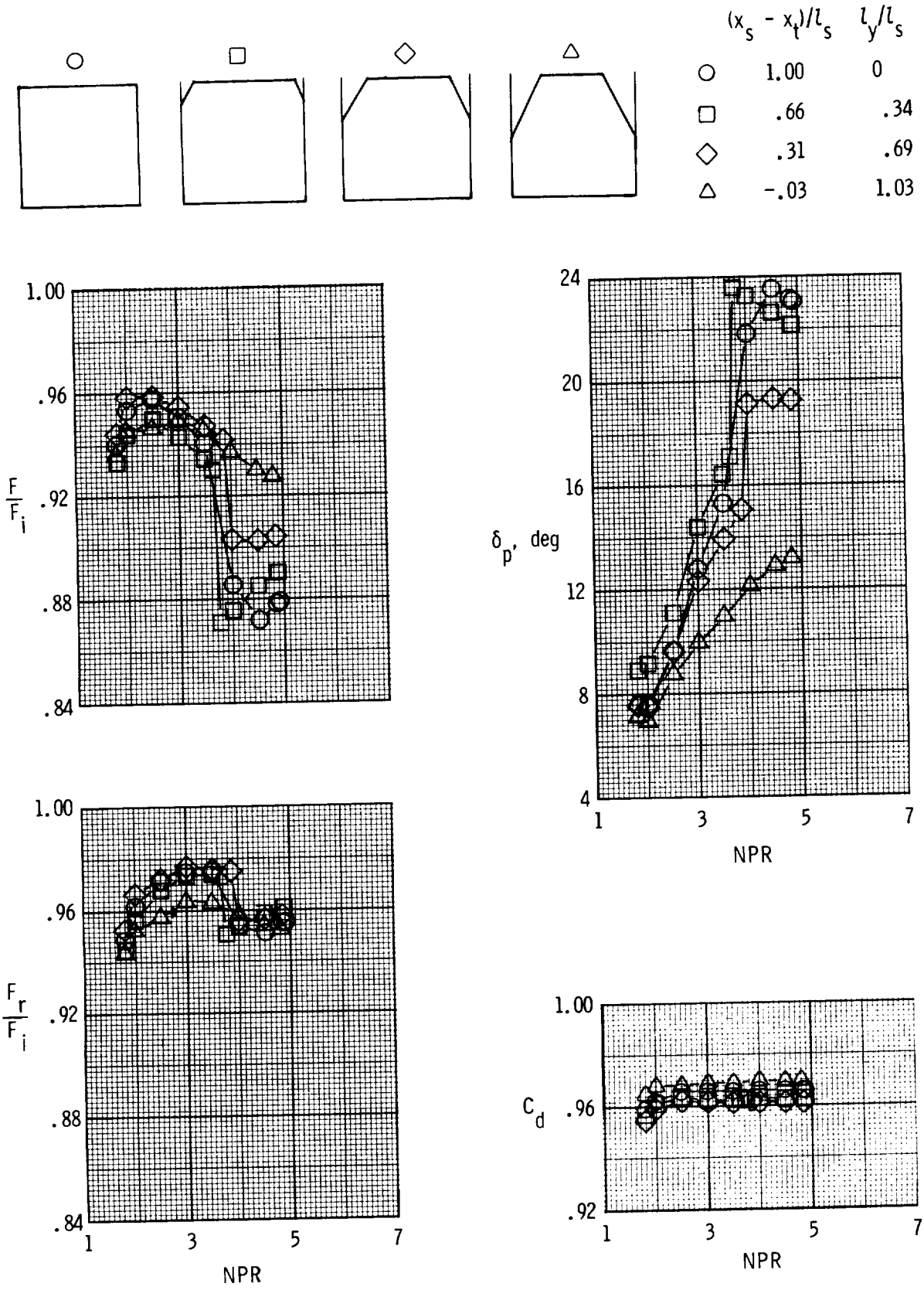

(d) A/B power; $\delta_{v,p} = 20.26°$.

Figure 9. Concluded.

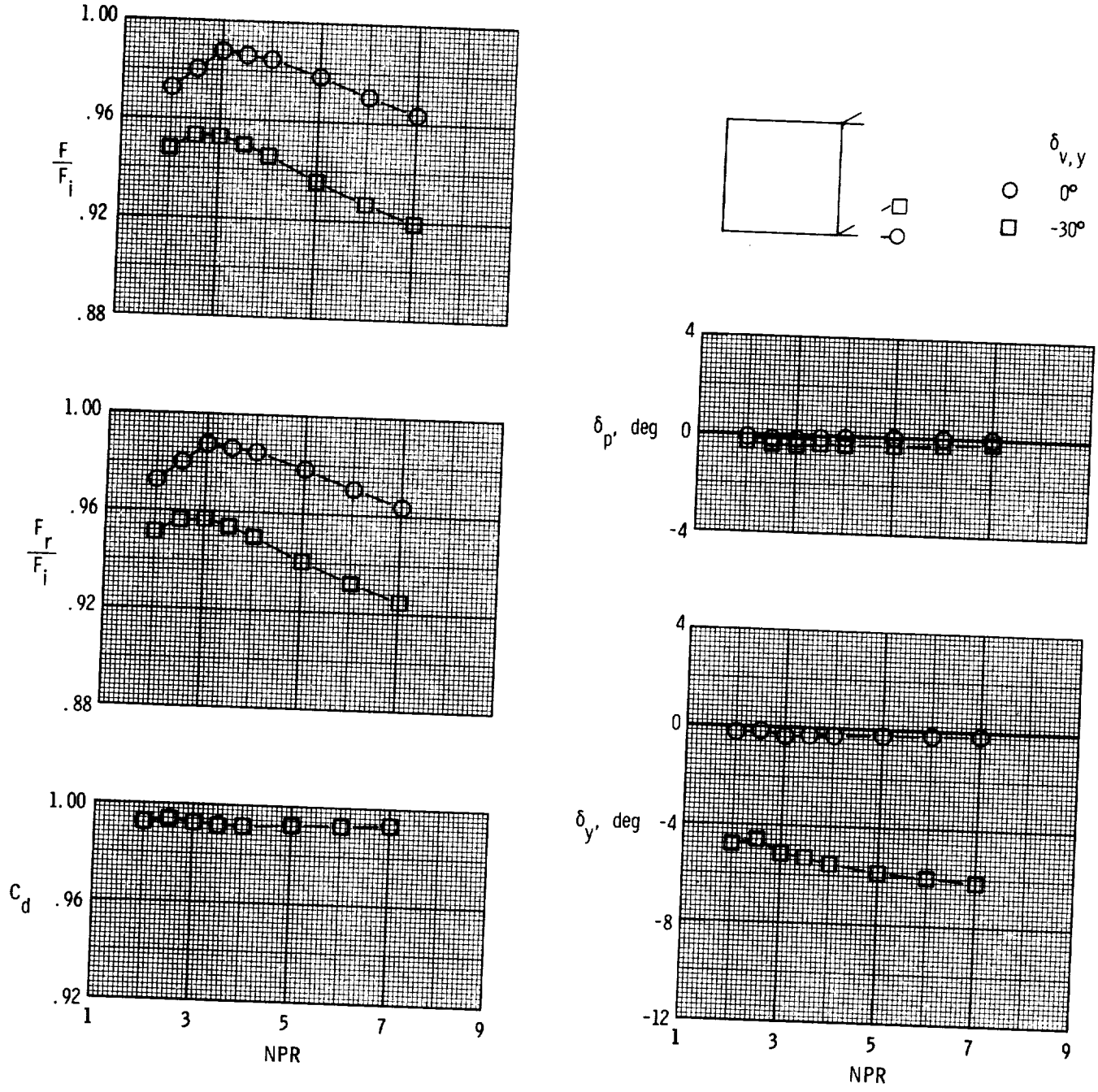

(a) $l_y/l_s = 0.33$.

Figure 10. Effect of yaw-flap deflection on internal performance characteristics of dry power nozzle for $\delta_{v,p} = 0°$ and $(x_s - x_t)/l_s = 1.00$.

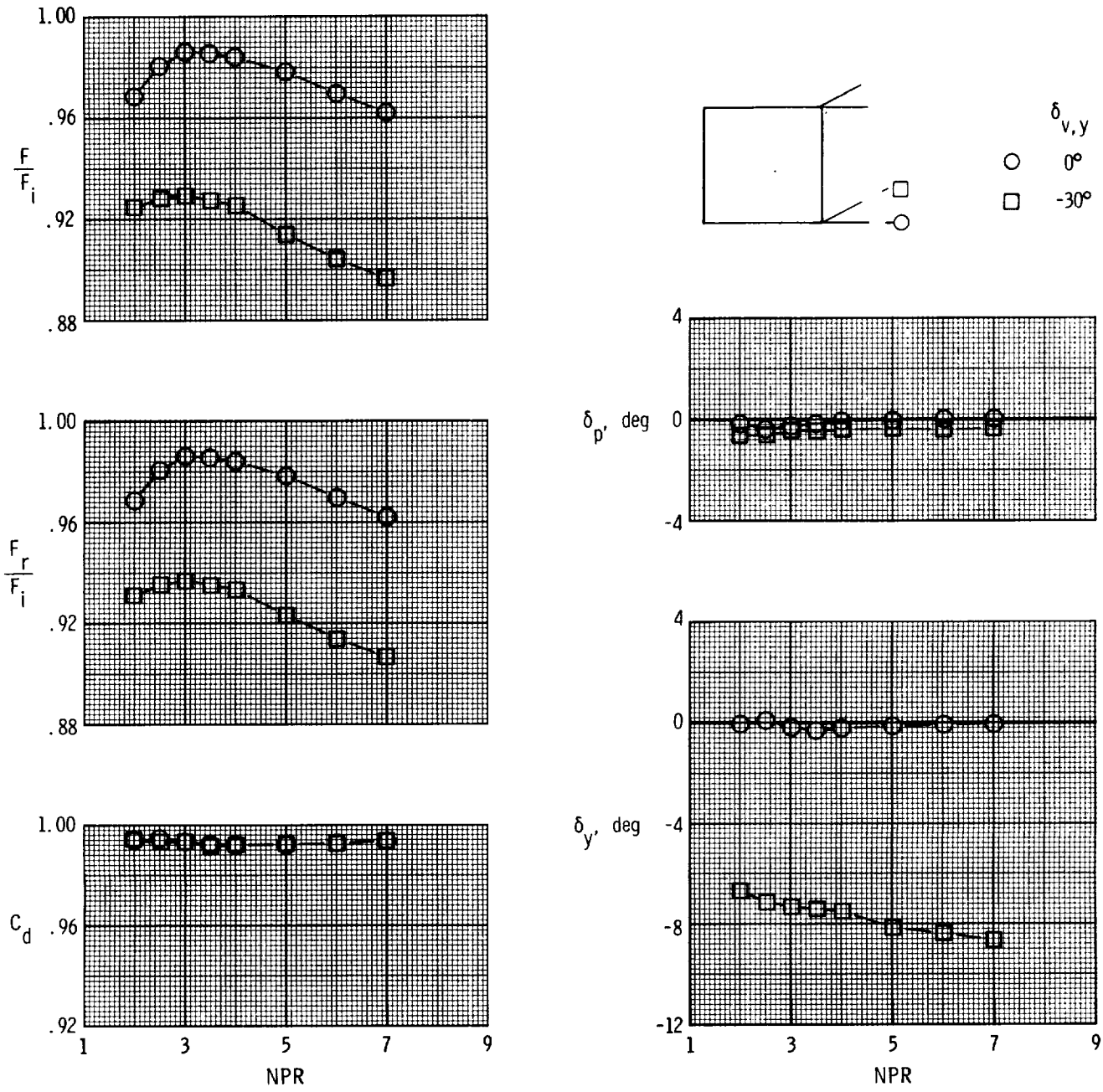

(b) $l_y/l_s = 0.67$.

Figure 10. Continued.

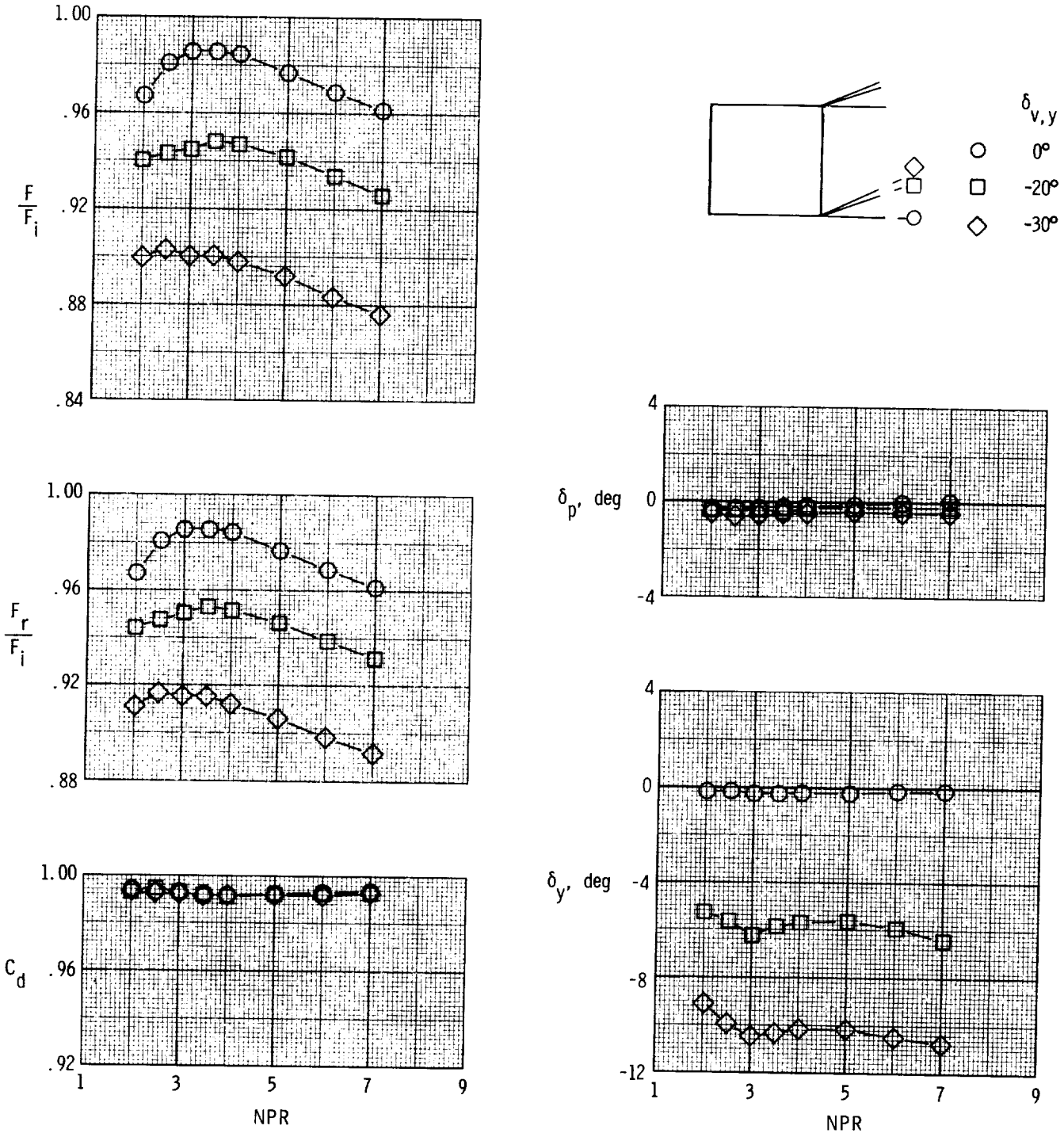

(c) $l_y/l_s = 1.00$.

Figure 10. Concluded.

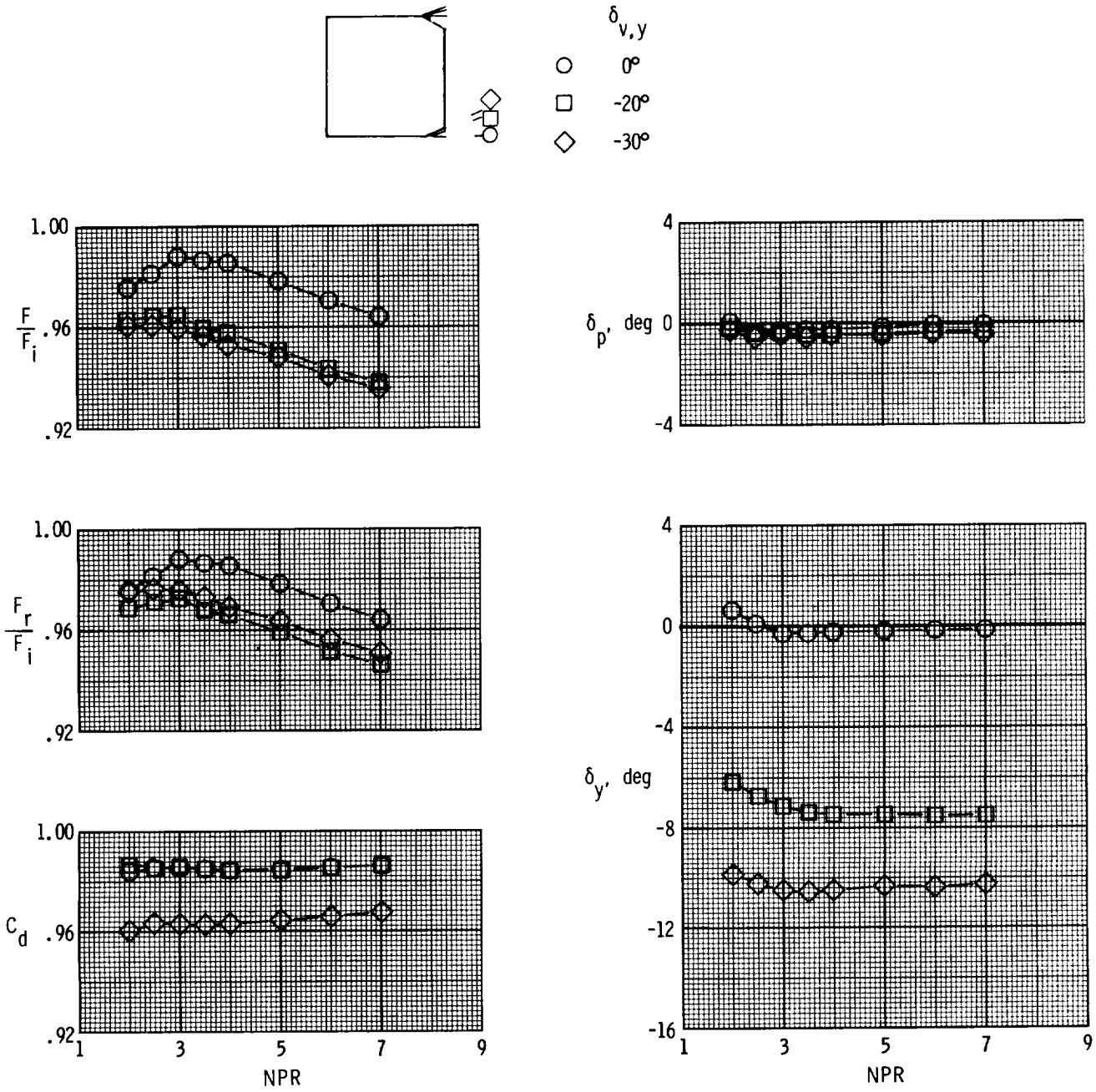

(a) $l_y/l_s = 0.33$.

Figure 11. Effect of yaw-flap deflection on internal performance characteristics of dry power nozzle for $\delta_{v,p} = 0°$ and $(x_s - x_t)/l_s = 0.67$.

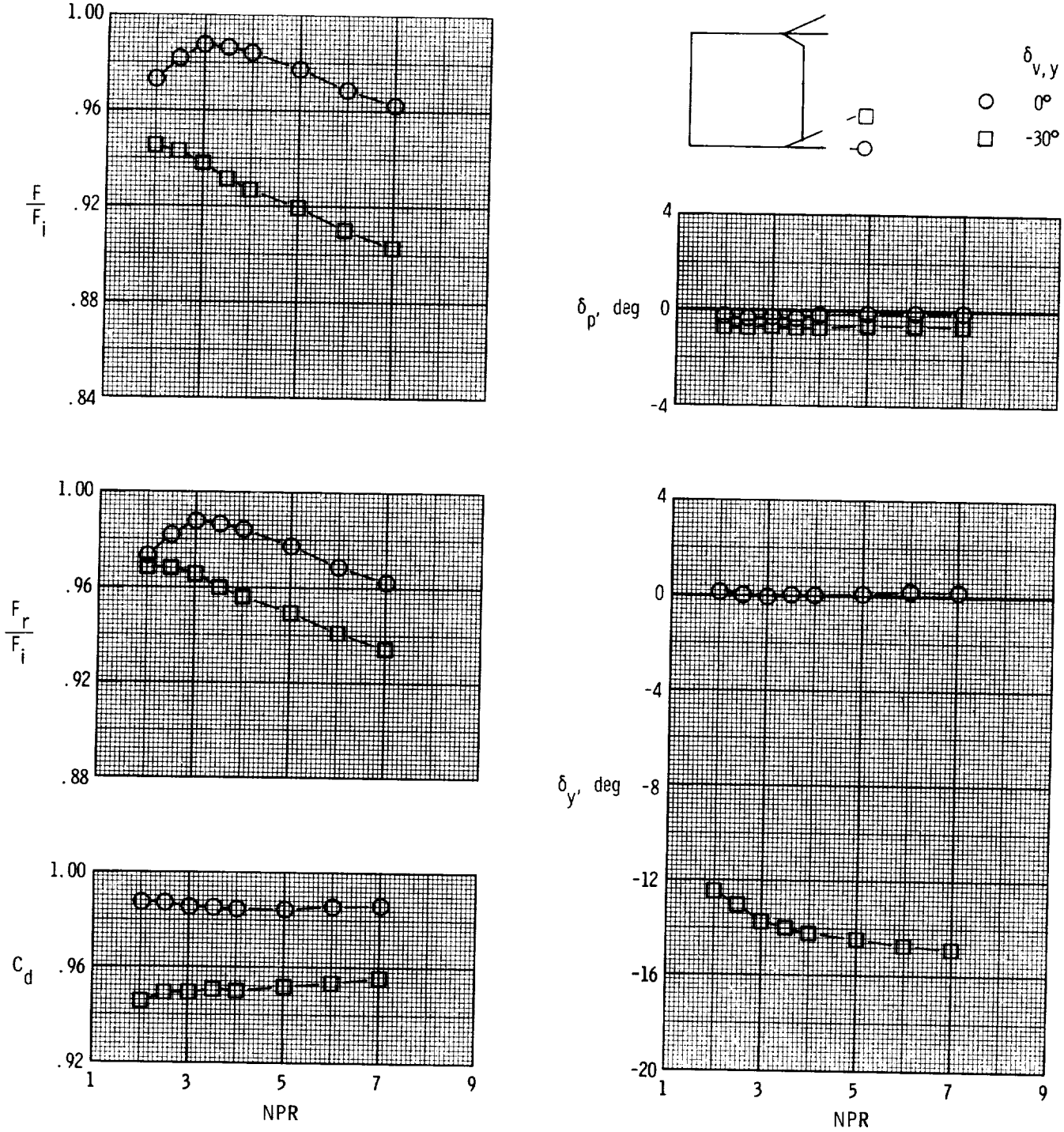

(b) $l_y/l_s = 0.67$.

Figure 11. Continued.

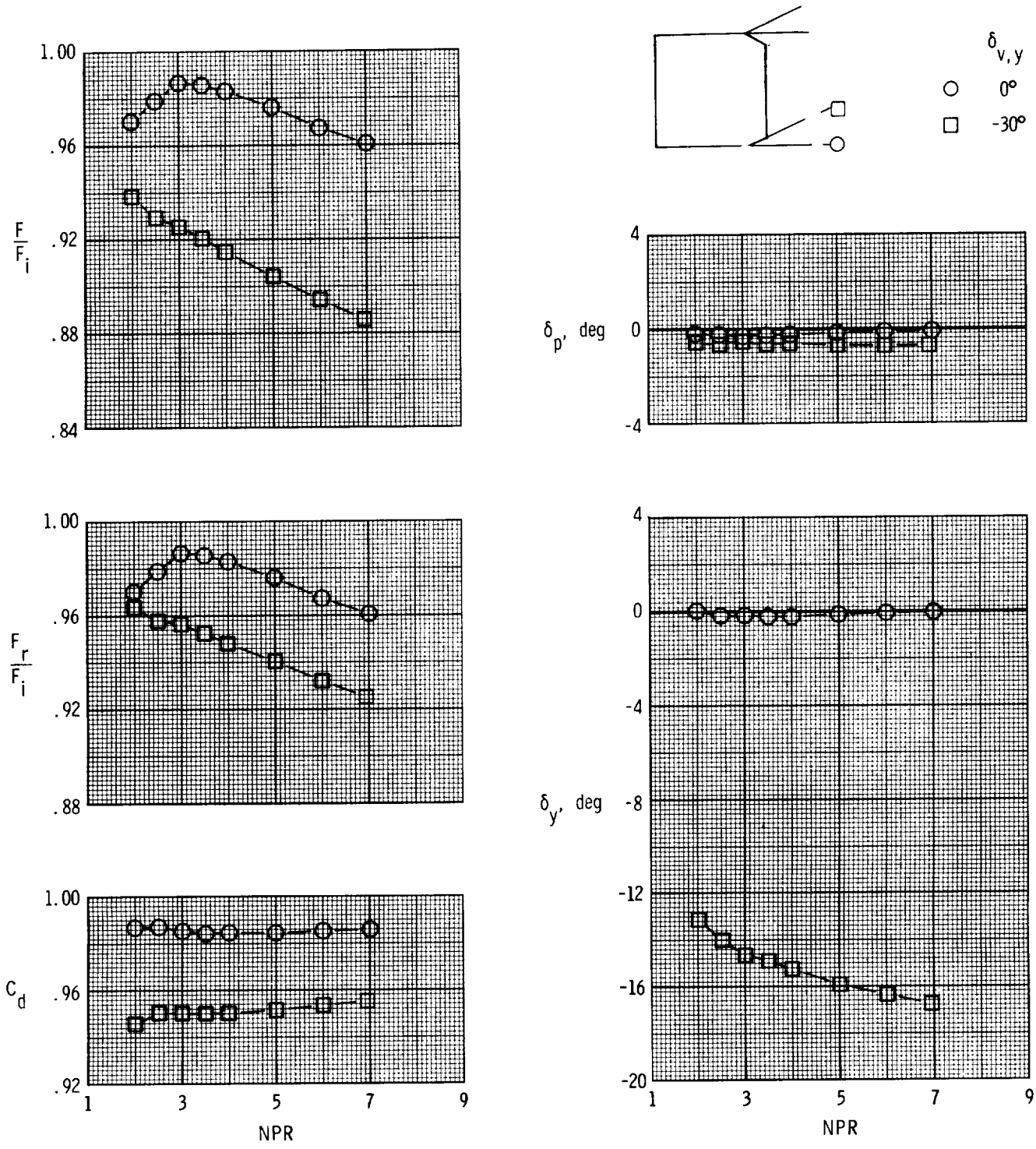

(c) $l_y/l_s = 1.00$.

Figure 11. Concluded.

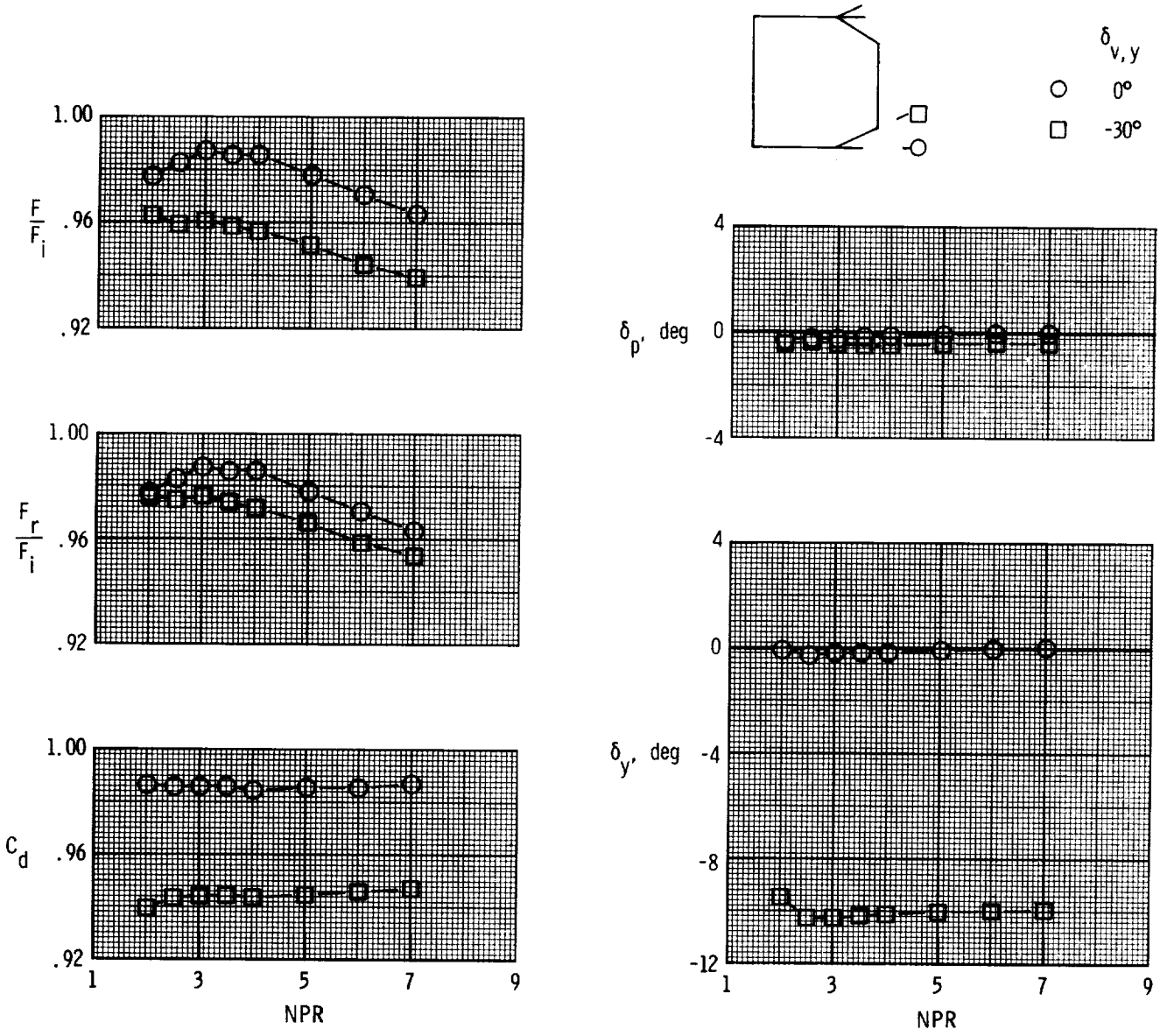

(a) $l_y/l_s = 0.33$.

Figure 12. Effect of yaw-flap deflection on internal performance characteristics of dry power nozzle for $\delta_{v,p} = 0°$ and $(x_s - x_t)/l_s = 0.33$.

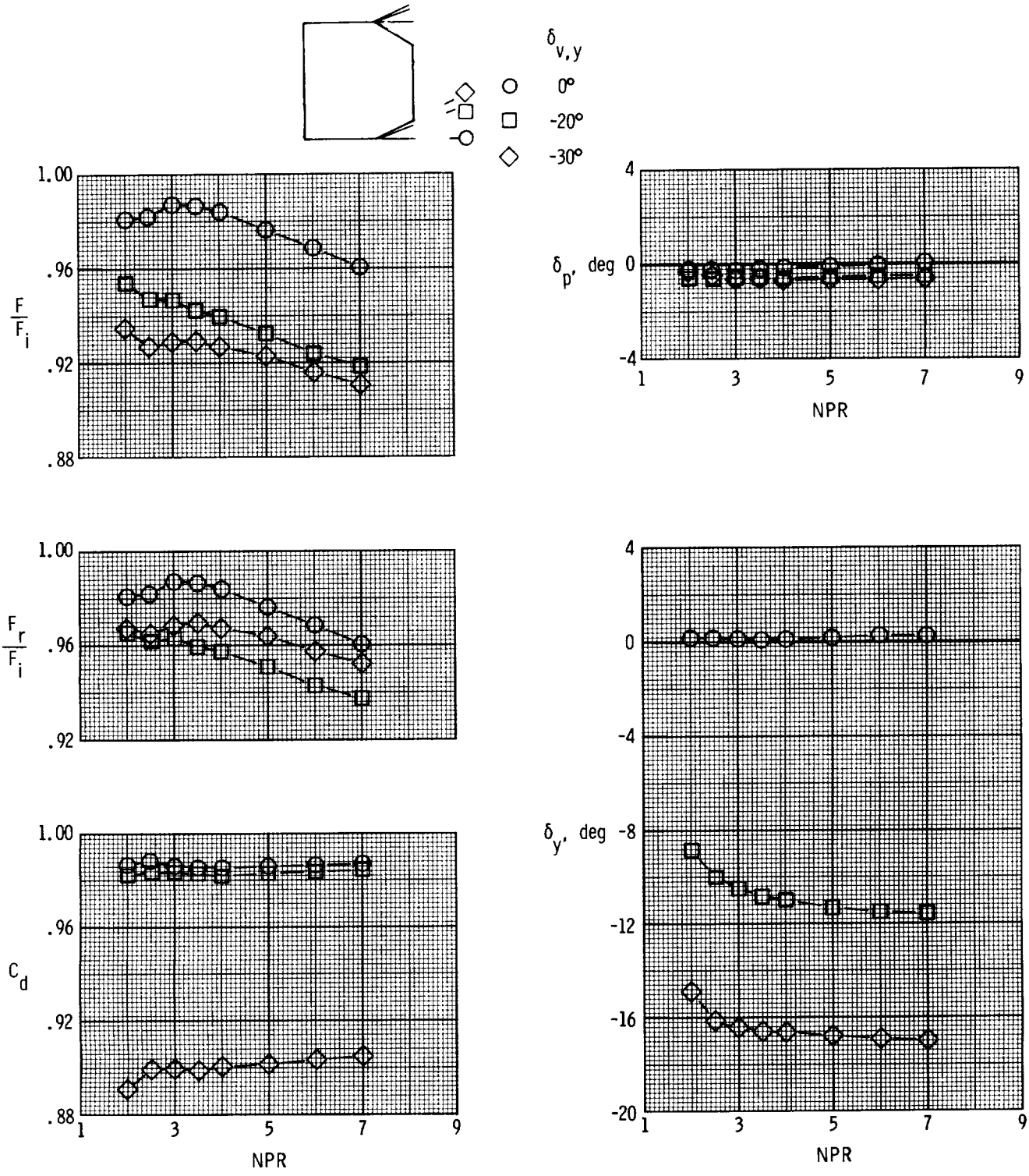

(b) $l_y/l_s = 0.67$.

Figure 12. Continued.

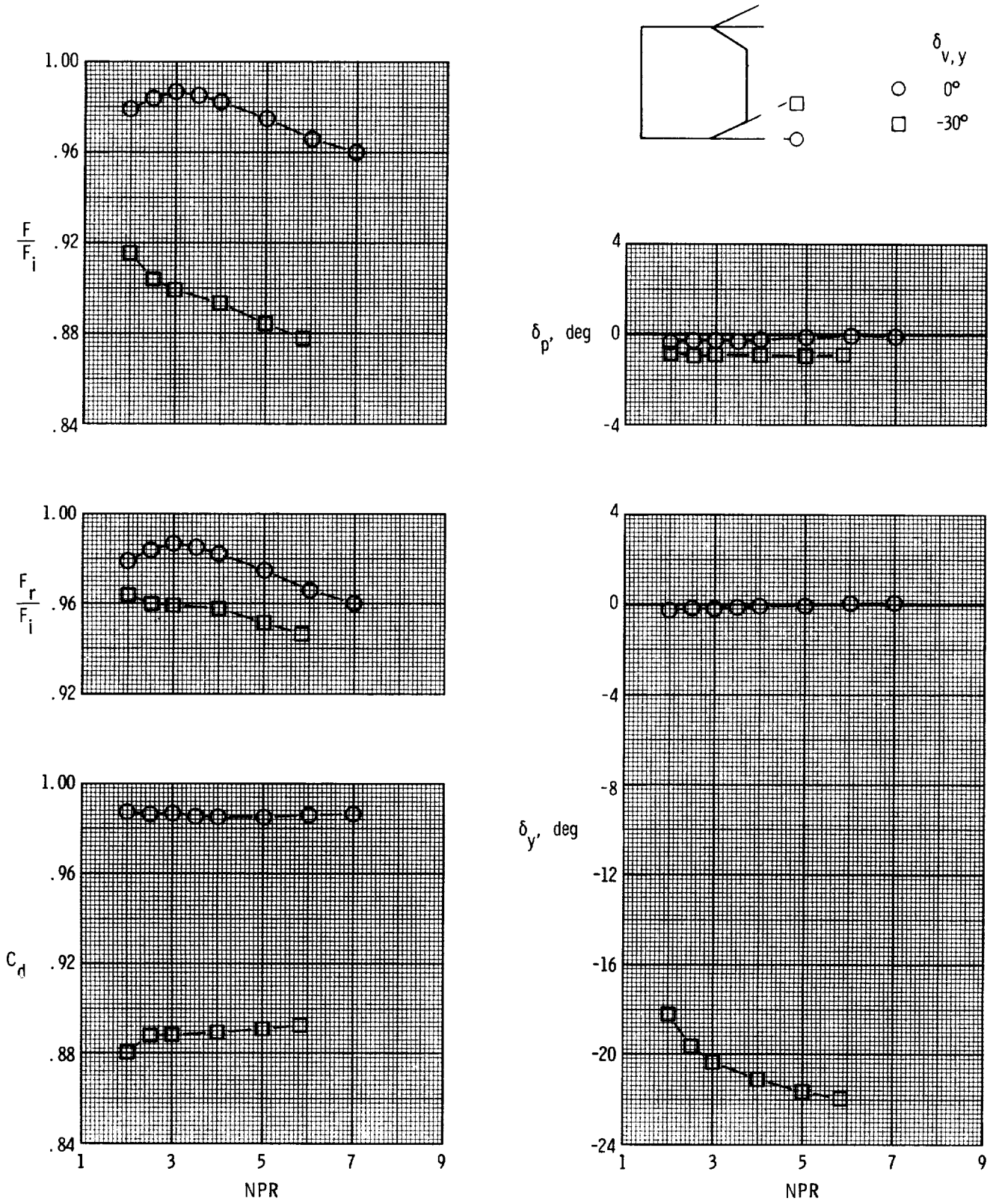

(c) $l_y/l_s = 1.00$.

Figure 12. Concluded.

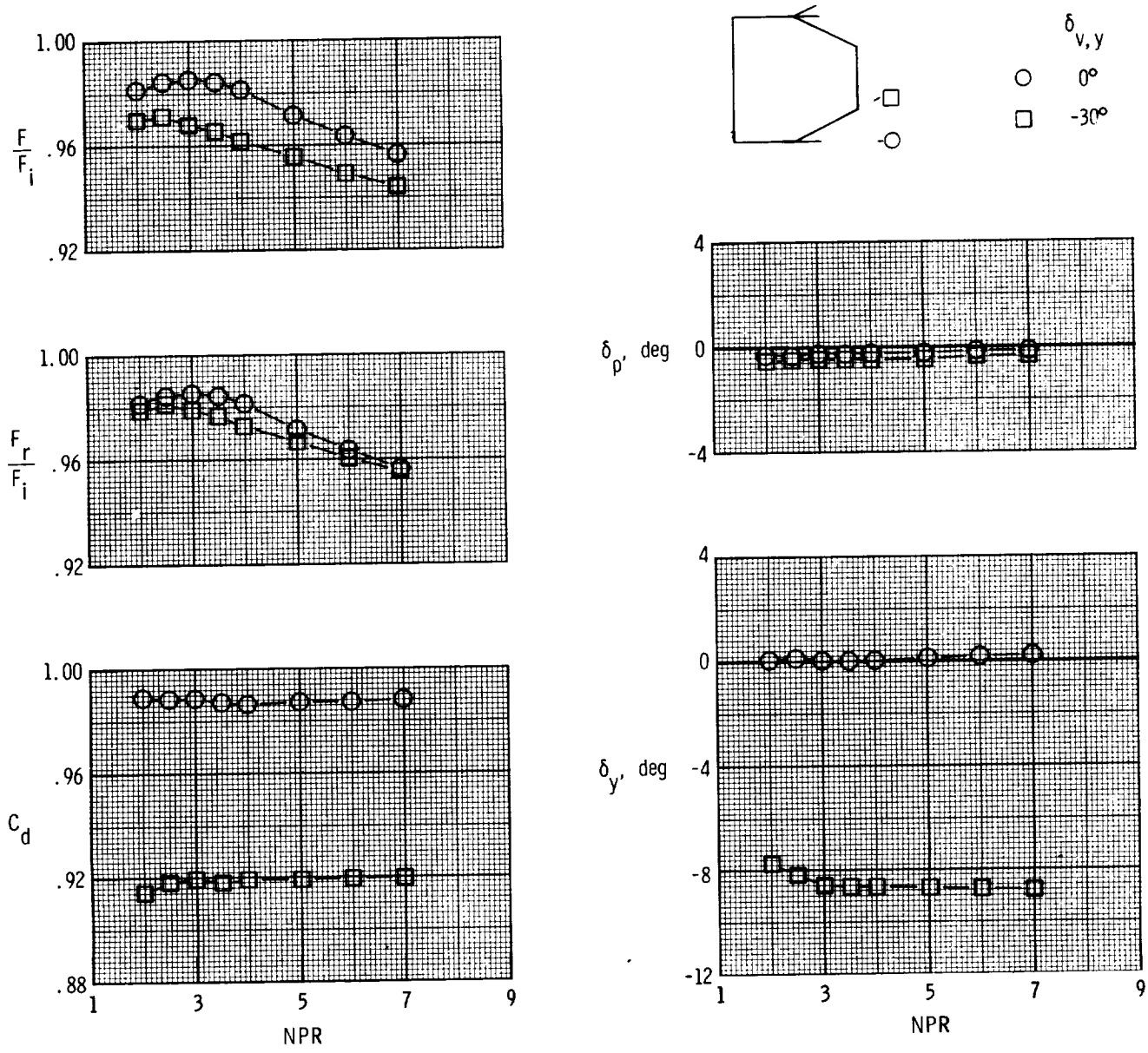

(a) $l_y/l_s = 0.33$.

Figure 13. Effect of yaw-flap deflection on internal performance characteristics of dry power nozzle for $\delta_{v,p} = 0°$ and $(x_s - x_t)/l_s = 0$.

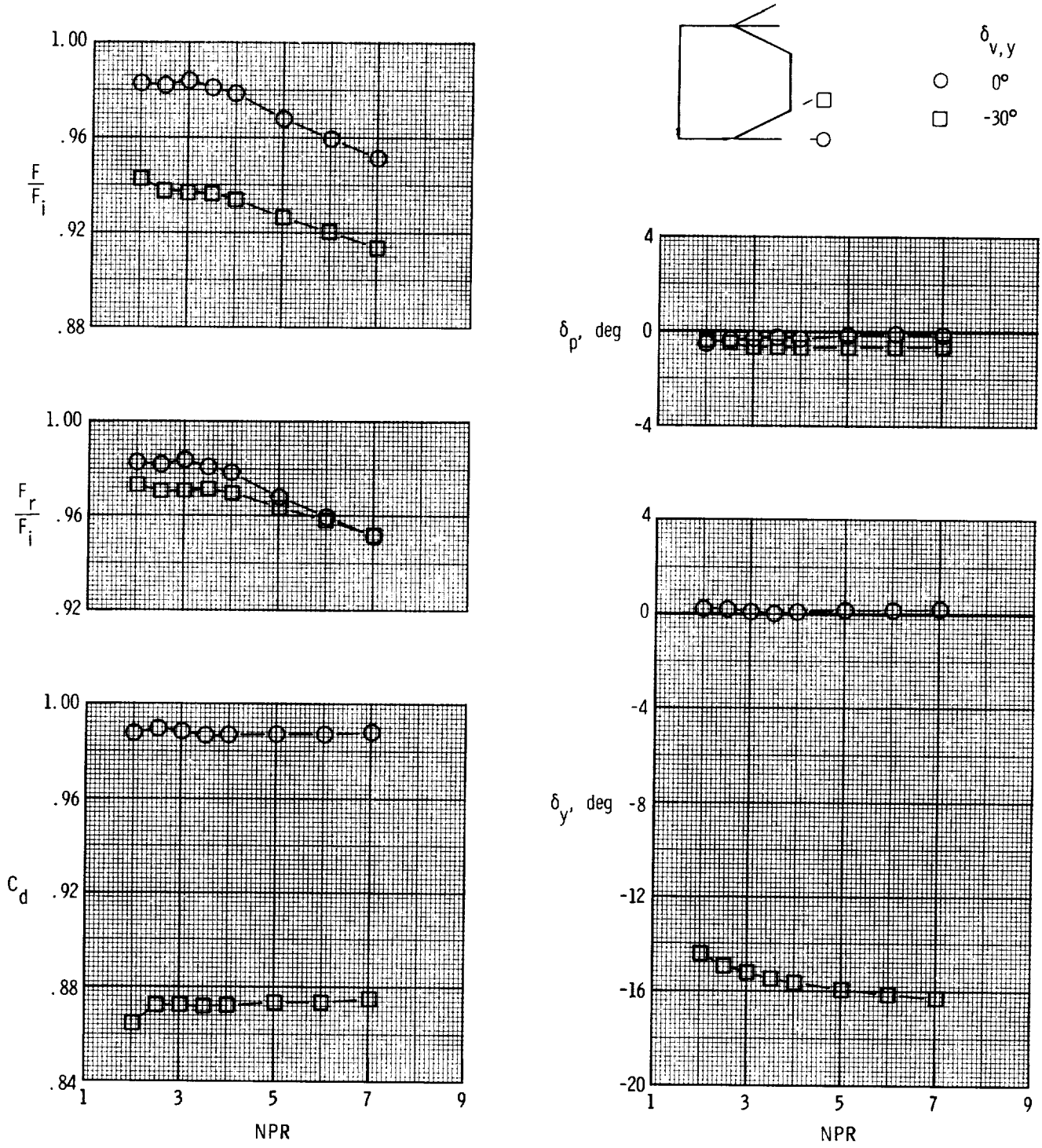

(b) $l_y/l_s = 0.67$.

Figure 13. Continued.

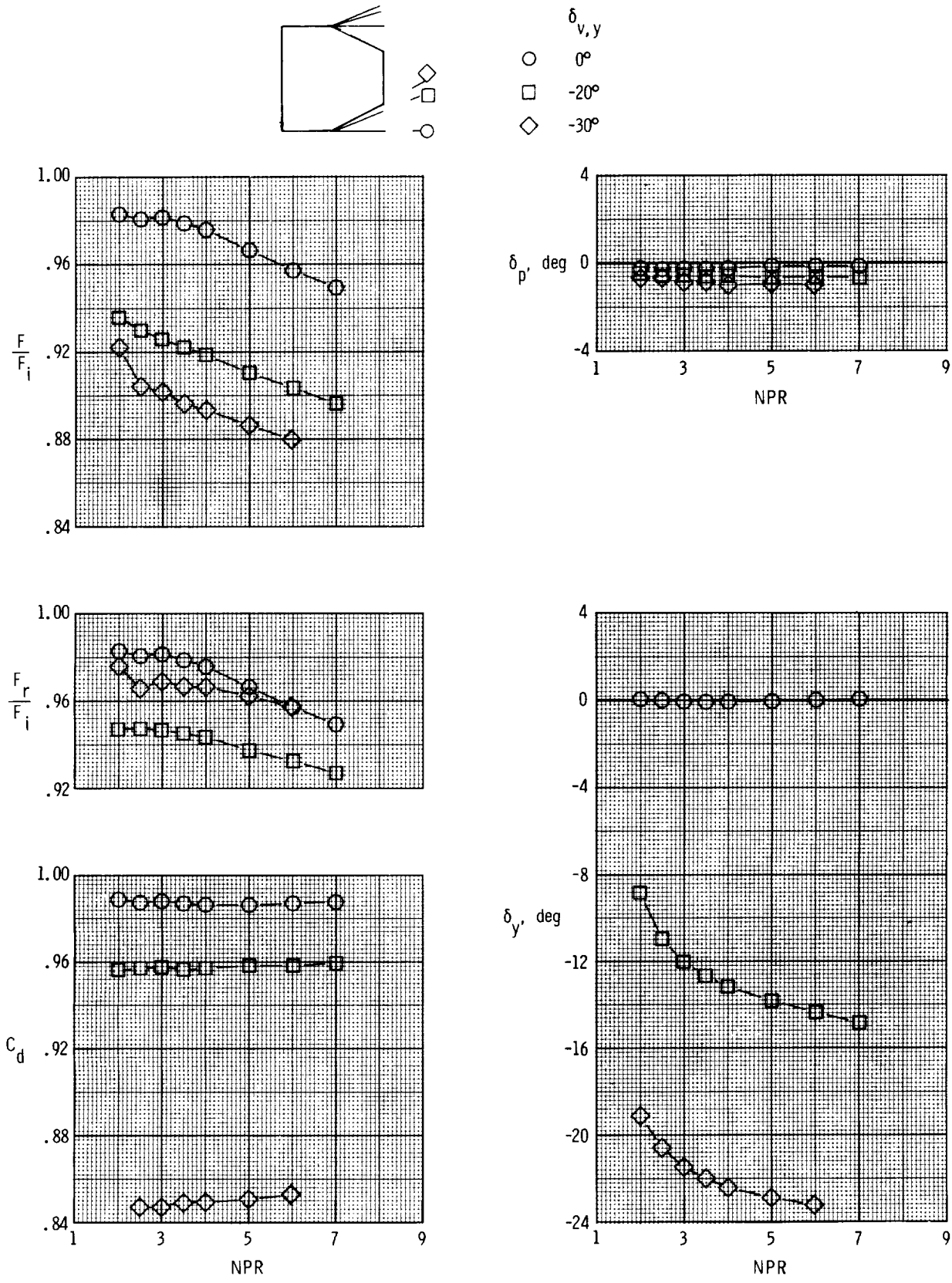

(c) $l_y/l_s = 1.00$.

Figure 13. Concluded.

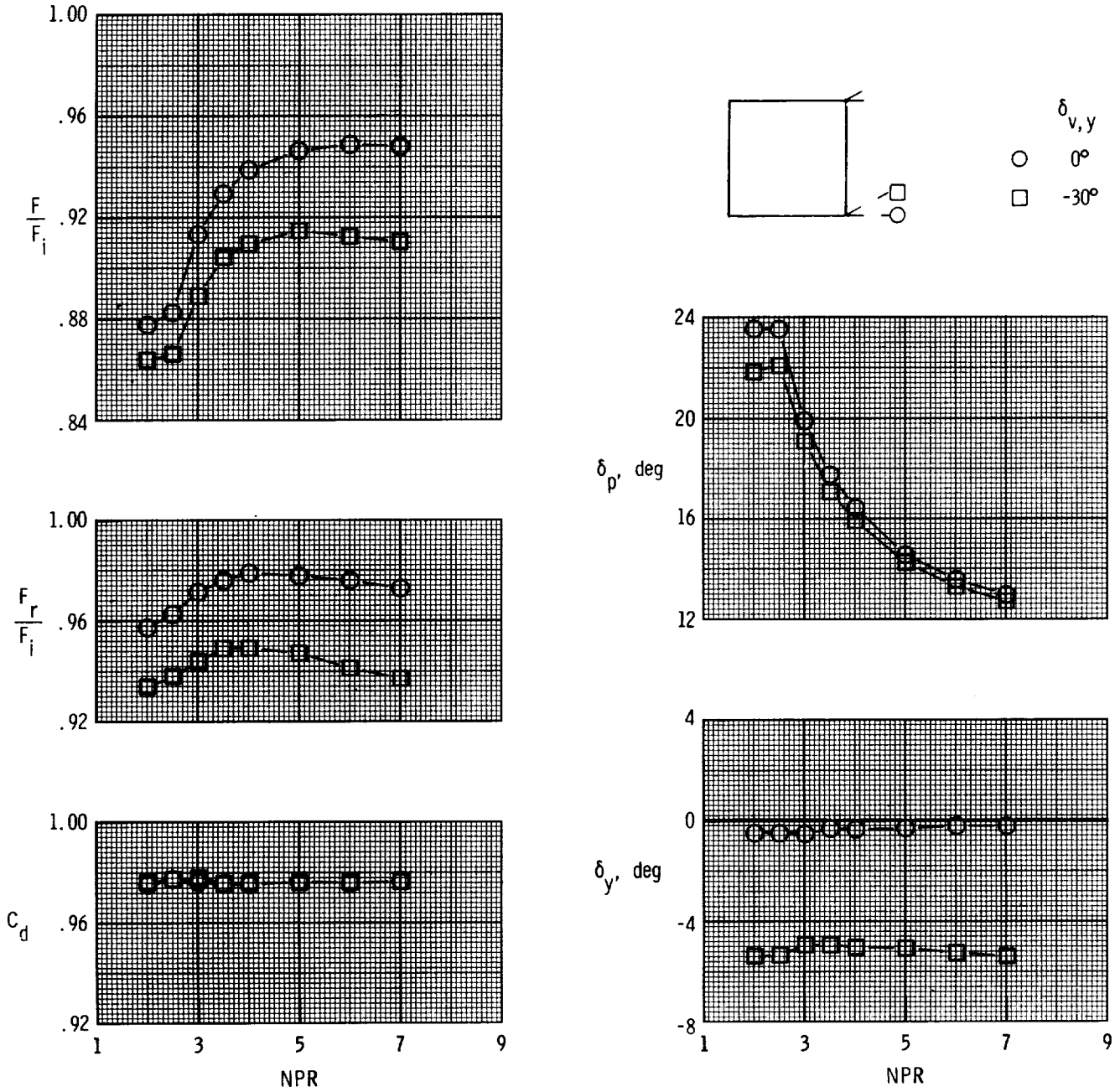

(a) $l_y/l_s = 0.33$.

Figure 14. Effect of yaw-flap deflection on internal performance characteristics of dry power nozzle for $\delta_{v,p} = 19.53°$ and $(x_s - x_t)/l_s = 1.00$.

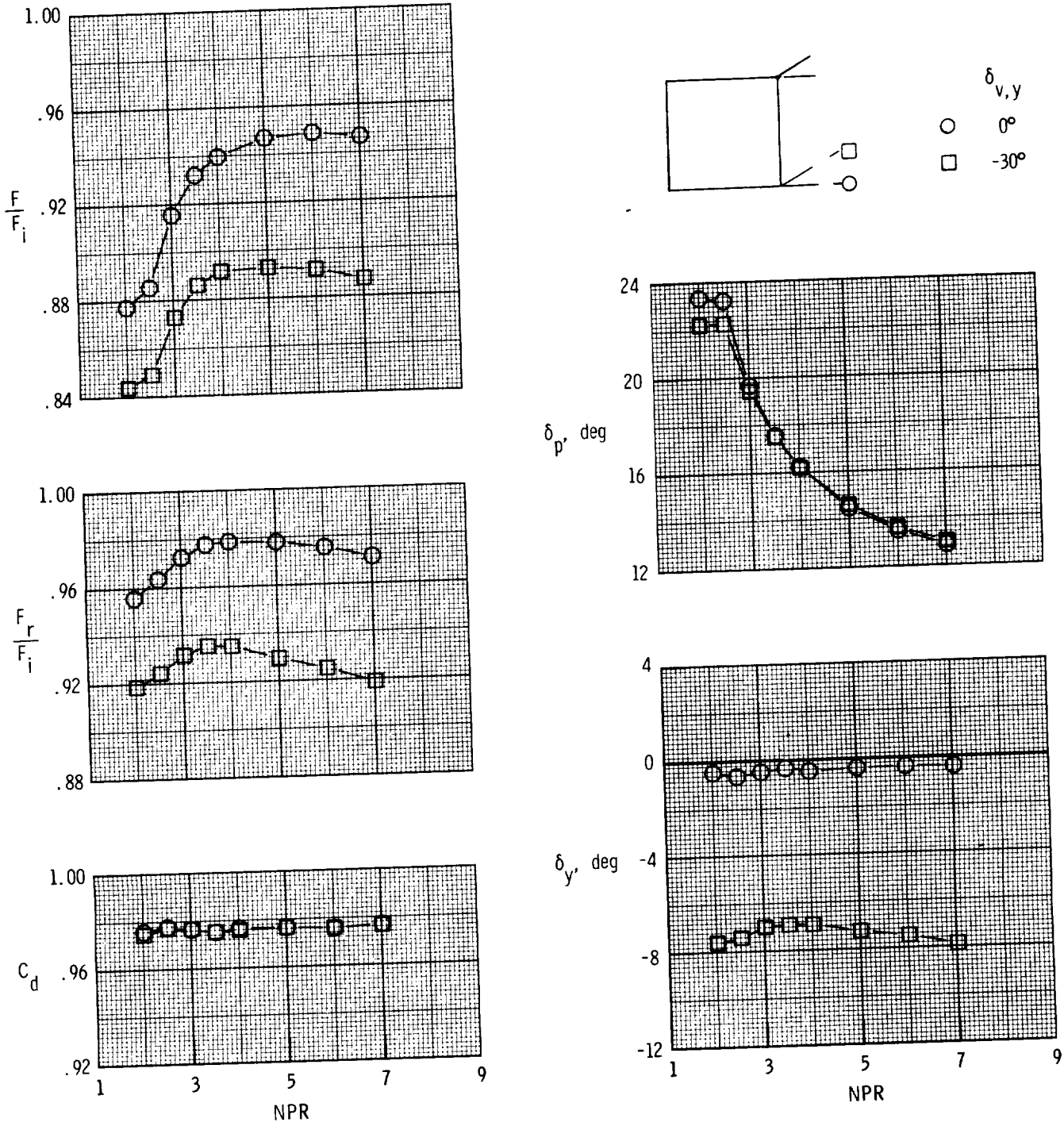

(b) $l_y/l_s = 0.67$.

Figure 14. Continued.

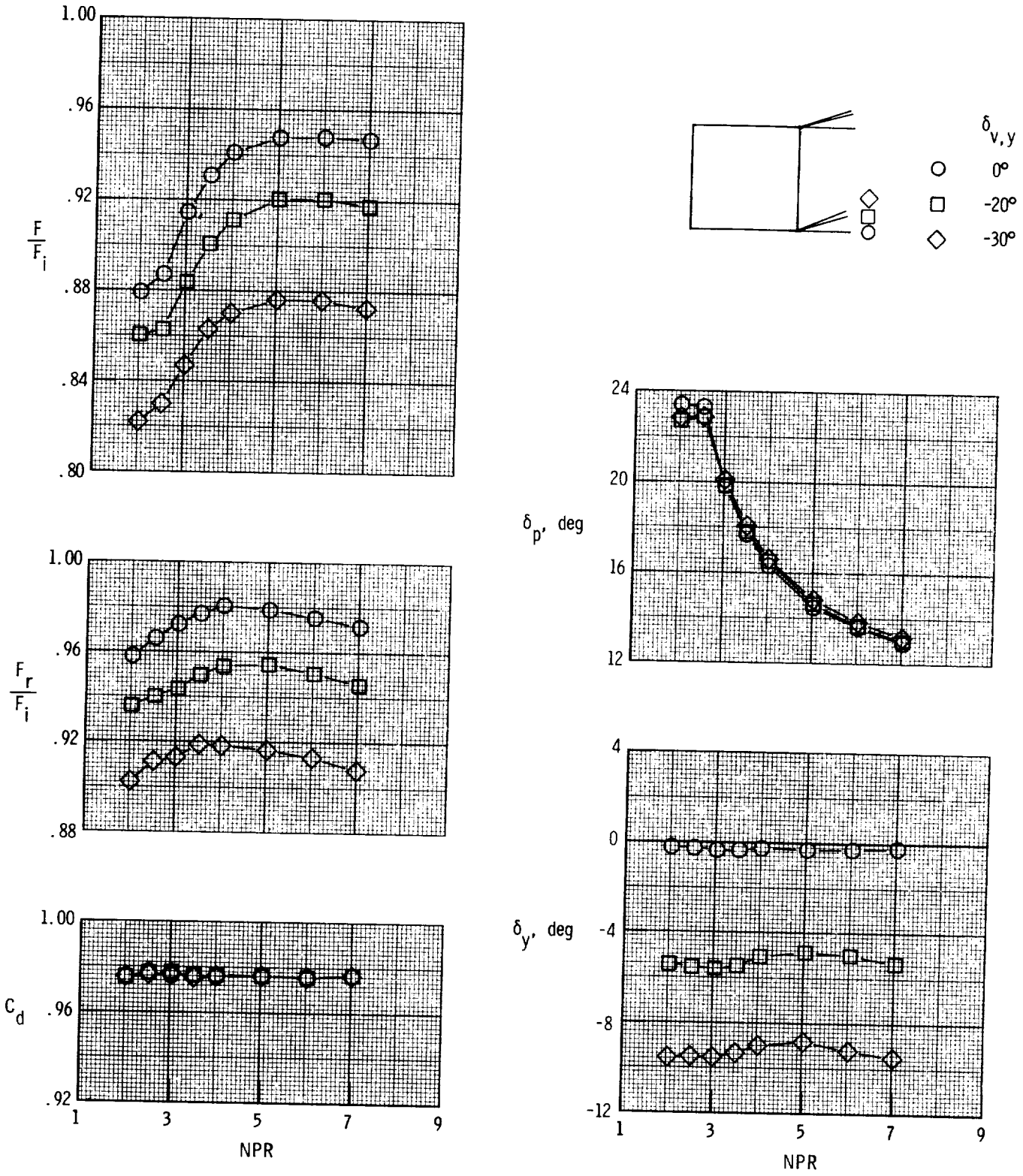

(c) $l_y/l_s = 1.00$.

Figure 14. Concluded.

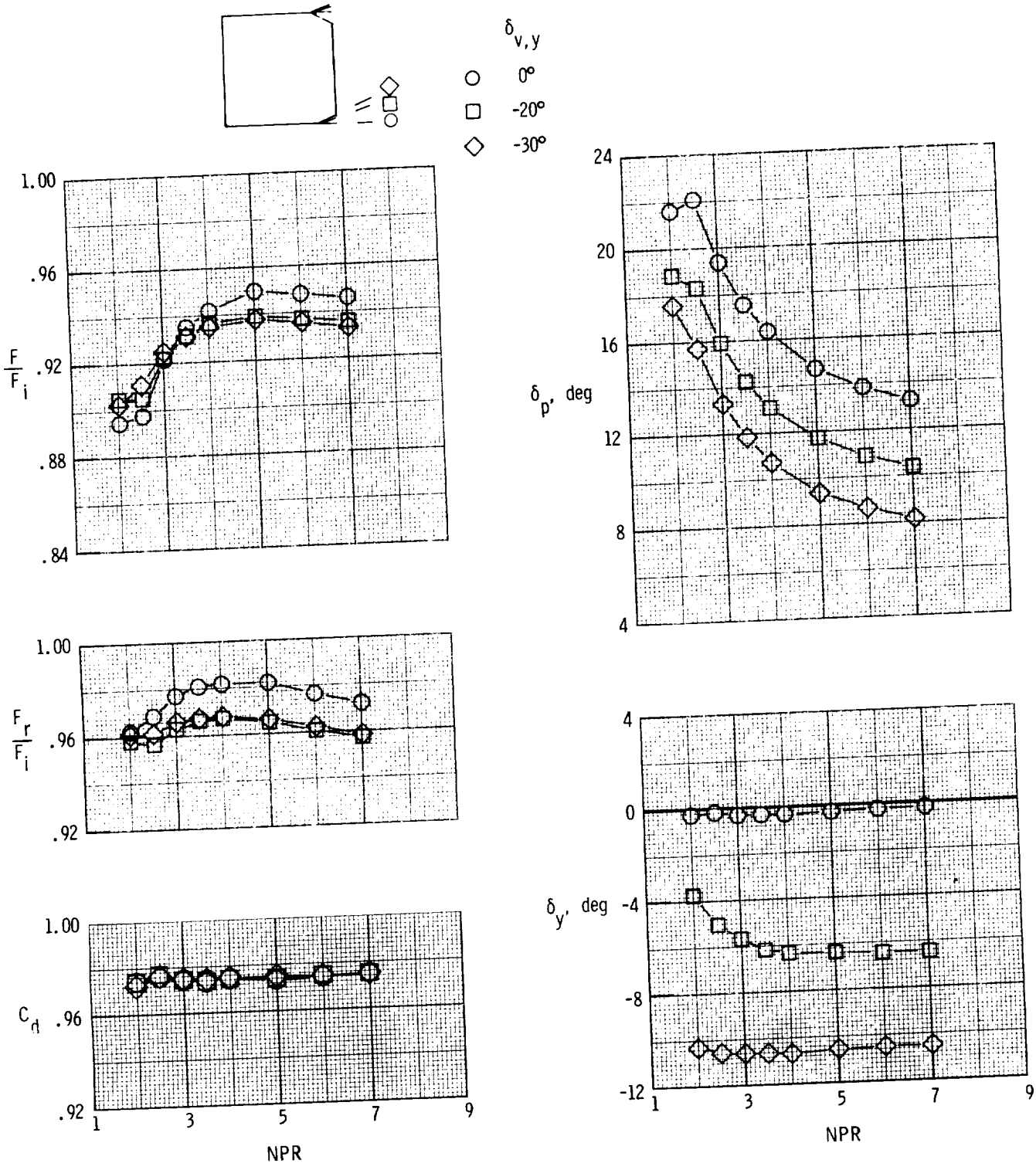

(a) $l_y/l_s = 0.33$.

Figure 15. Effect of yaw-flap deflection on internal performance characteristics of dry power nozzle for $\delta_{v,p} = 19.53°$ and $(x_s - x_t)/l_s = 0.67$.

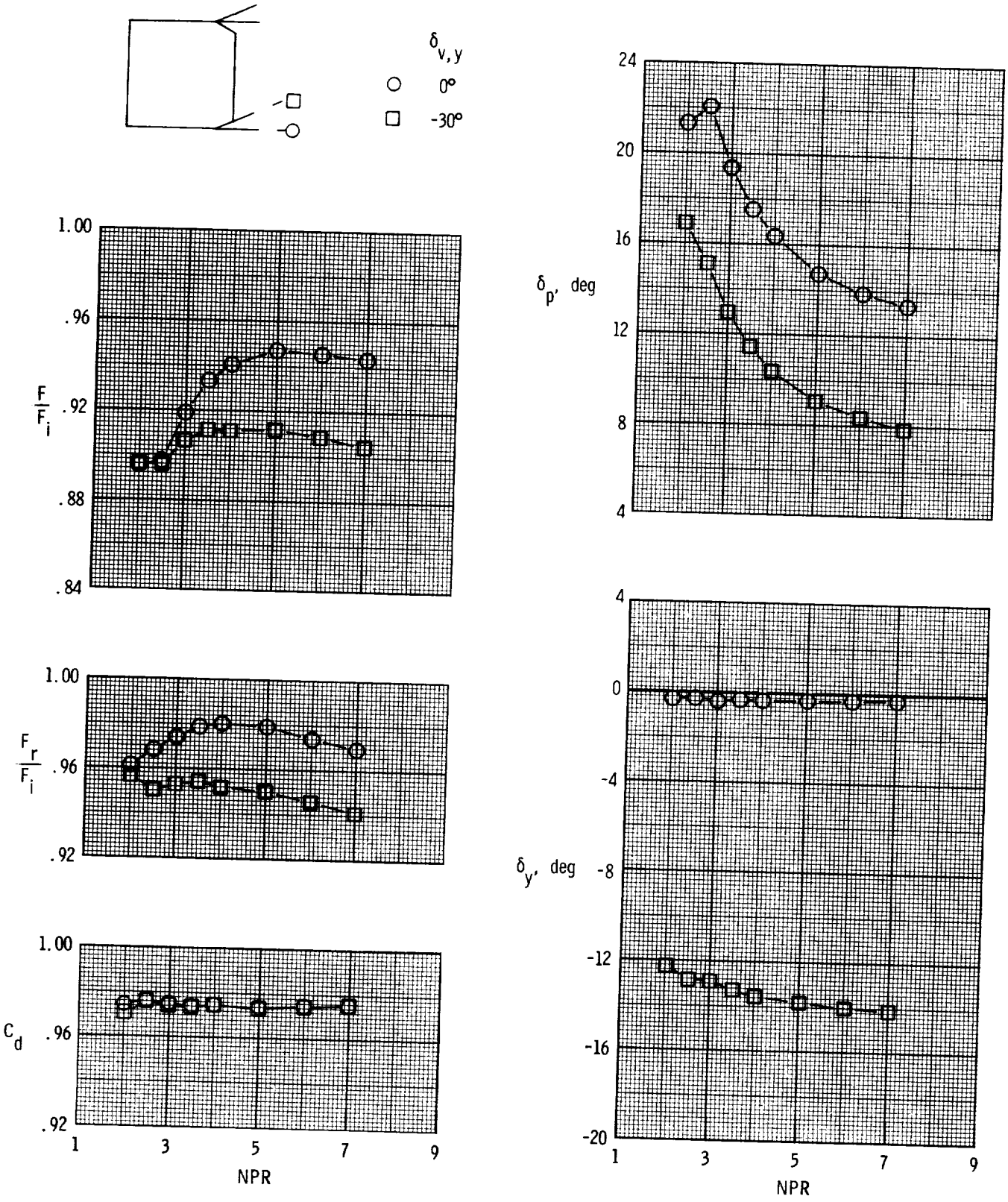

(b) $l_y/l_s = 0.67$.

Figure 15. Continued.

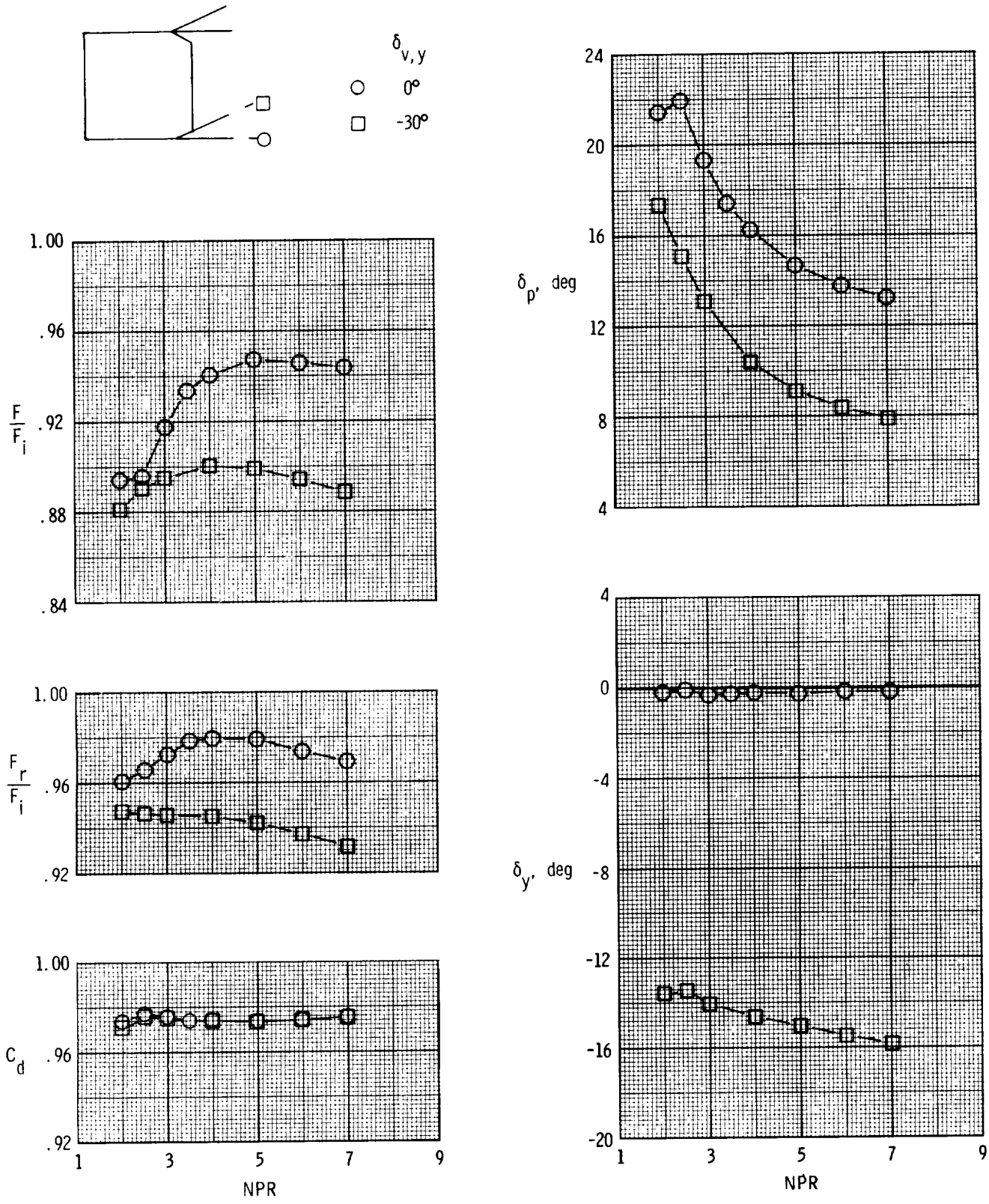

(c) $l_y/l_s = 1.00$.

Figure 15. Concluded.

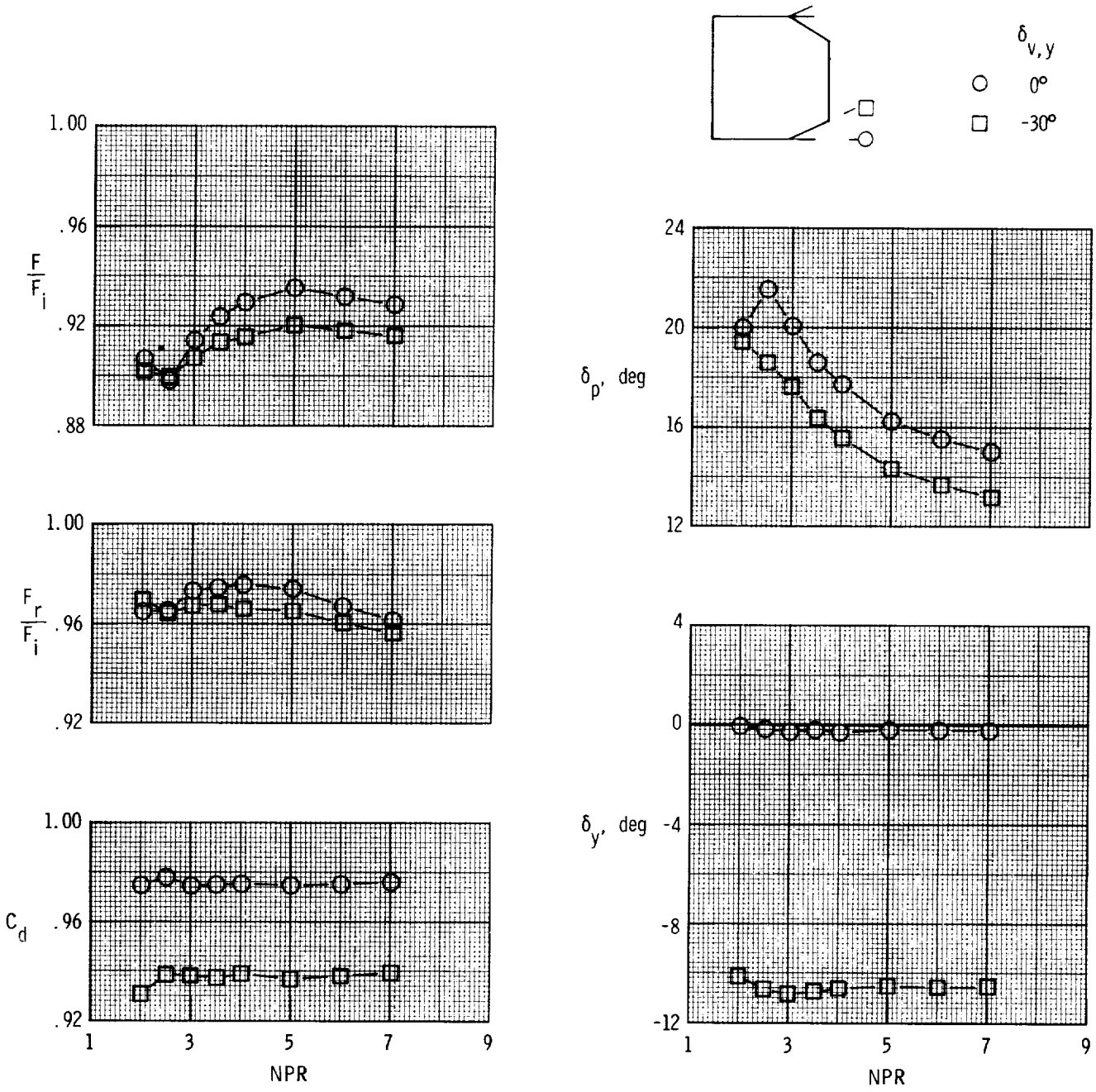

(a) $l_y/l_s = 0.33$.

Figure 16. Effect of yaw-flap deflection on internal performance characteristics of dry power nozzle for $\delta_{v,p} = 19.53°$ and $(x_s - x_t)/l_s = 0.33$.

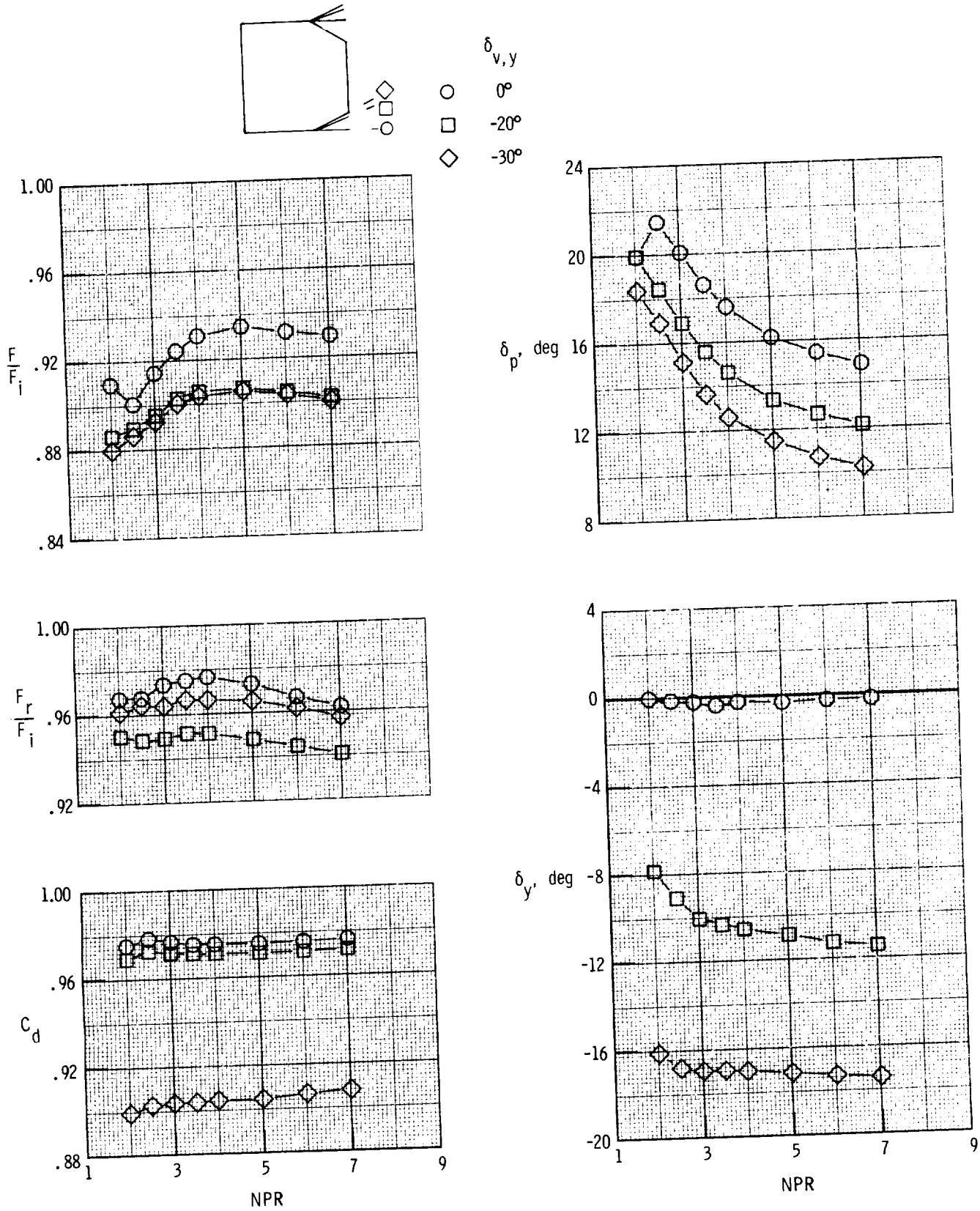

(b) $l_y/l_s = 0.67$.

Figure 16. Continued.

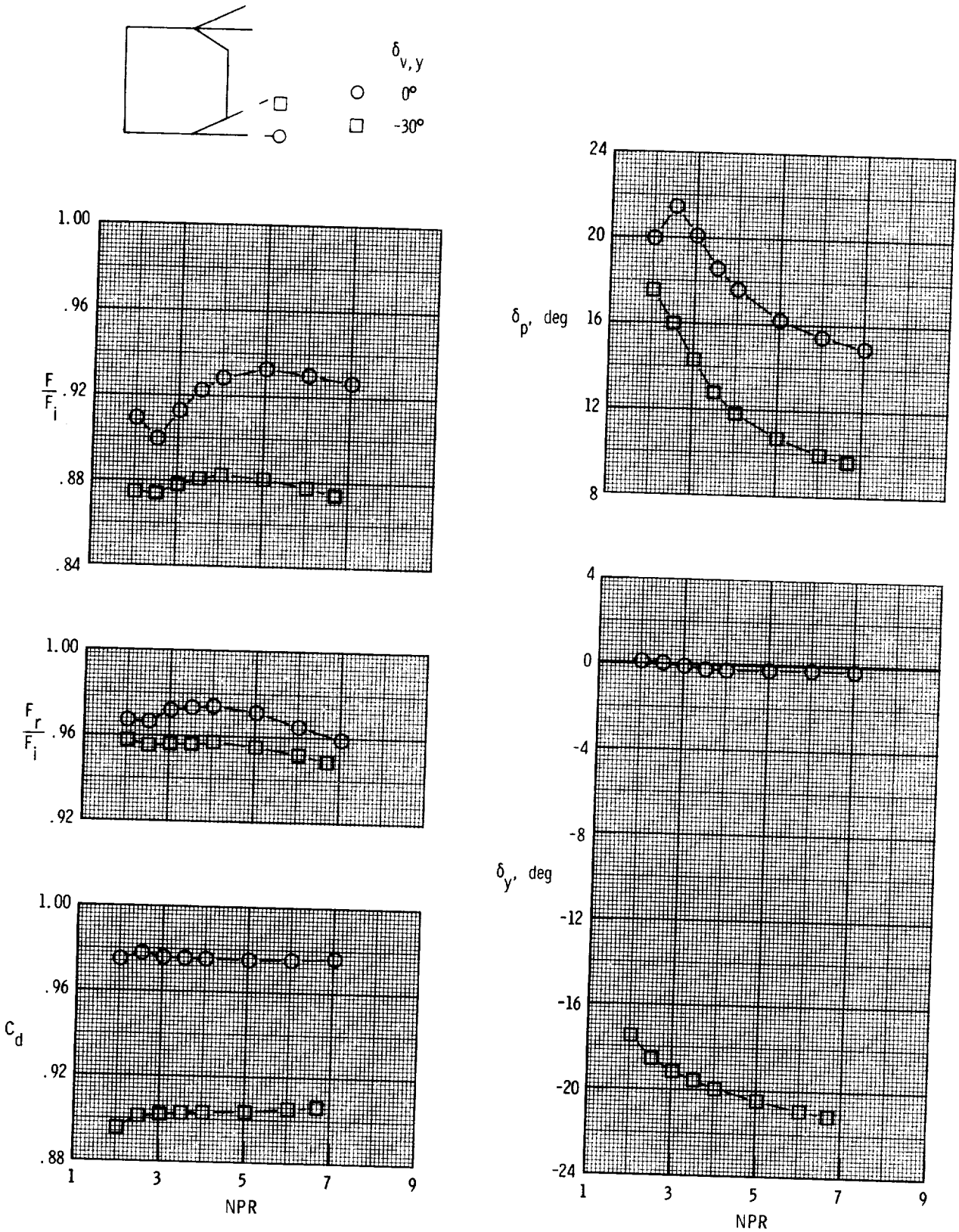

(c) $l_y/l_s = 1.00$.

Figure 16. Concluded.

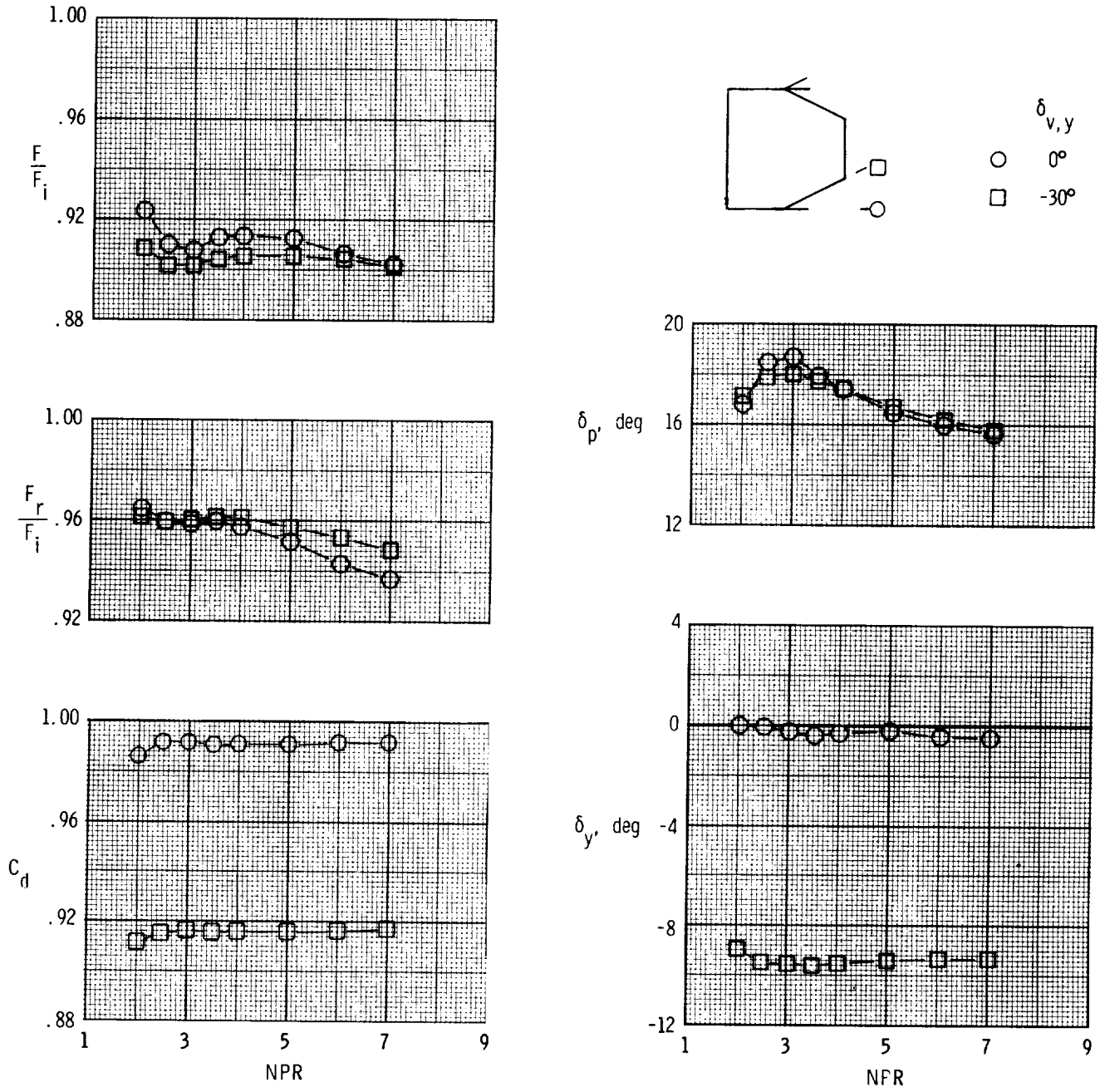

(a) $l_y/l_s = 0.33$.

Figure 17. Effect of yaw-flap deflection on internal performance characteristics of dry power nozzle for $\delta_{v,p} = 19.53°$ and $(x_s - x_t)/l_s = 0$.

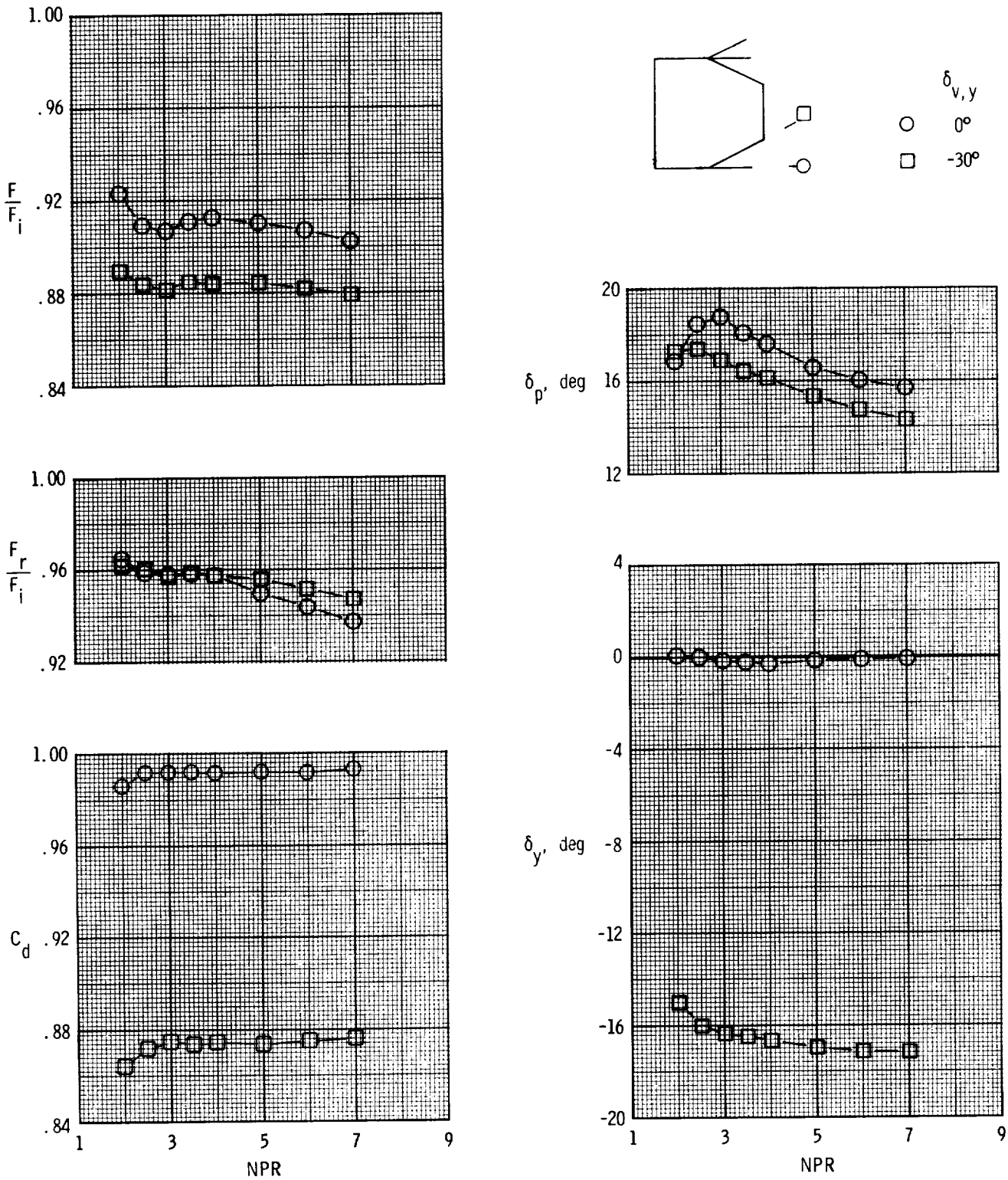

(b) $l_y/l_s = 0.67$.

Figure 17. Continued.

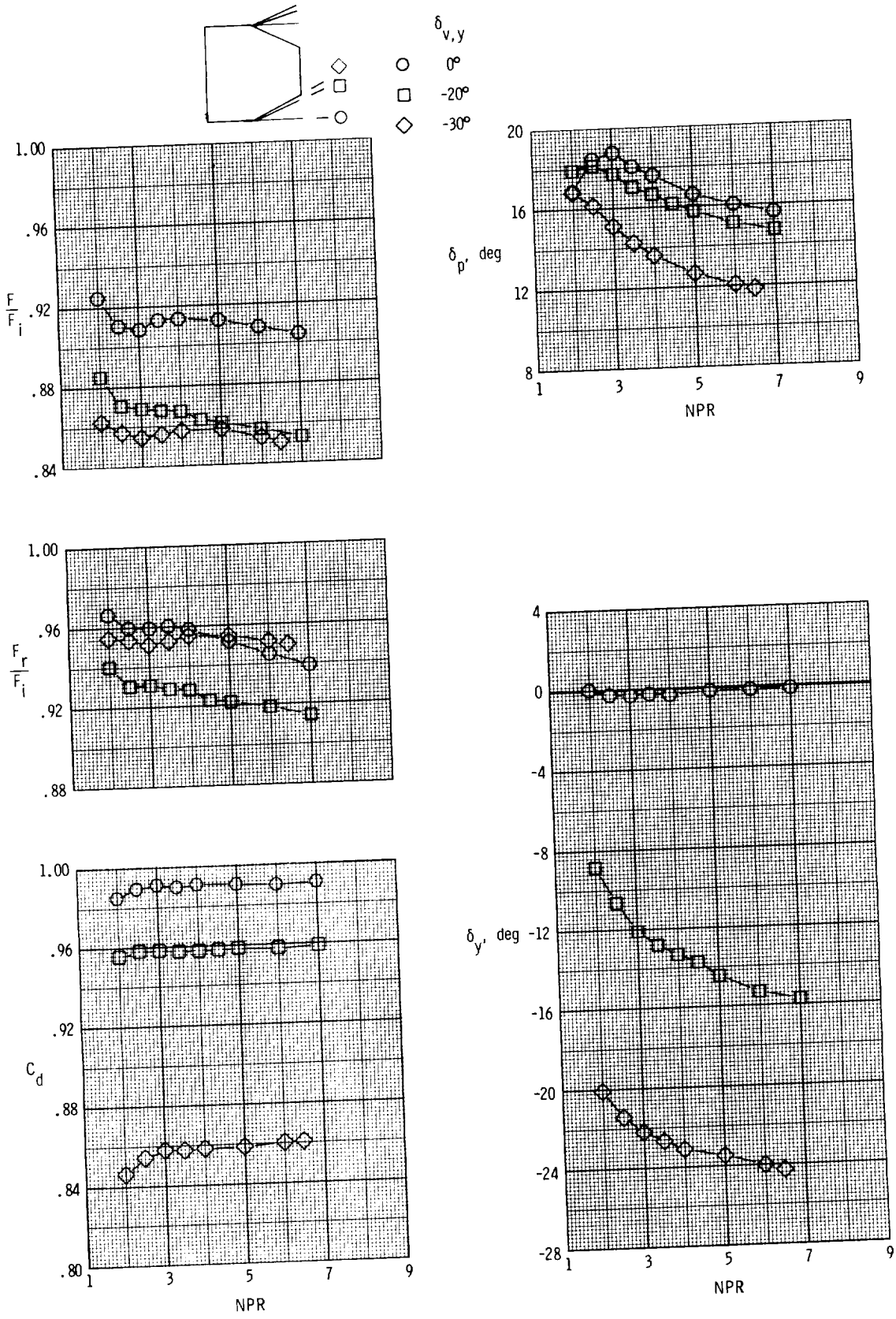

(c) $l_y/l_s = 1.00$.

Figure 17. Concluded.

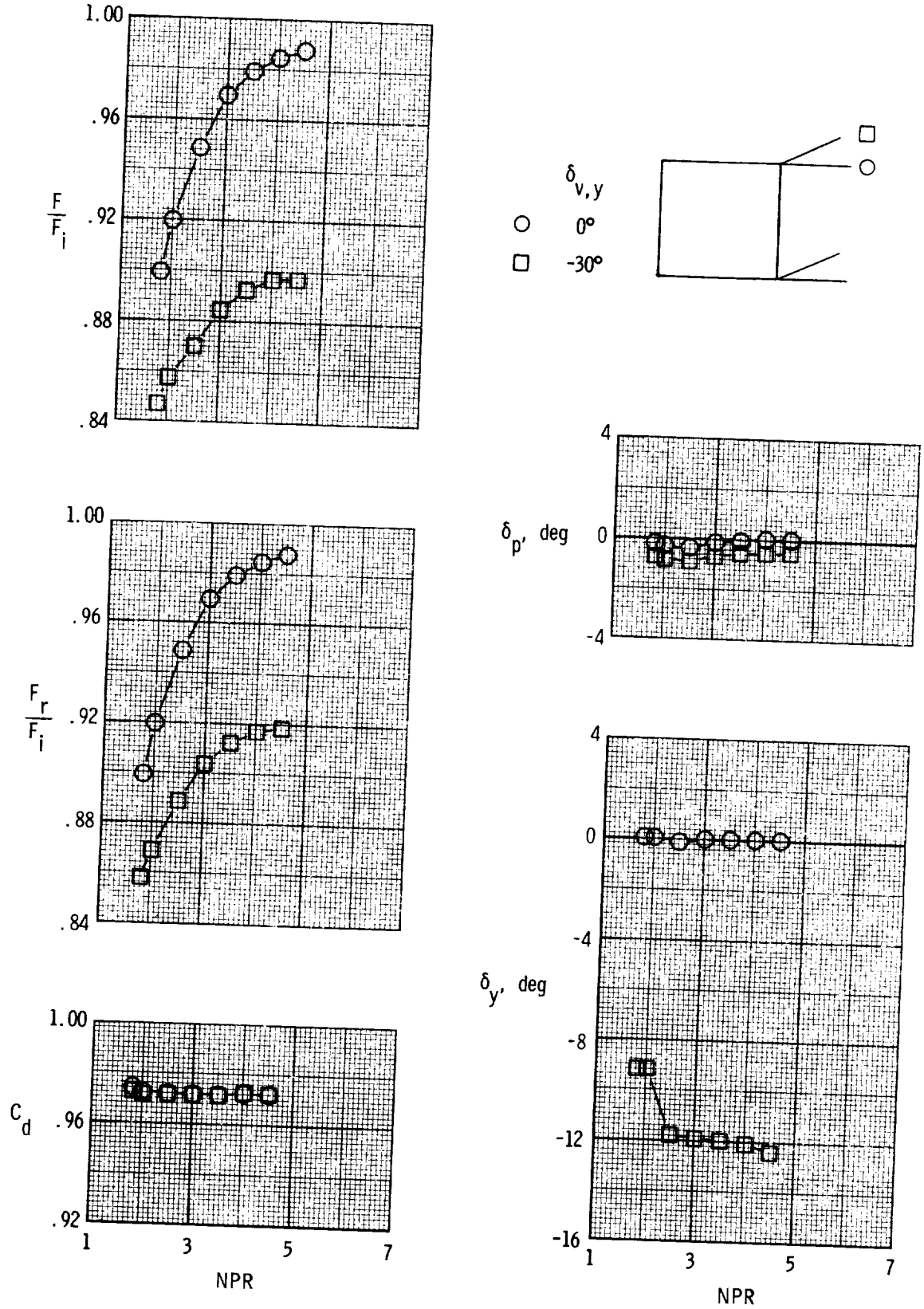

Figure 18. Effect of yaw-flap deflection on internal performance characteristics of A/B power nozzle for $\delta_{v,p} = 0°$, $(x_s - x_t)/l_s = 1.00$, and $l_y/l_s = 1.03$.

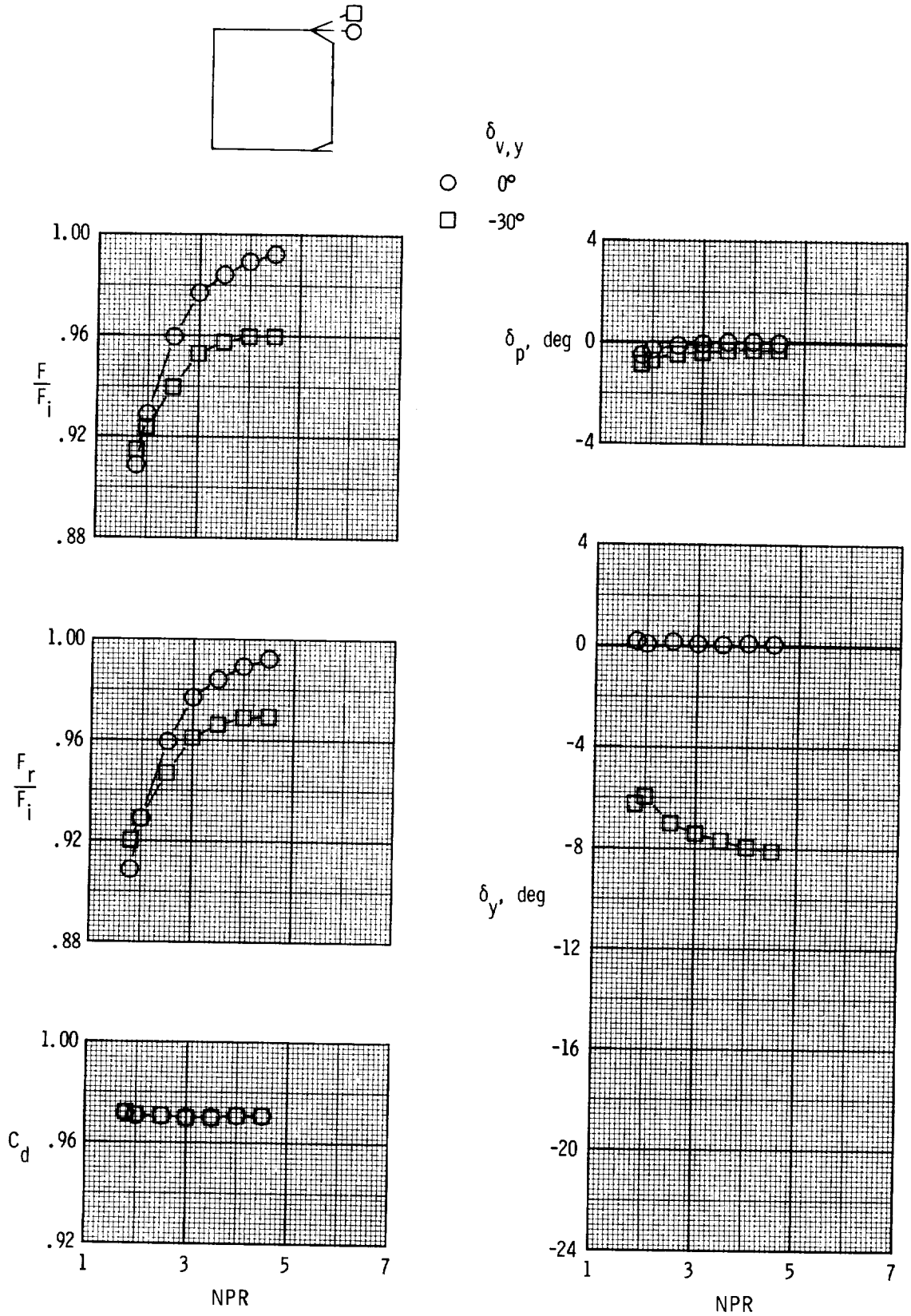

Figure 19. Effect of yaw-flap deflection on internal performance characteristics of A/B power nozzle for $\delta_{v,p} = 0°$, $(x_s - x_t)/l_s = 0.66$, and $l_y/l_s = 0.34$.

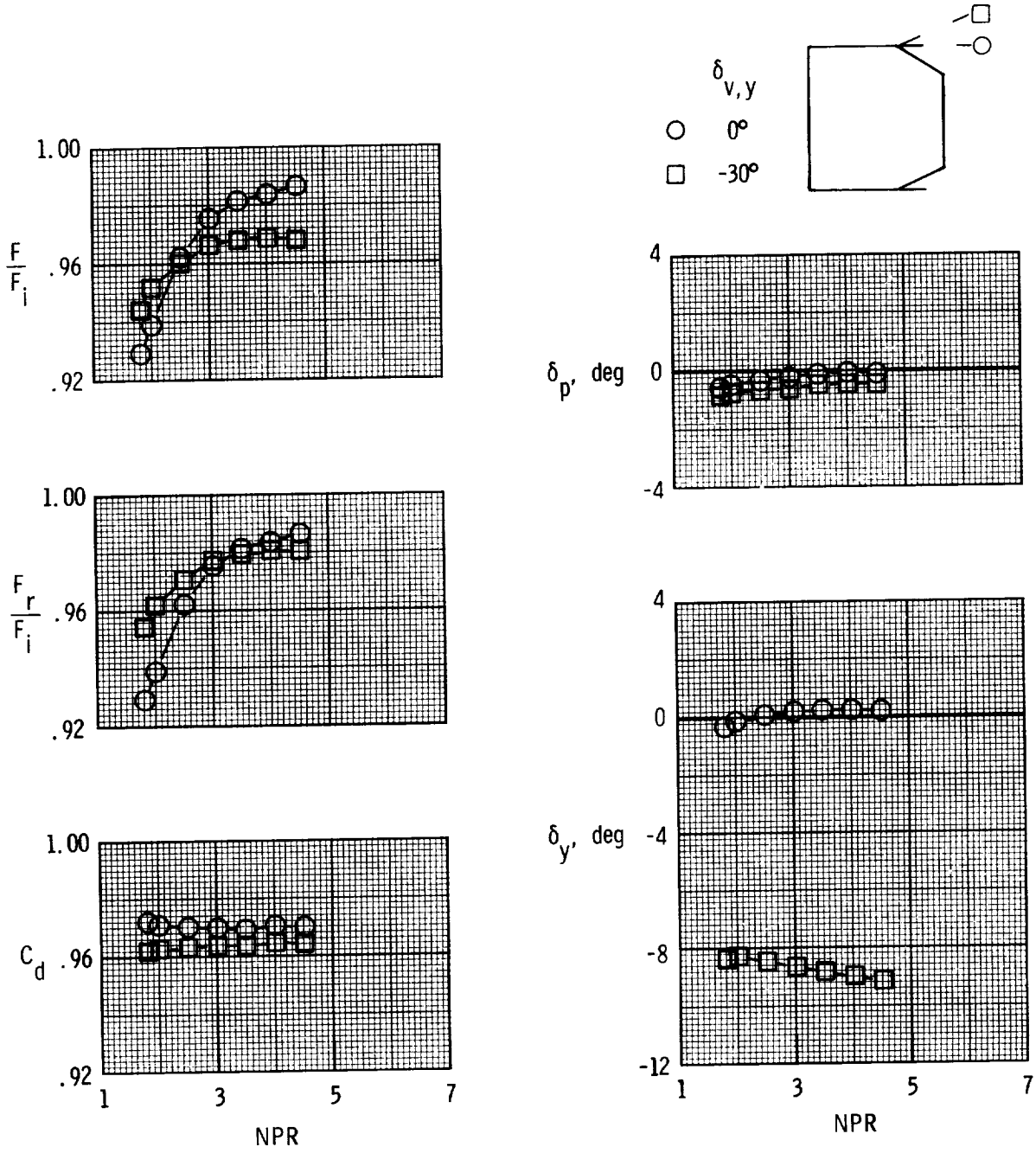

(a) $l_y/l_s = 0.34$.

Figure 20. Effect of yaw-flap deflection on internal performance characteristics of A/B power nozzle for $\delta_{v,p} = 0°$ and $(x_s - x_t)/l_s = 0.31$.

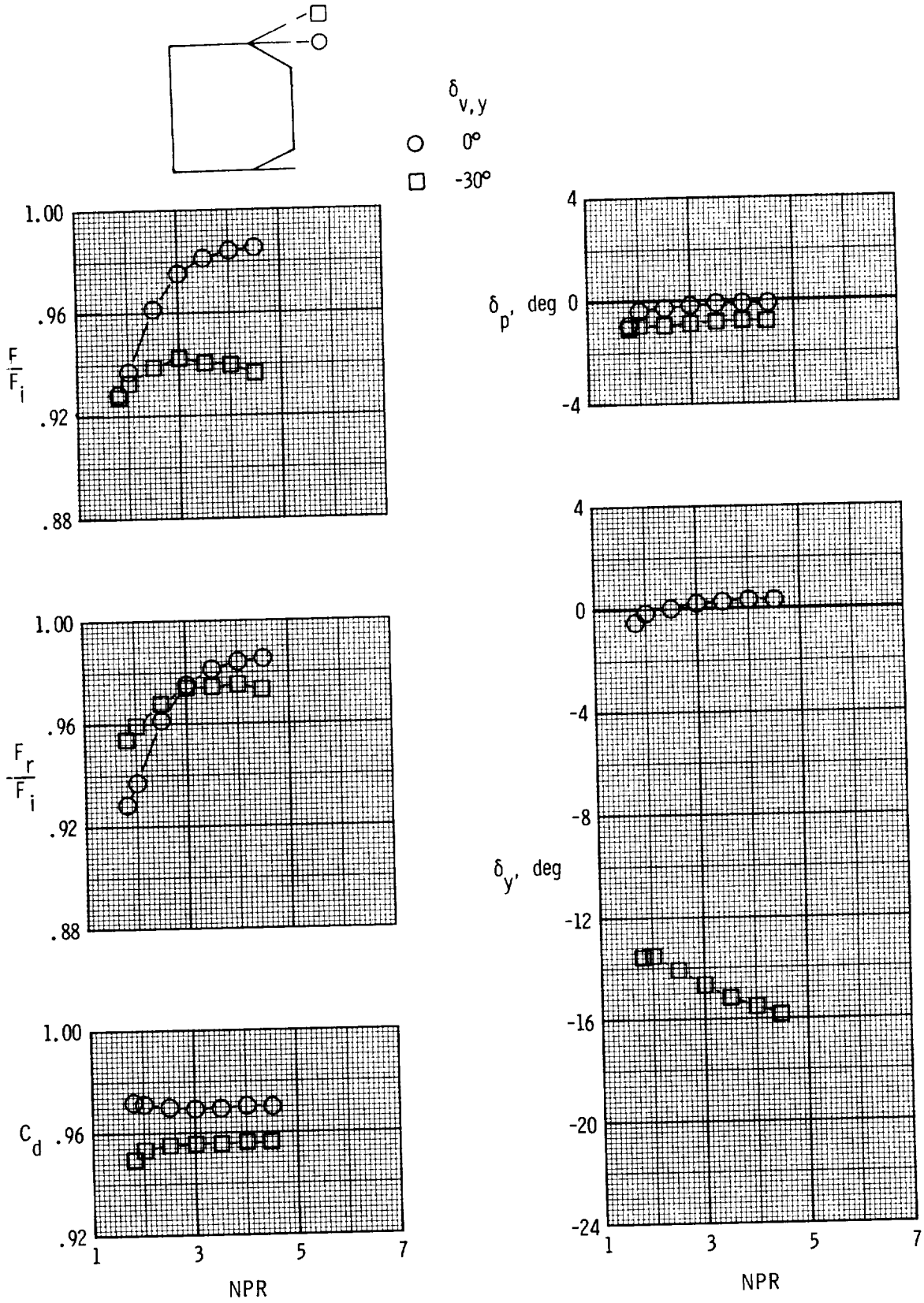

(b) $l_y/l_s = 0.69$.

Figure 20. Continued.

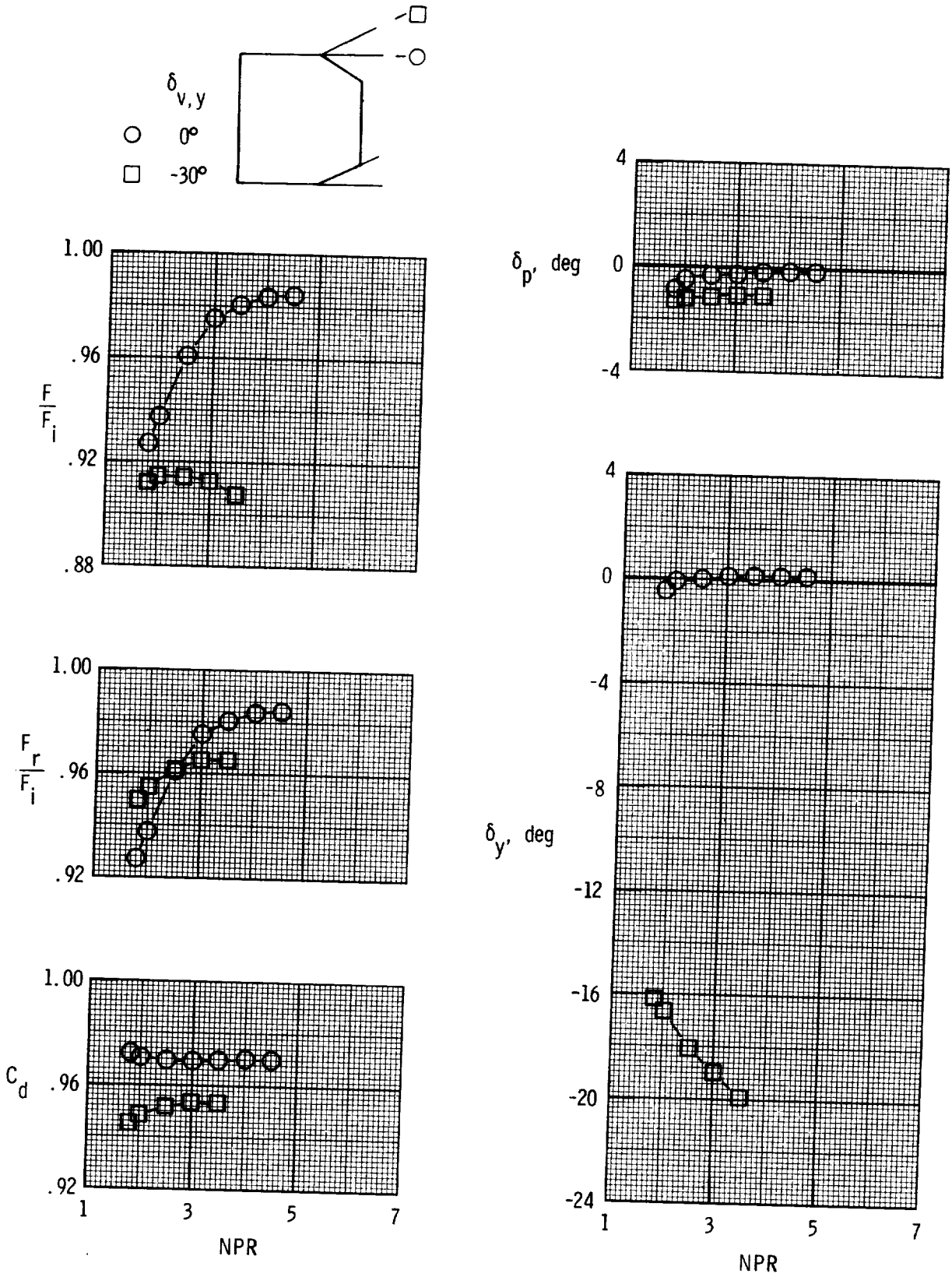

(c) $l_y/l_s = 1.03$.

Figure 20. Concluded.

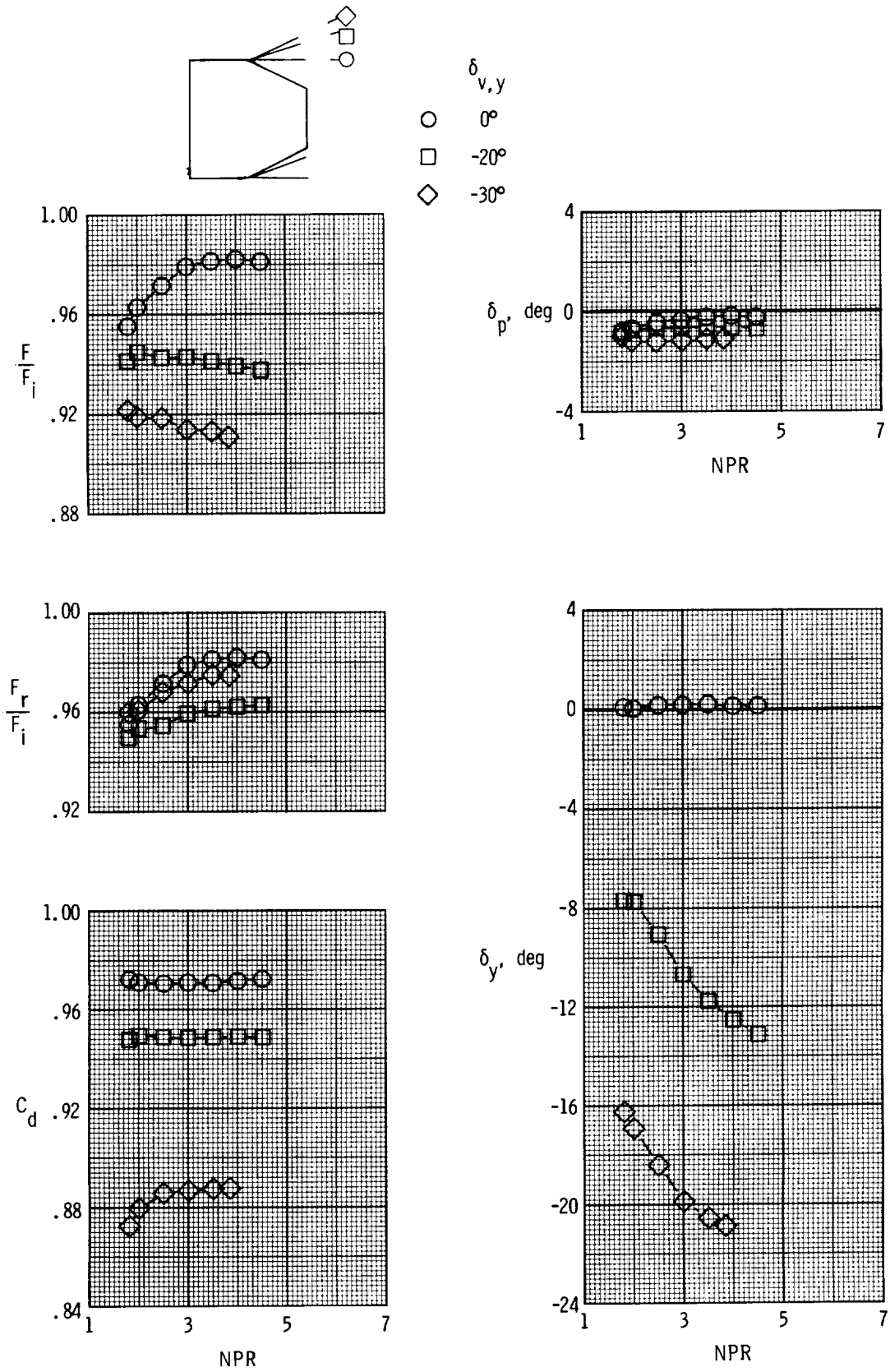

Figure 21. Effect of yaw-flap deflection on internal performance characteristics of A/B power nozzle for $\delta_{v,p} = 0°$, $(x_s - x_t)/l_s = -0.03$, and $l_y/l_s = 1.03$.

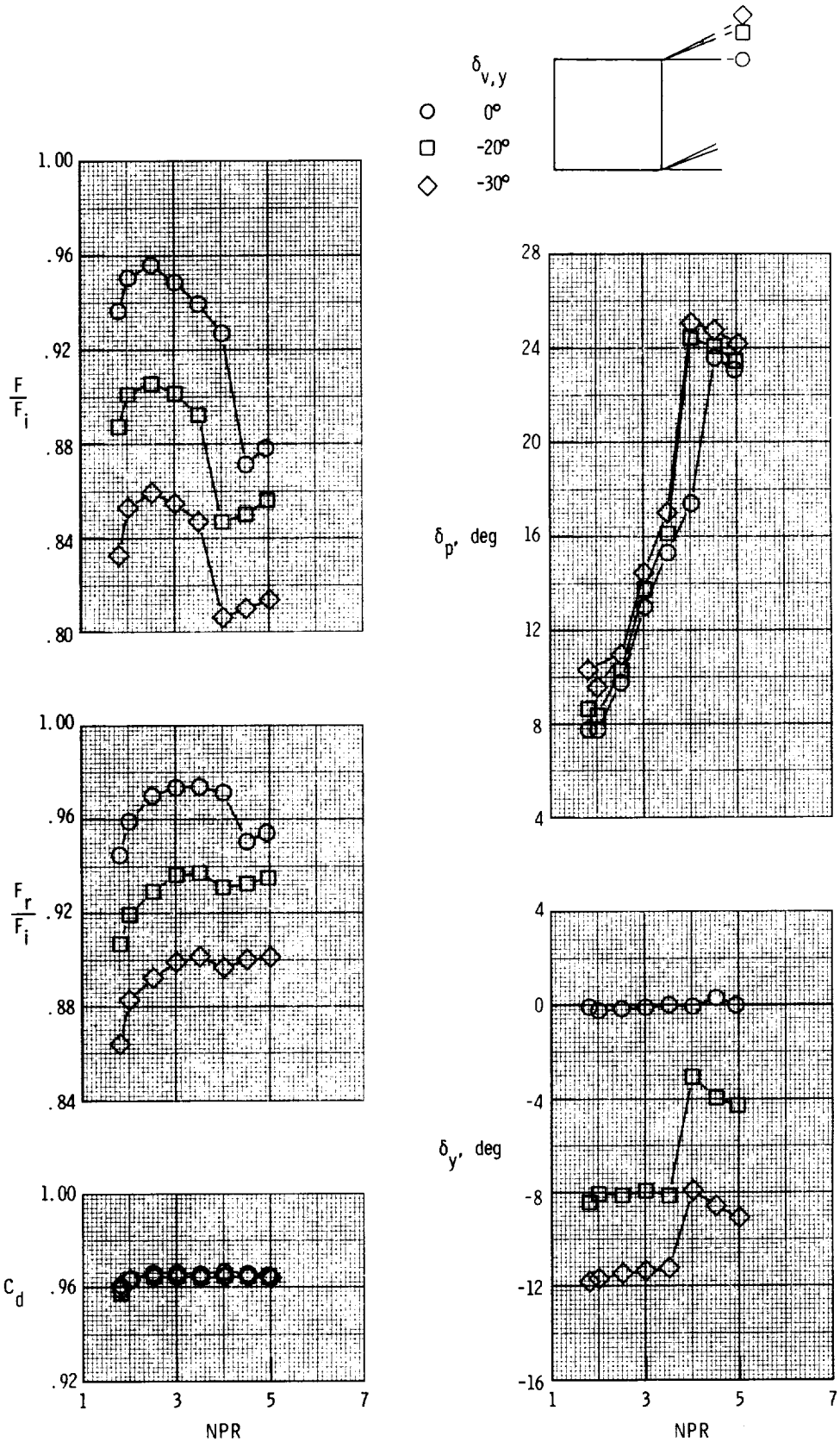

Figure 22. Effect of yaw-flap deflection on internal performance characteristics of A/B power nozzle for $\delta_{v,p} = 20.26°$, $(x_s - x_t)/l_s = 1.00$, and $l_y/l_s = 1.03$.

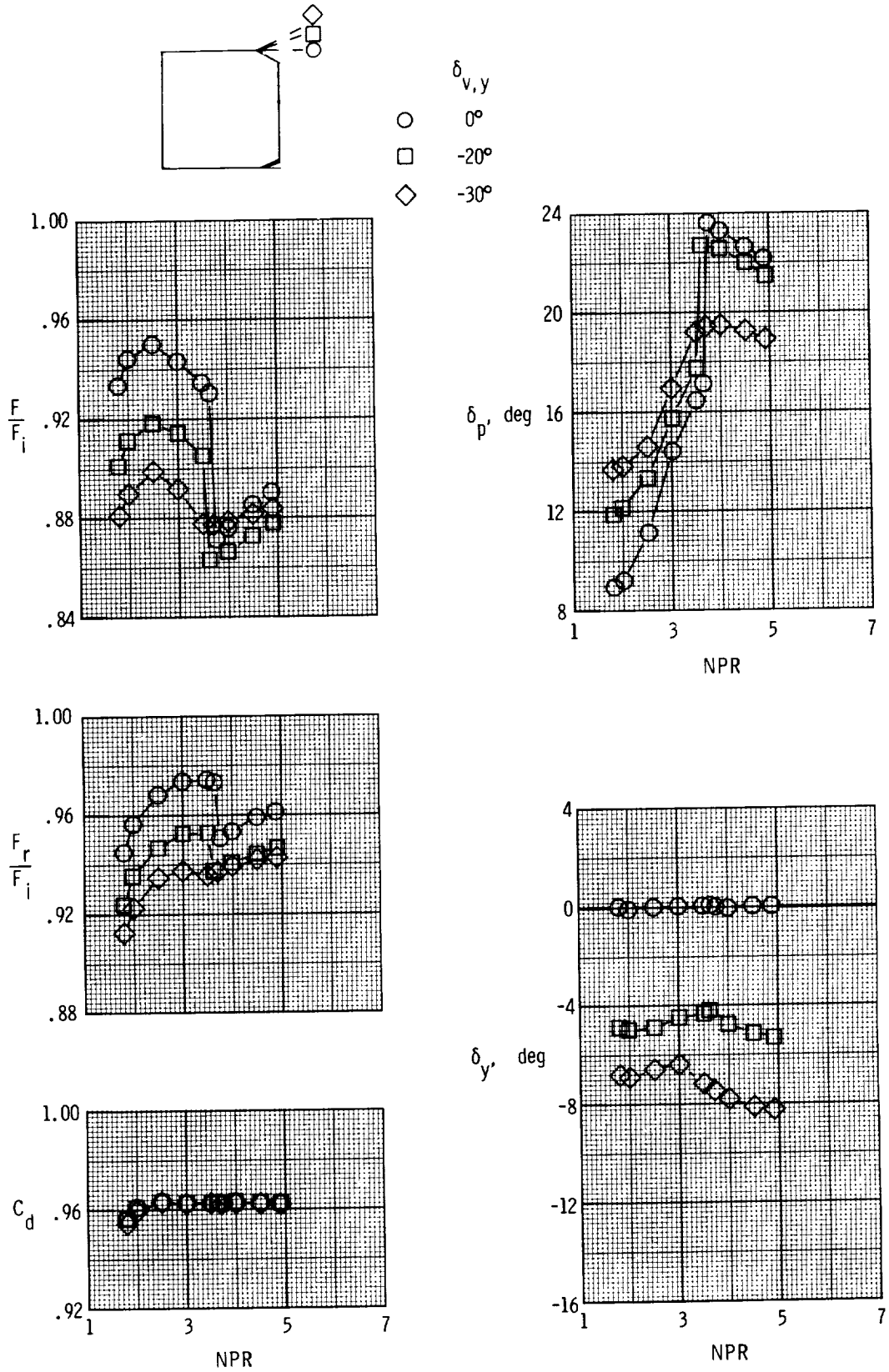

Figure 23. Effect of yaw-flap deflection on internal performance characteristics of A/B power nozzle for $\delta_{v,p} = 20.26°$, $(x_s - x_t)/l_s = 0.66$, and $l_y/l_s = 0.34$.

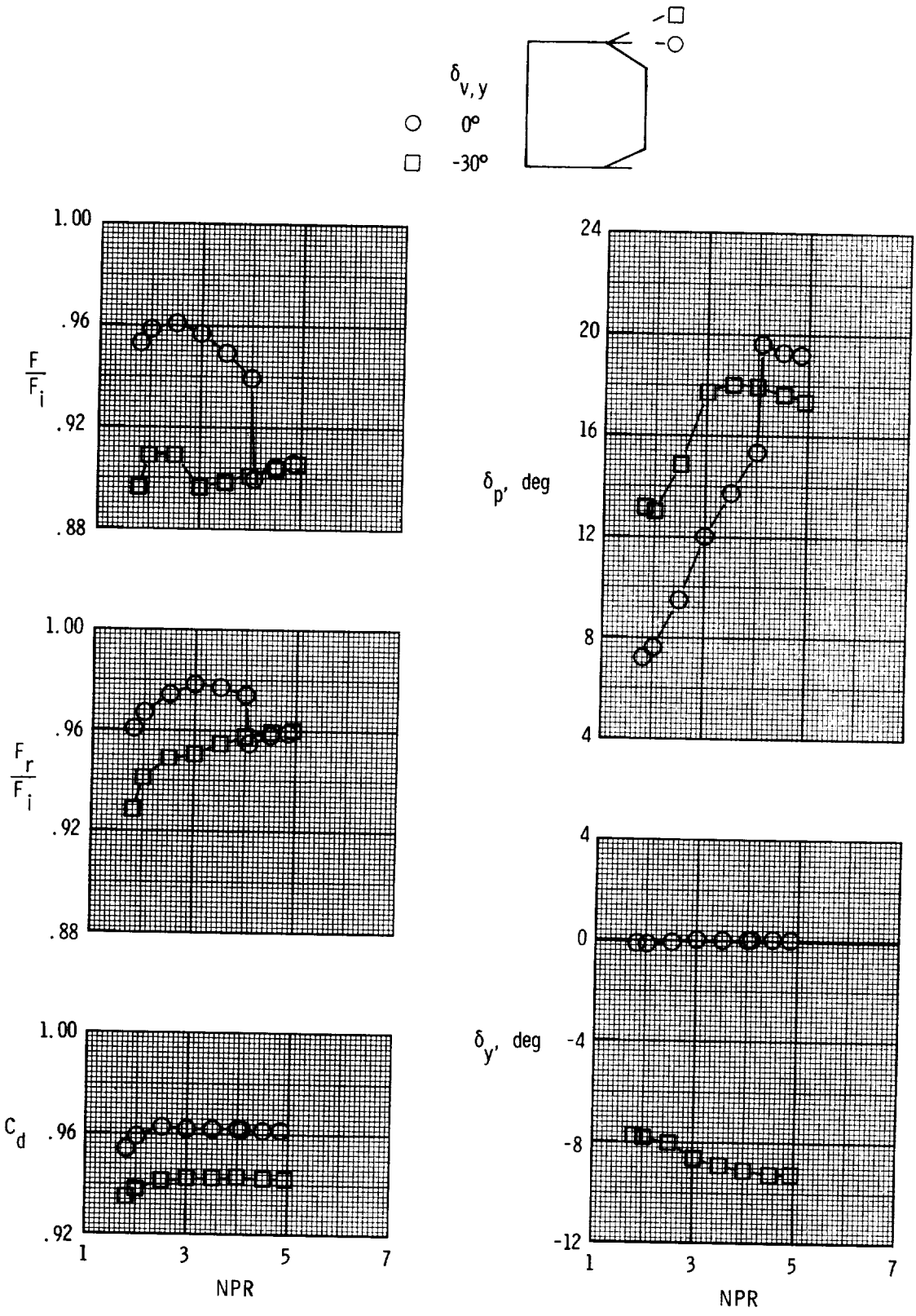

(a) $l_y/l_s = 0.34$.

Figure 24. Effect of yaw-flap deflection on internal performance characteristics of A/B power nozzle for $\delta_{v,p} = 20.26°$ and $(x_s - x_t)/l_s = 0.31$.

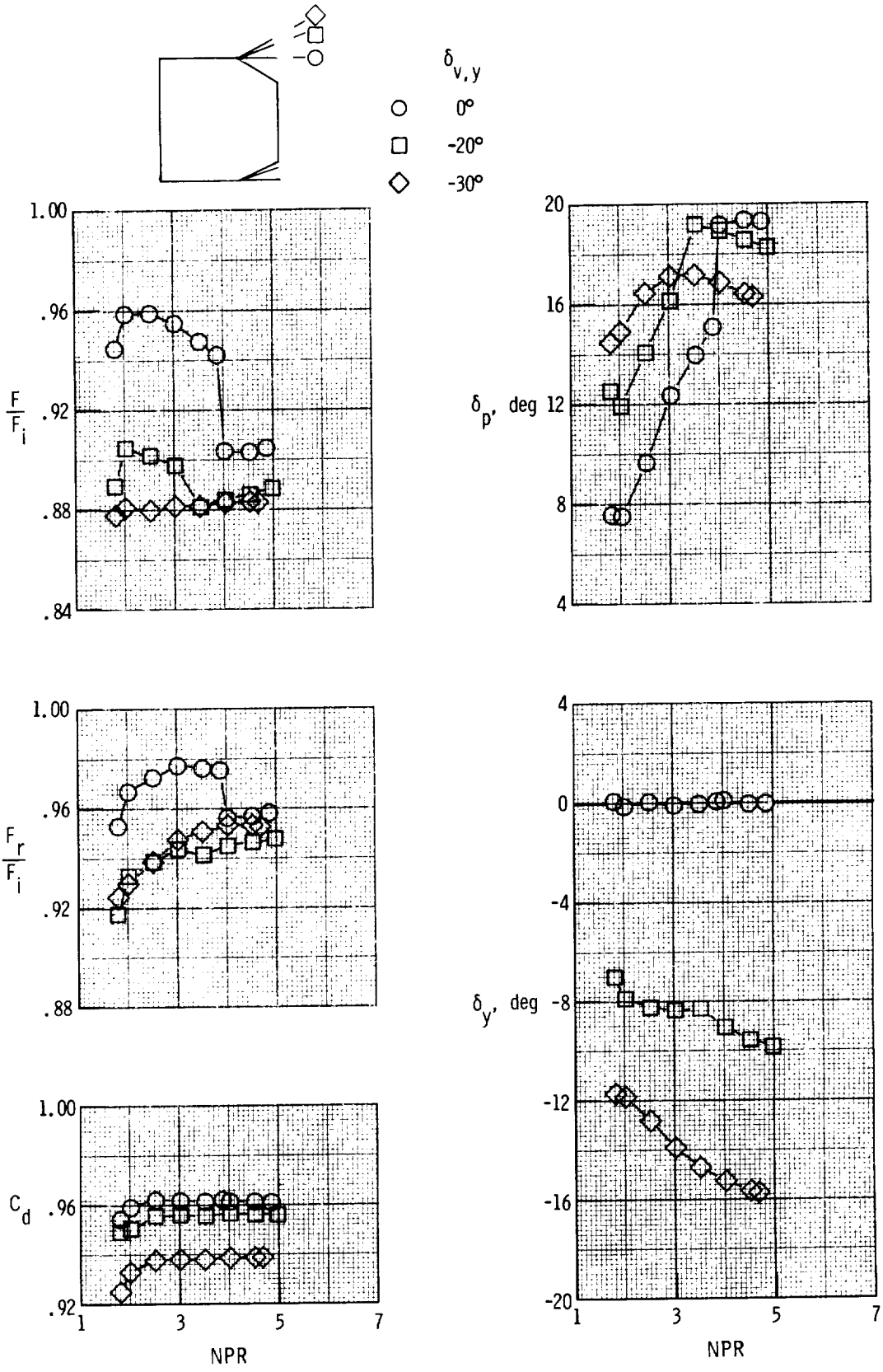

(b) $l_y/l_s = 0.69$.

Figure 24. Continued.

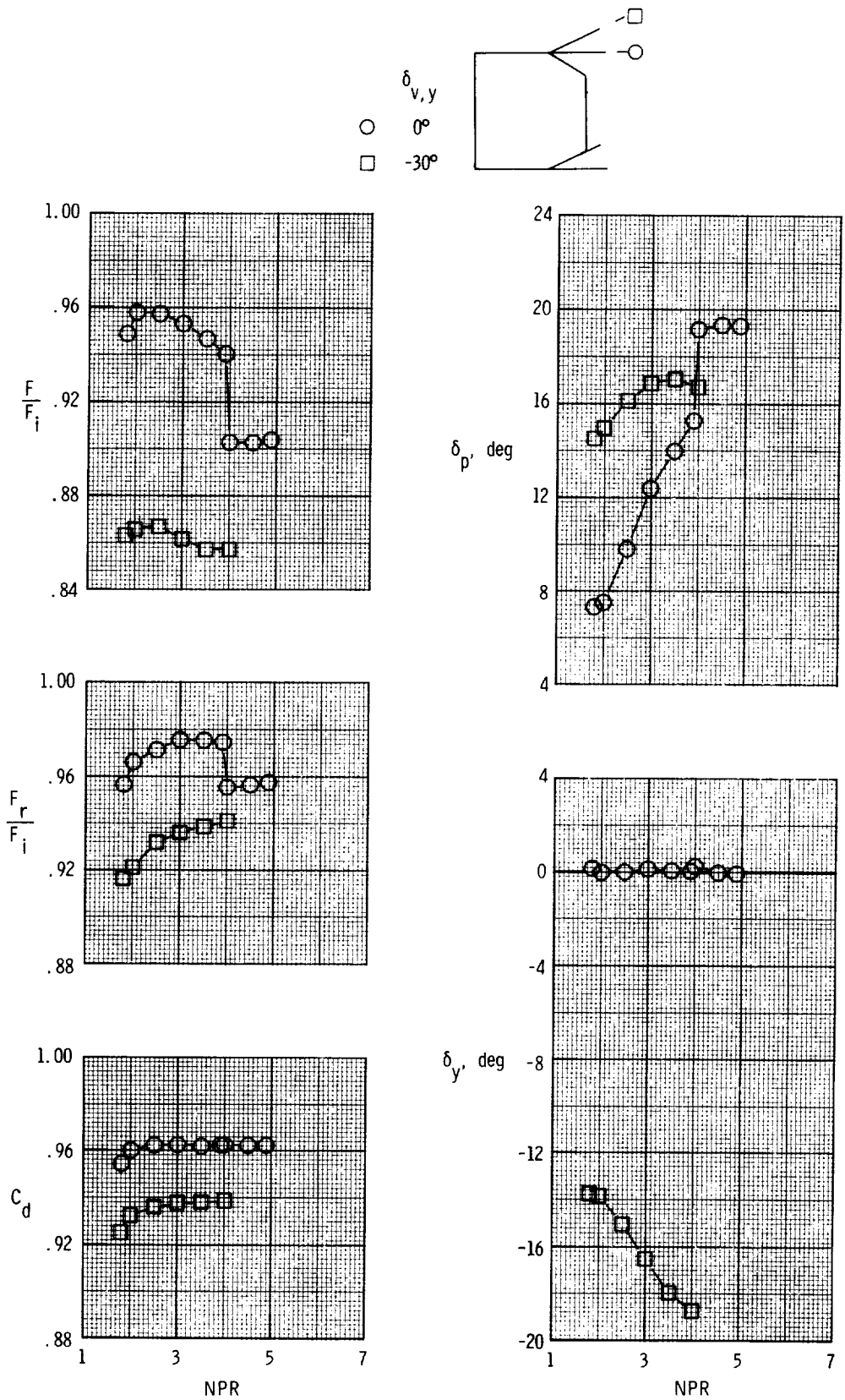

(c) $l_y/l_s = 1.03$.

Figure 24. Concluded.

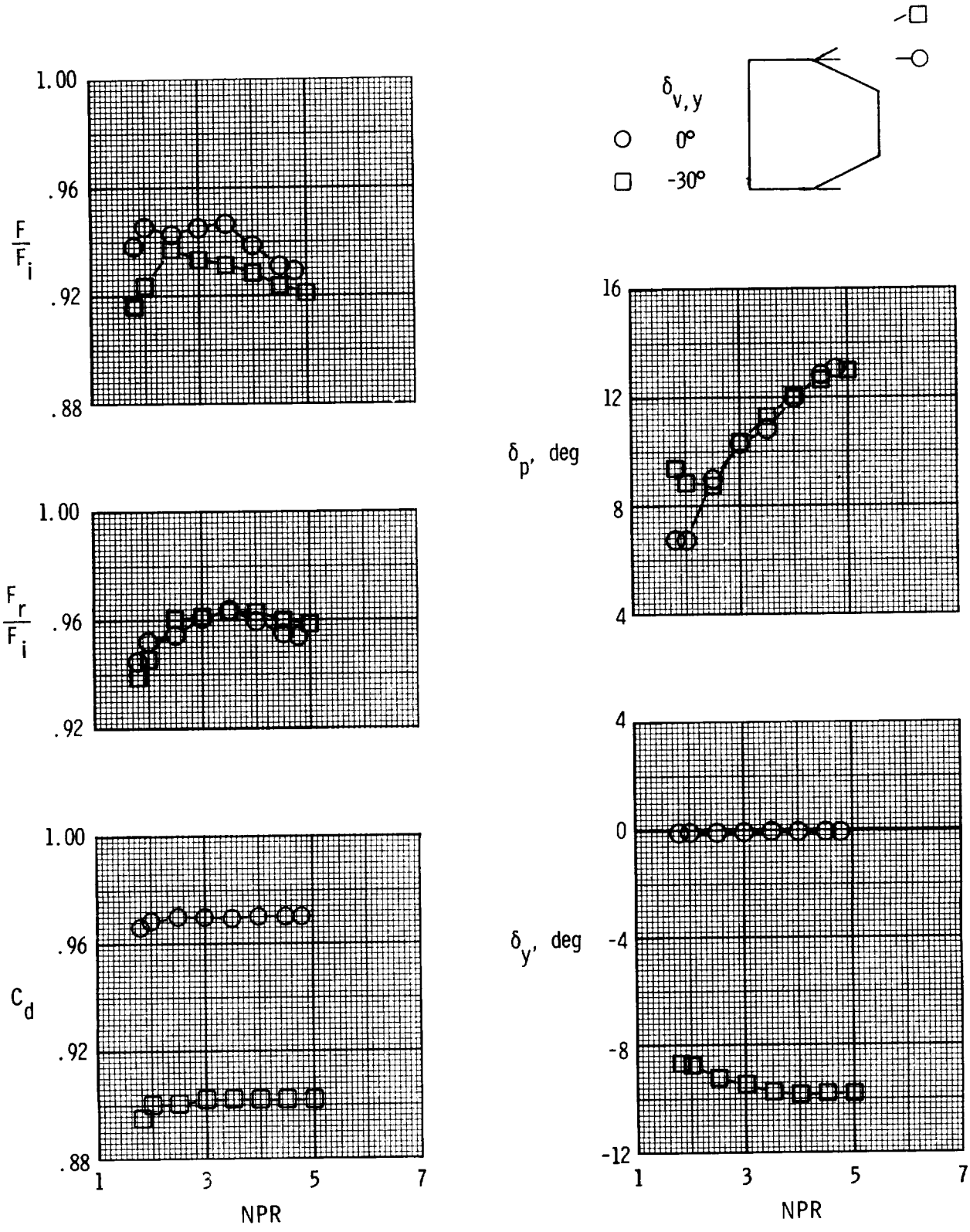

(a) $l_y/l_s = 0.34$.

Figure 25. Effect of yaw-flap deflection on internal performance characteristics of A/B power nozzle for $\delta_{v,p} = 20.26°$ and $(x_s - x_t)/l_s = -0.03$.

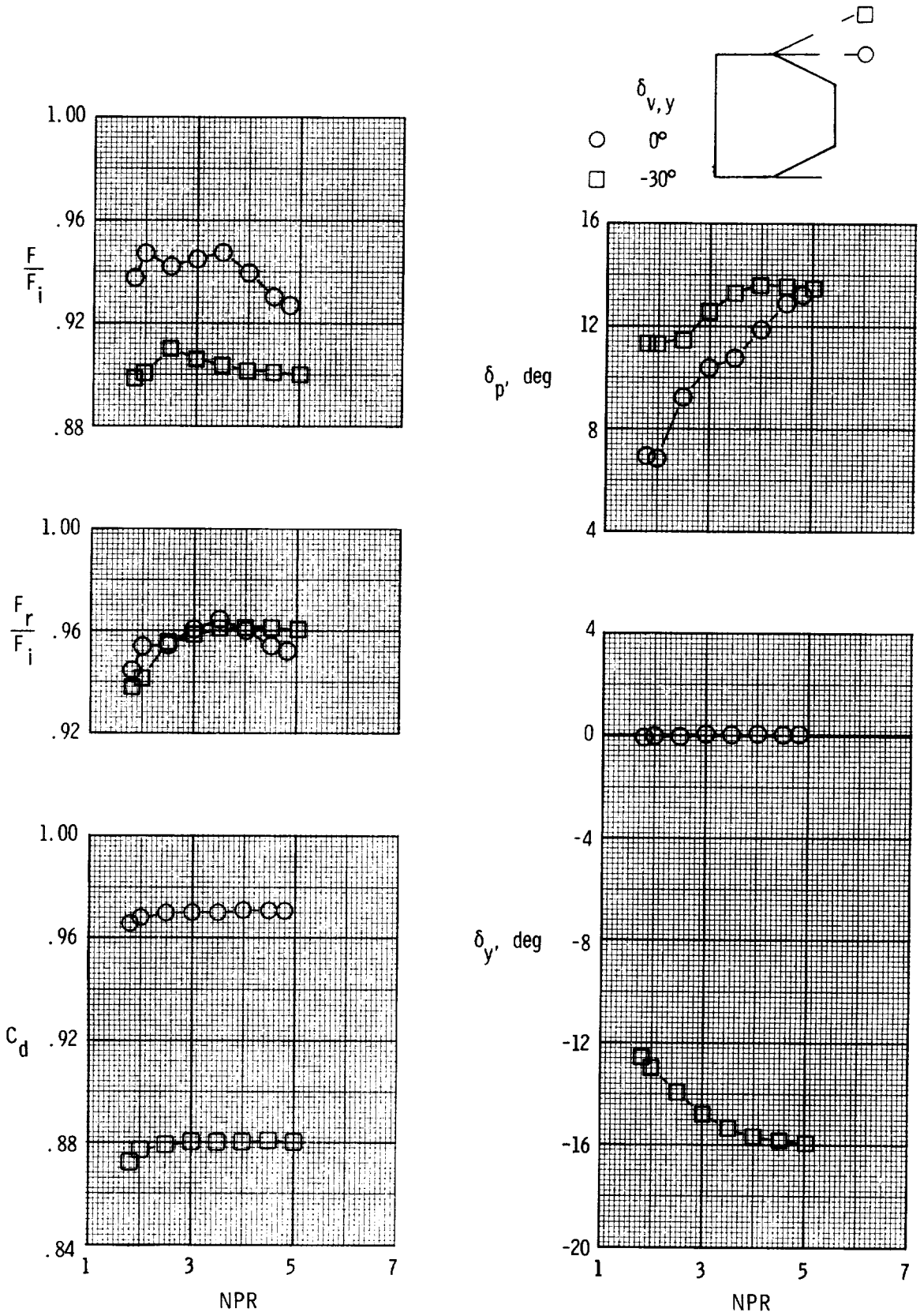

(b) $l_y/l_s = 0.69$.

Figure 25. Continued.

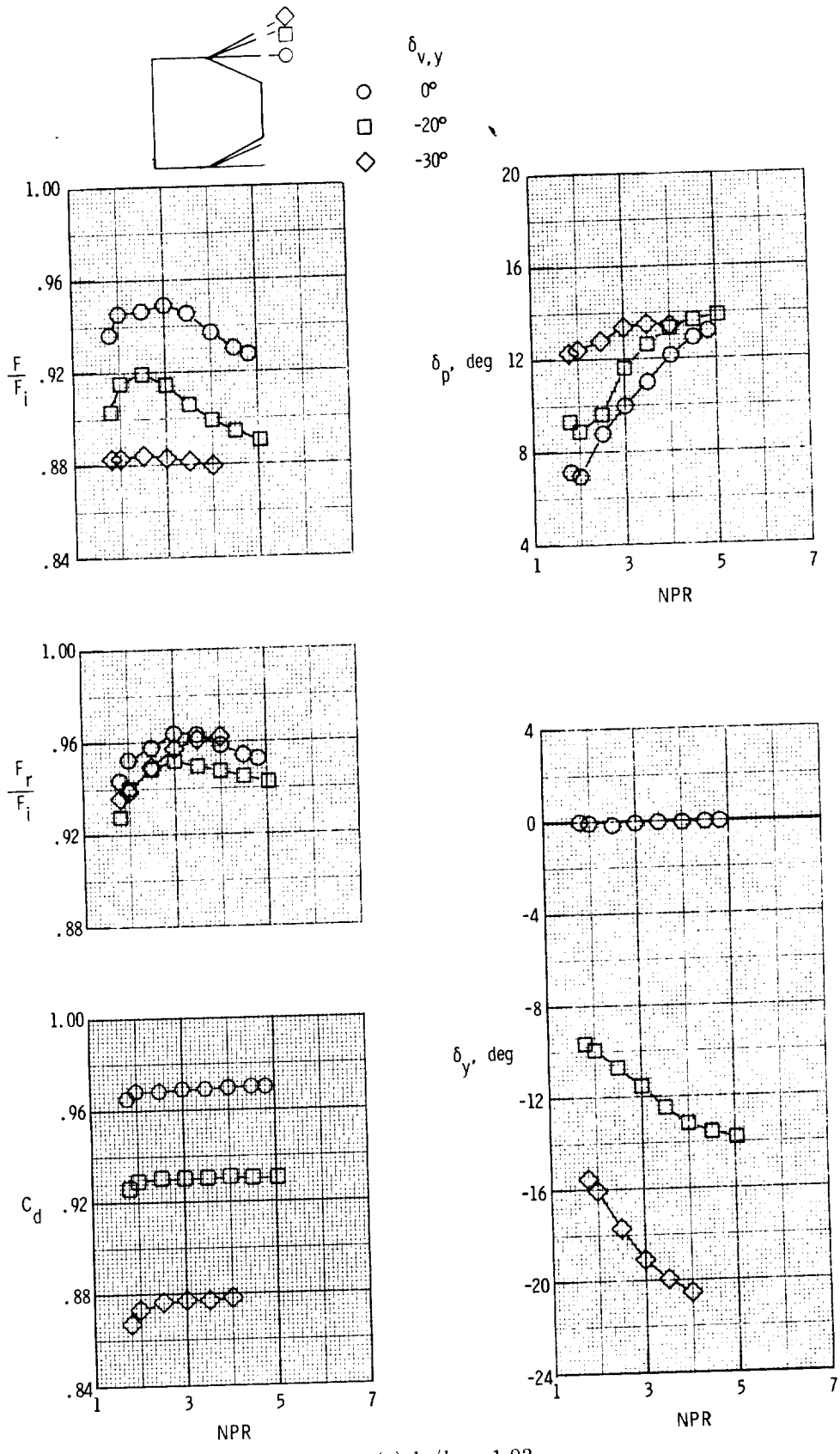

(c) $l_y/l_s = 1.03$.

Figure 25. Concluded.

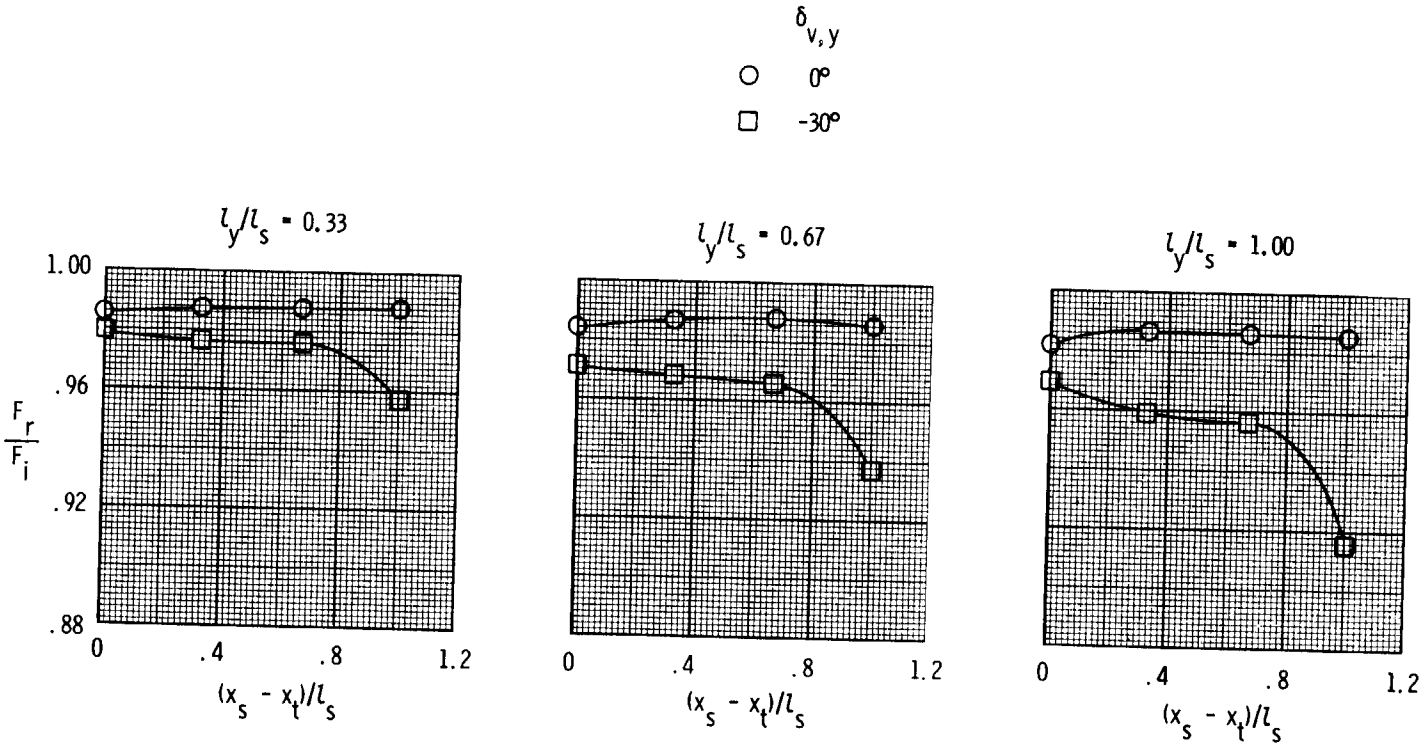

(a) $\delta_{v,p} = 0°$; NPR ≈ 3.

Figure 26. Summary of effects of yaw-flap deflection on dry power nozzle.

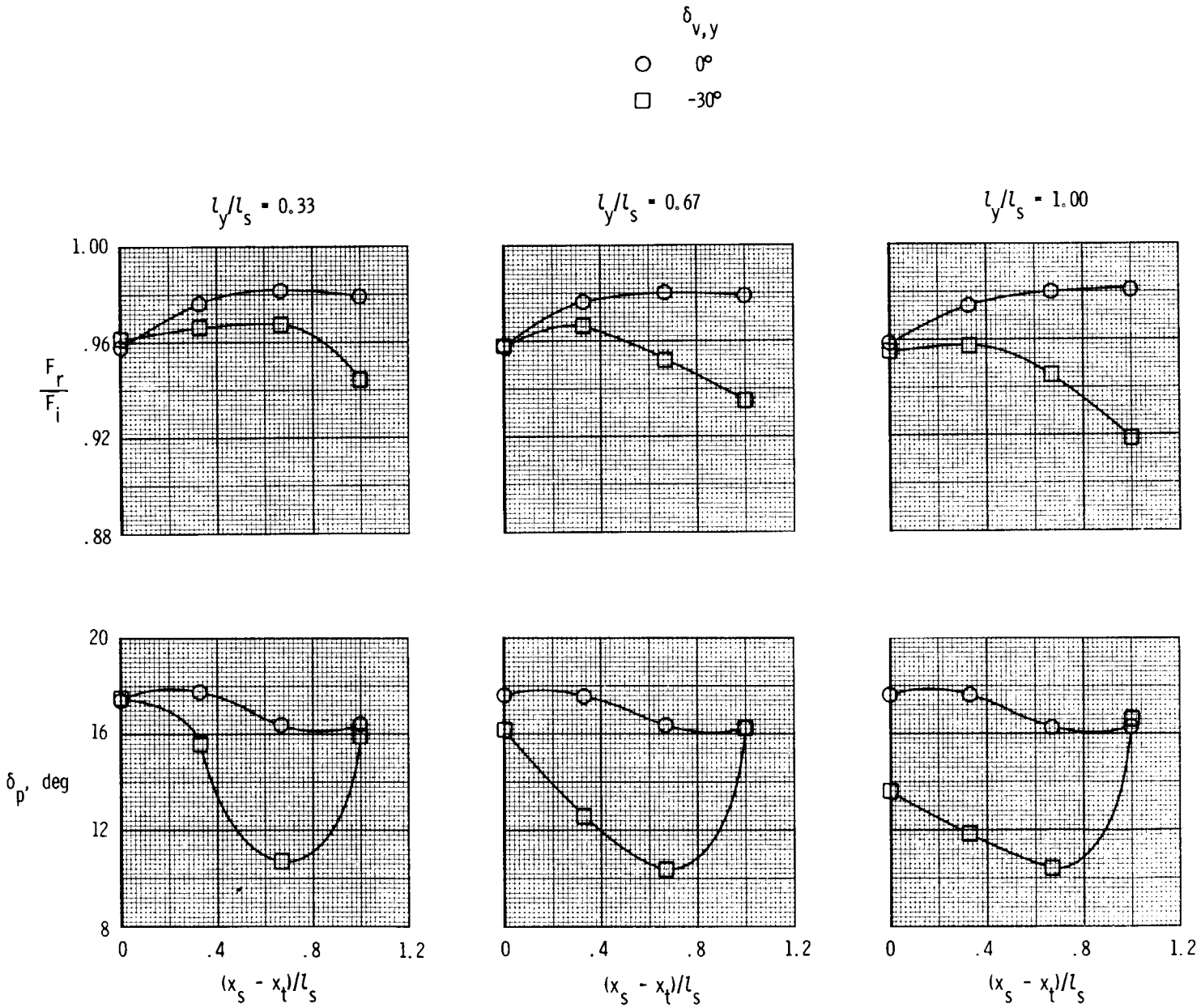

(b) $\delta_{v,p} = 19.53°$; NPR ≈ 4.

Figure 26. Concluded.

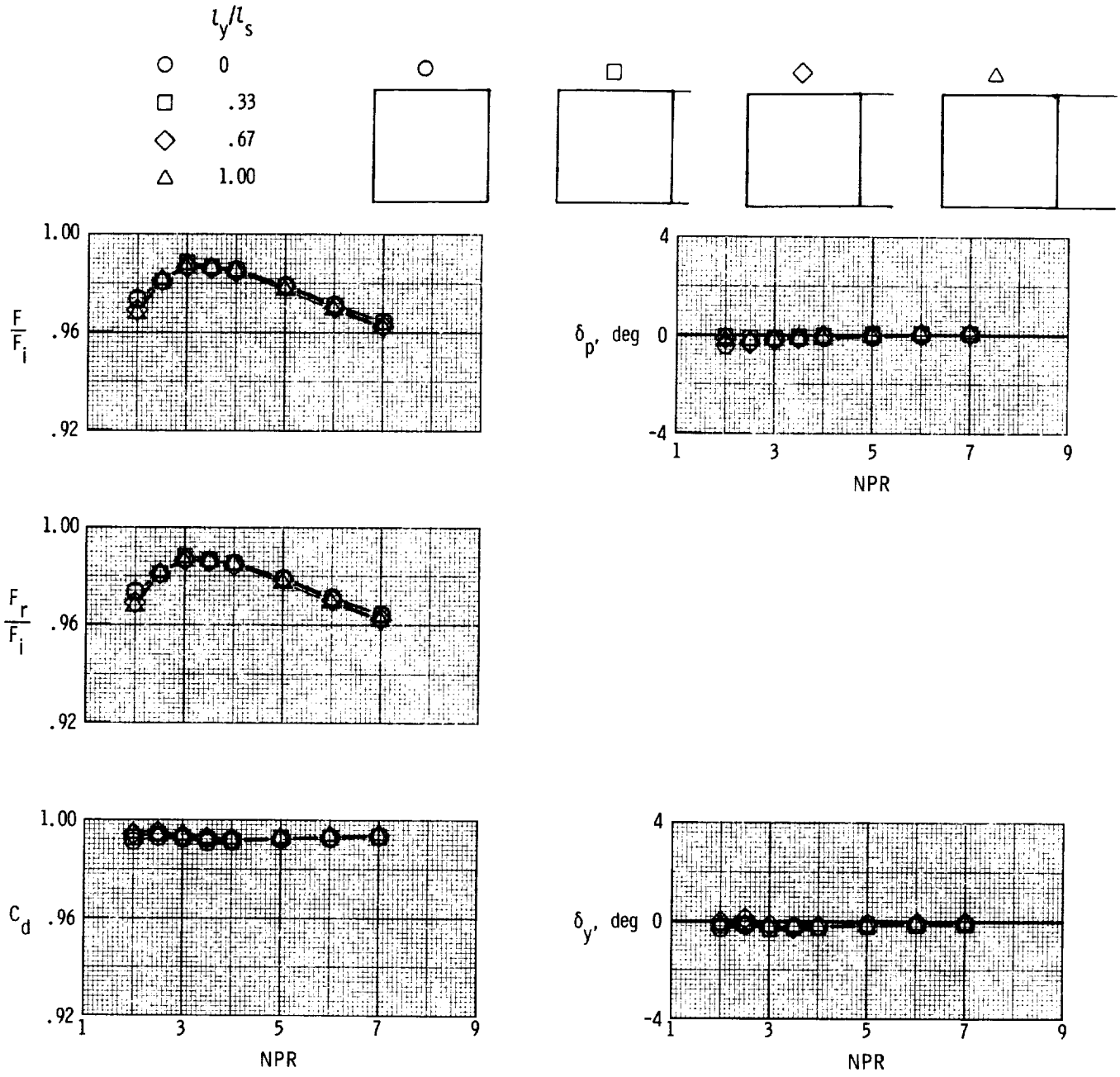

(a) Dry power; $\delta_{v,p} = 0°$.

Figure 27. Effect of undeflected yaw-flap length on nozzle internal performance characteristics for $\delta_{v,y} = 0°$ and $(x_s - x_t)/l_s = 1.00$.

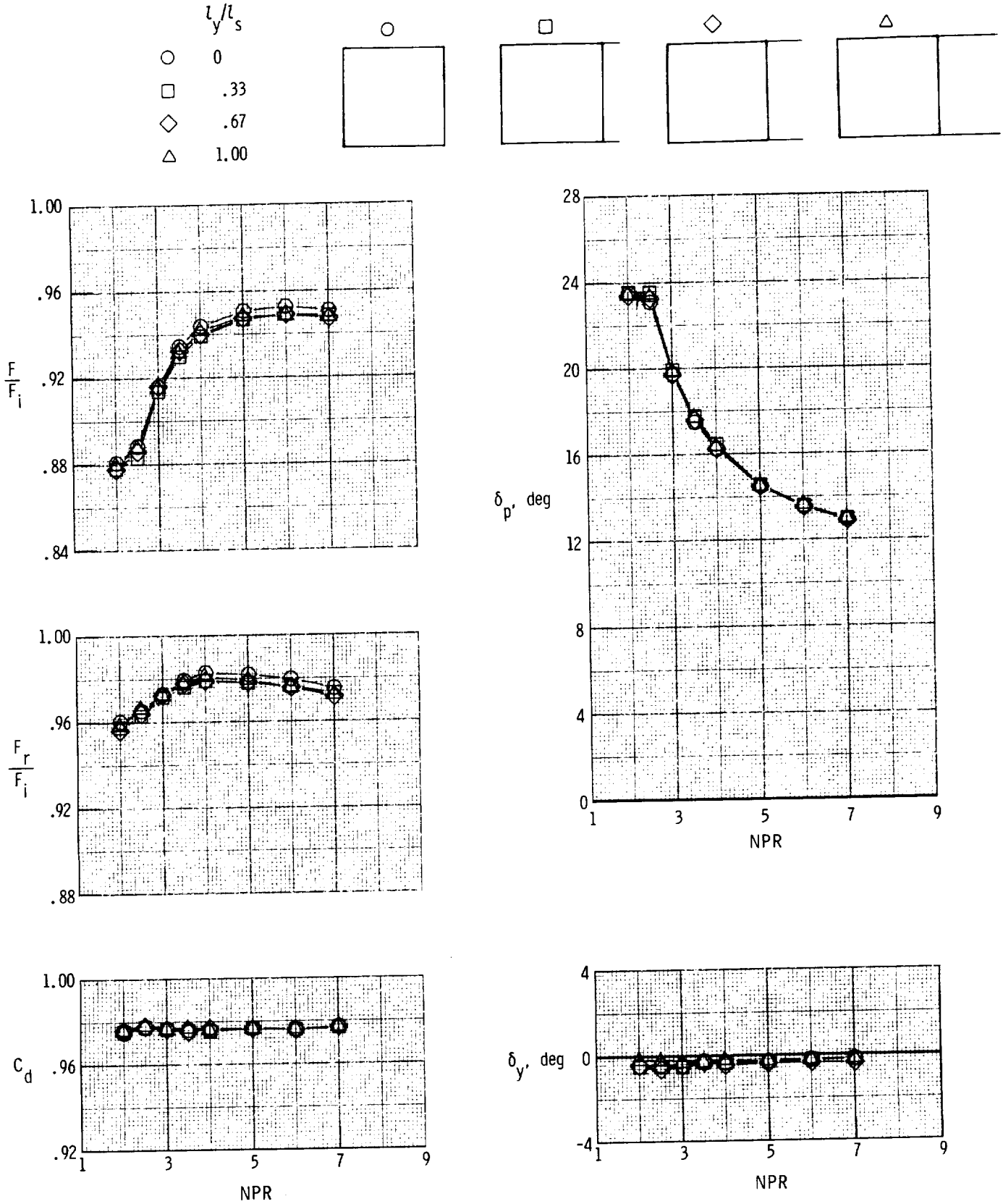

(b) Dry power; $\delta_{v,p} = 19.53°$.

Figure 27. Continued.

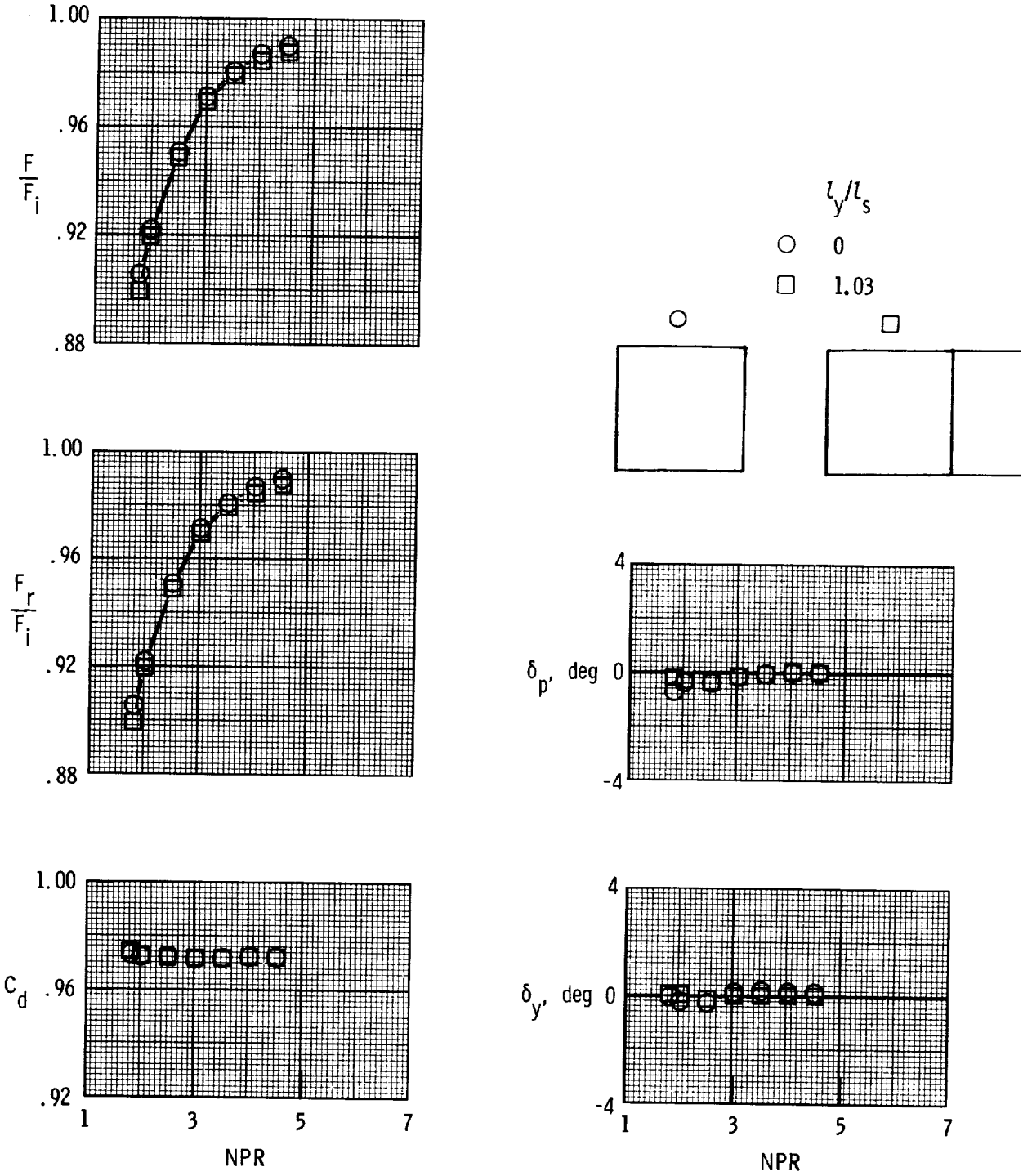

(c) A/B power; $\delta_{v,p} = 0°$.

Figure 27. Continued.

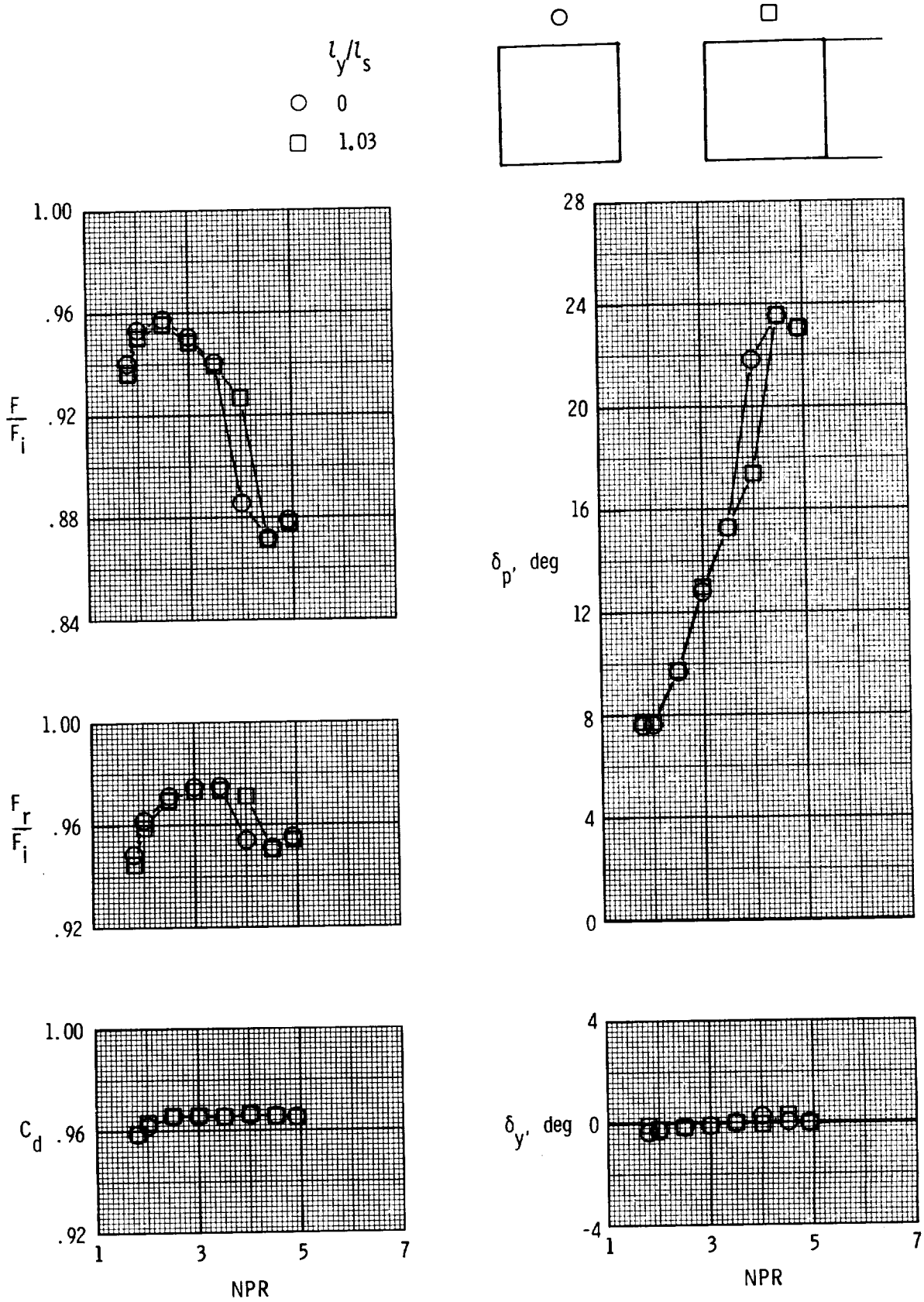

(d) A/B power; $\delta_{v,p} = 20.26°$.

Figure 27. Concluded.

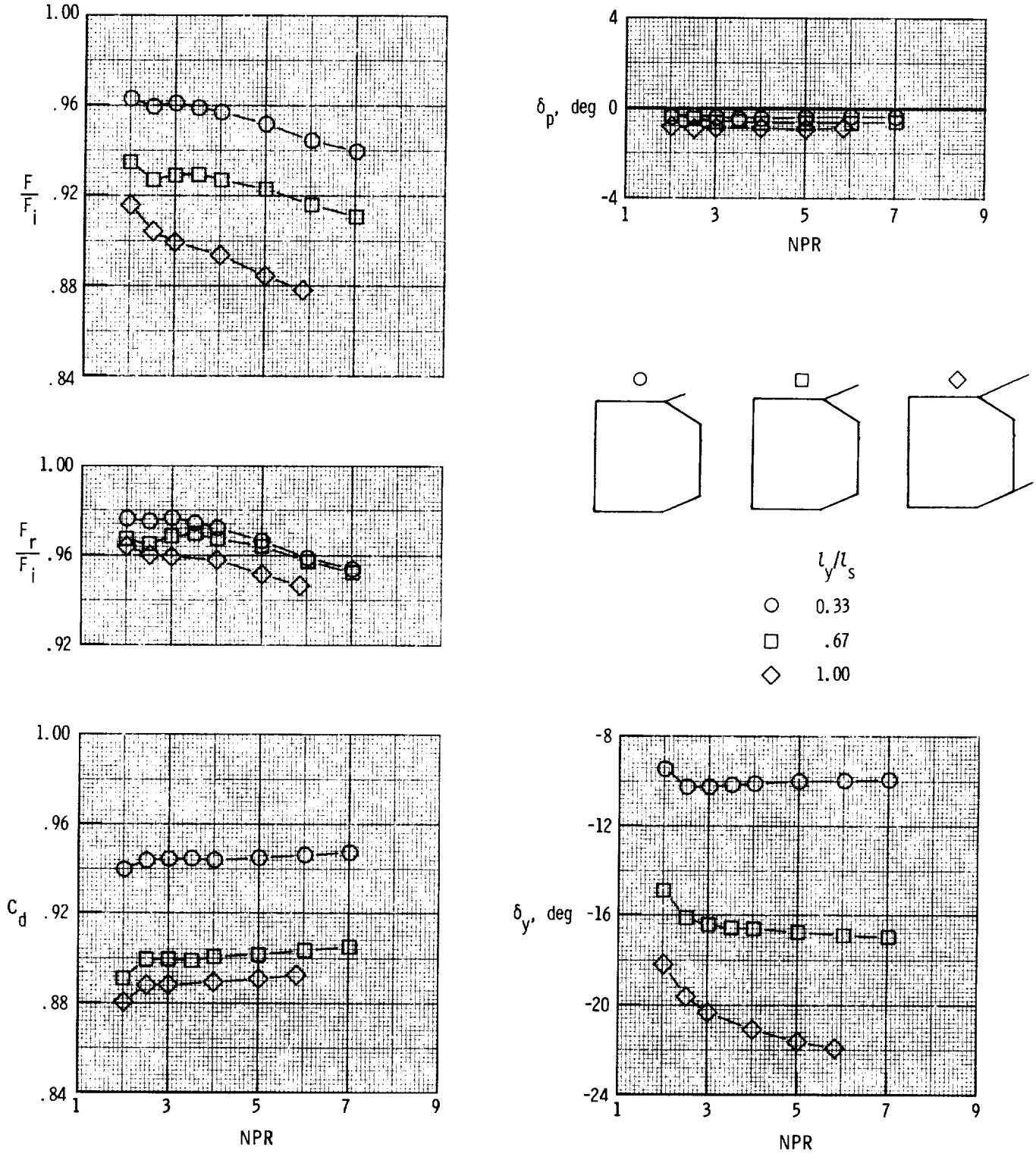

(a) Dry power; $\delta_{v,p} = 0°$; $(x_s - x_t)/l_s = 0.33$.

Figure 28. Effect of deflected yaw-flap length on nozzle internal performance characteristics for $\delta_{v,y} = -30°$.

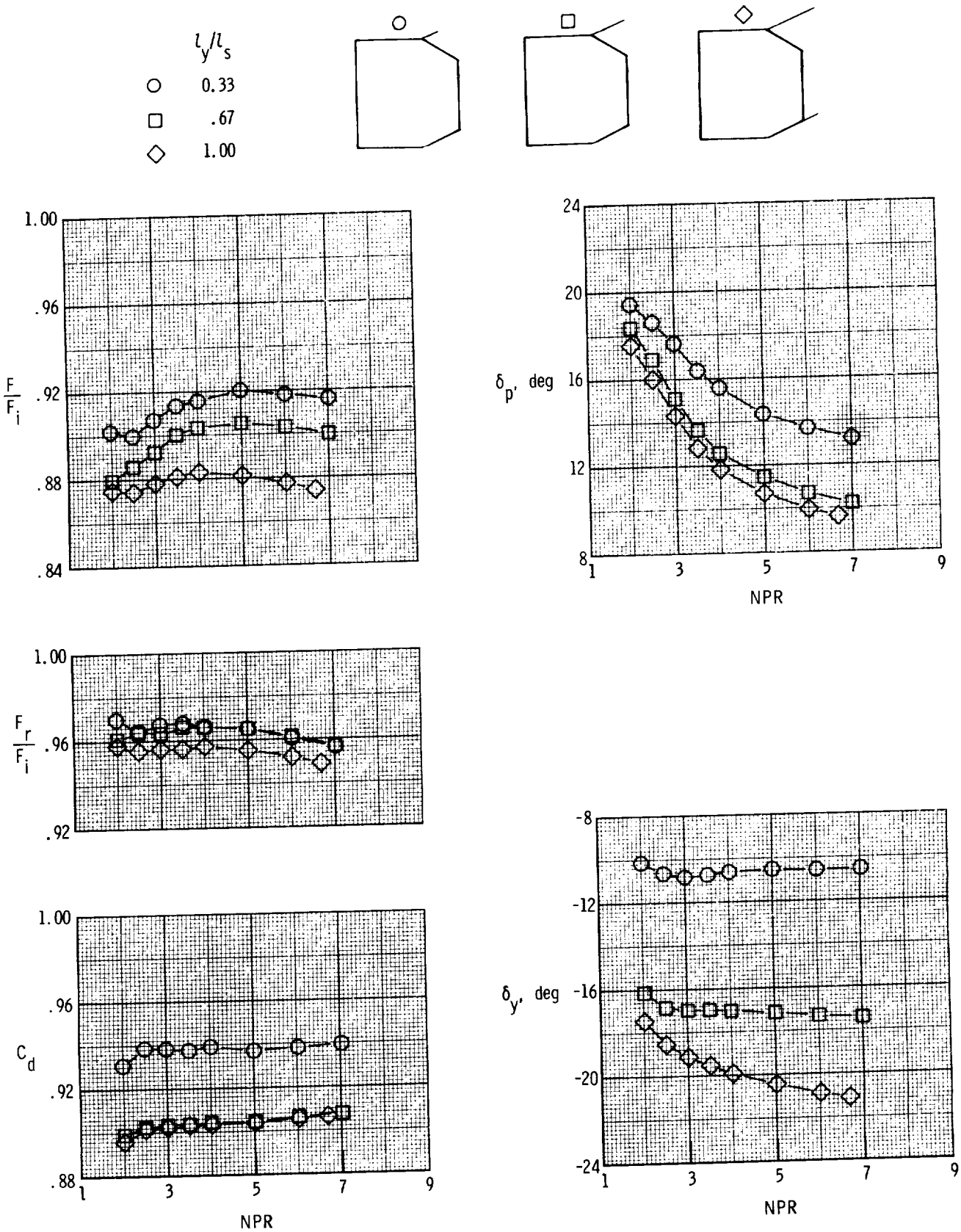

(b) Dry power; $\delta_{v,p} = 19.53°$; $(x_s - x_t)/l_s = 0.33$.

Figure 28. Continued.

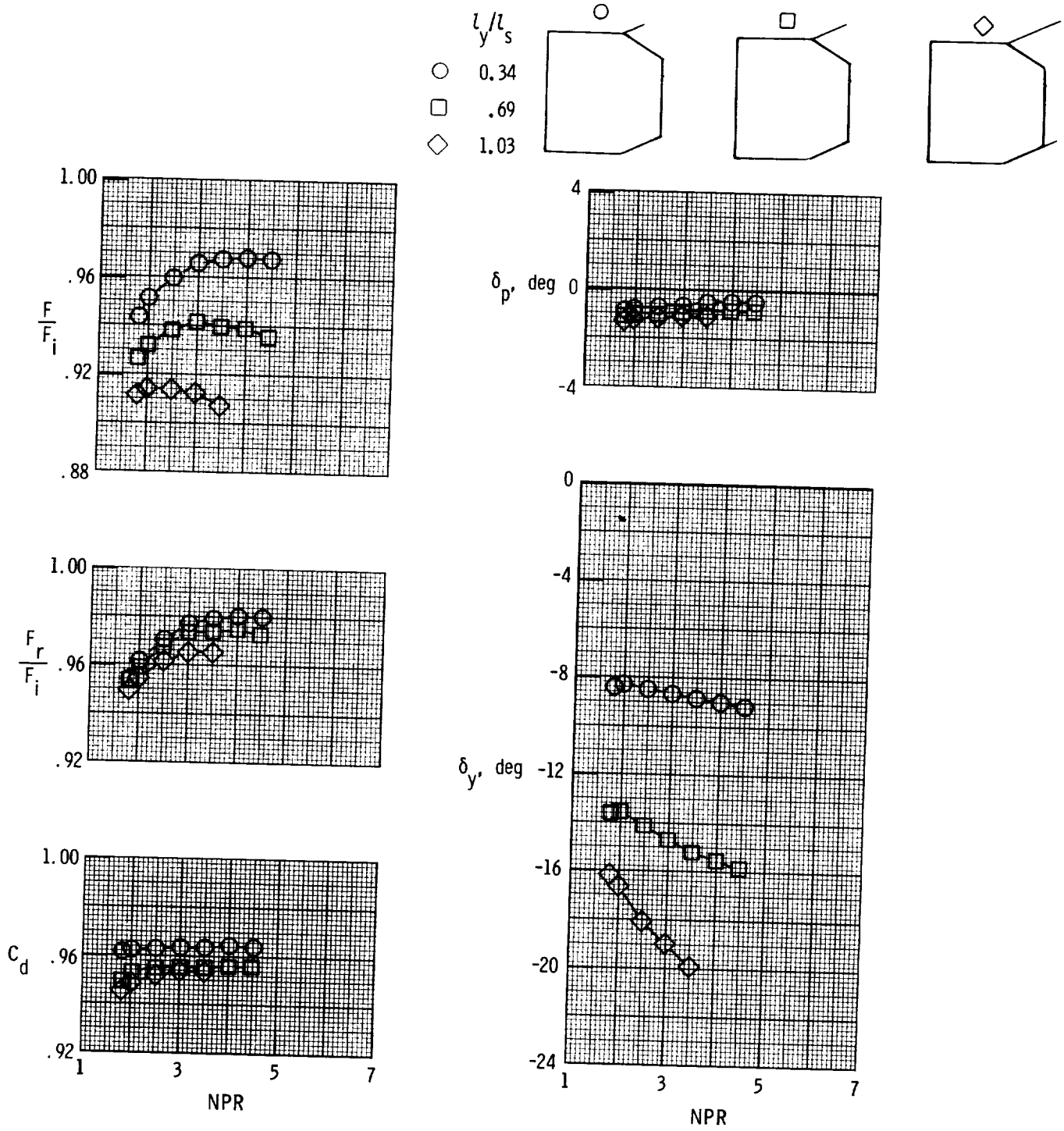

(c) A/B power; $\delta_{v,p} = 0°$; $(x_s - x_t)/l_s = 0.31$.

Figure 28. Continued.

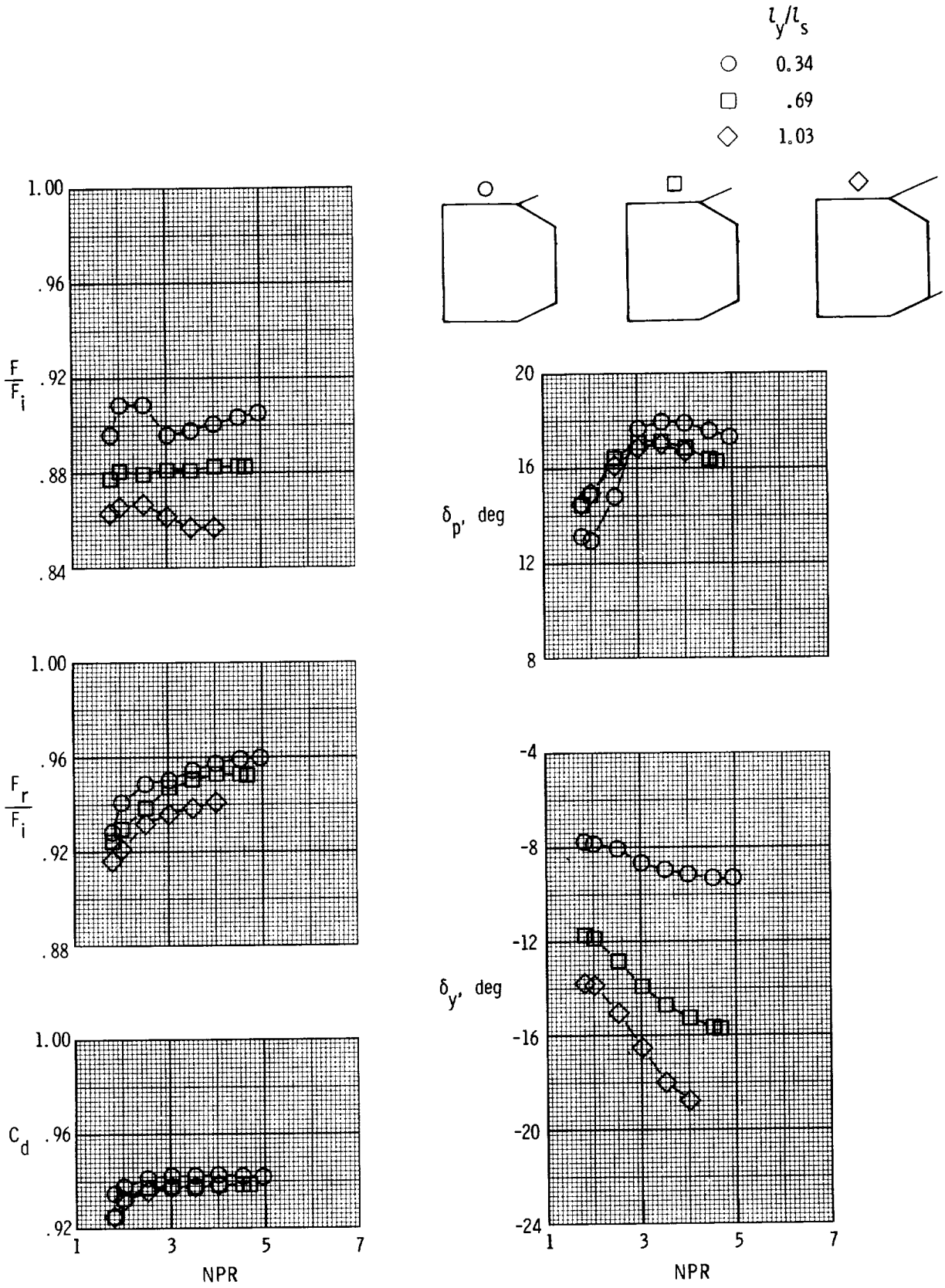

(d) A/B power; $\delta_{v,p} = 20.26°$; $(x_s - x_t)/l_s = 0.31$.

Figure 28. Concluded.

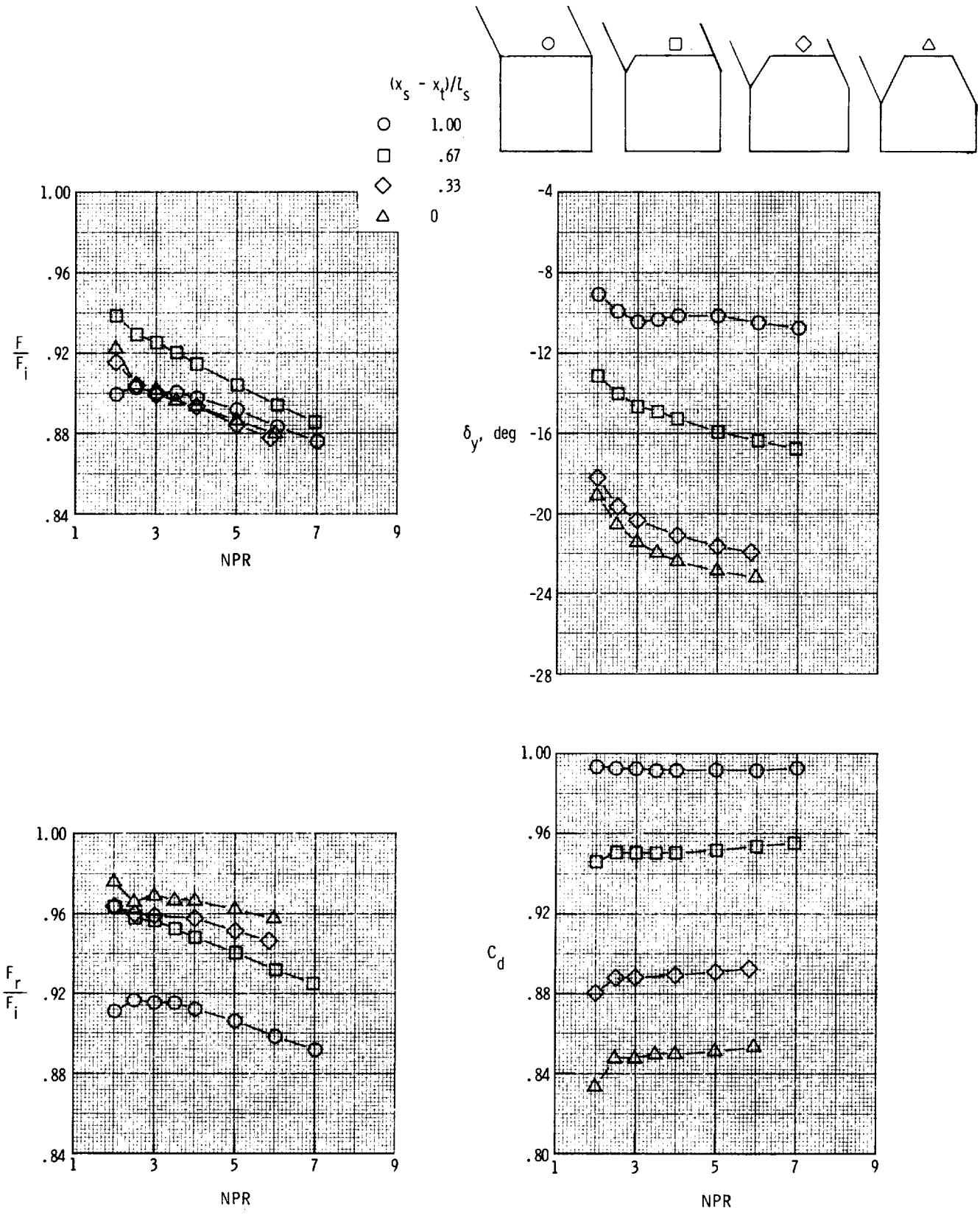

(a) Dry power; $\delta_{v,p} = 0°$; $l_y/l_s = 1.00$.

Figure 29. Effect of yaw-flap hinge location on nozzle internal performance characteristics for $\delta_{v,y} = -30°$.

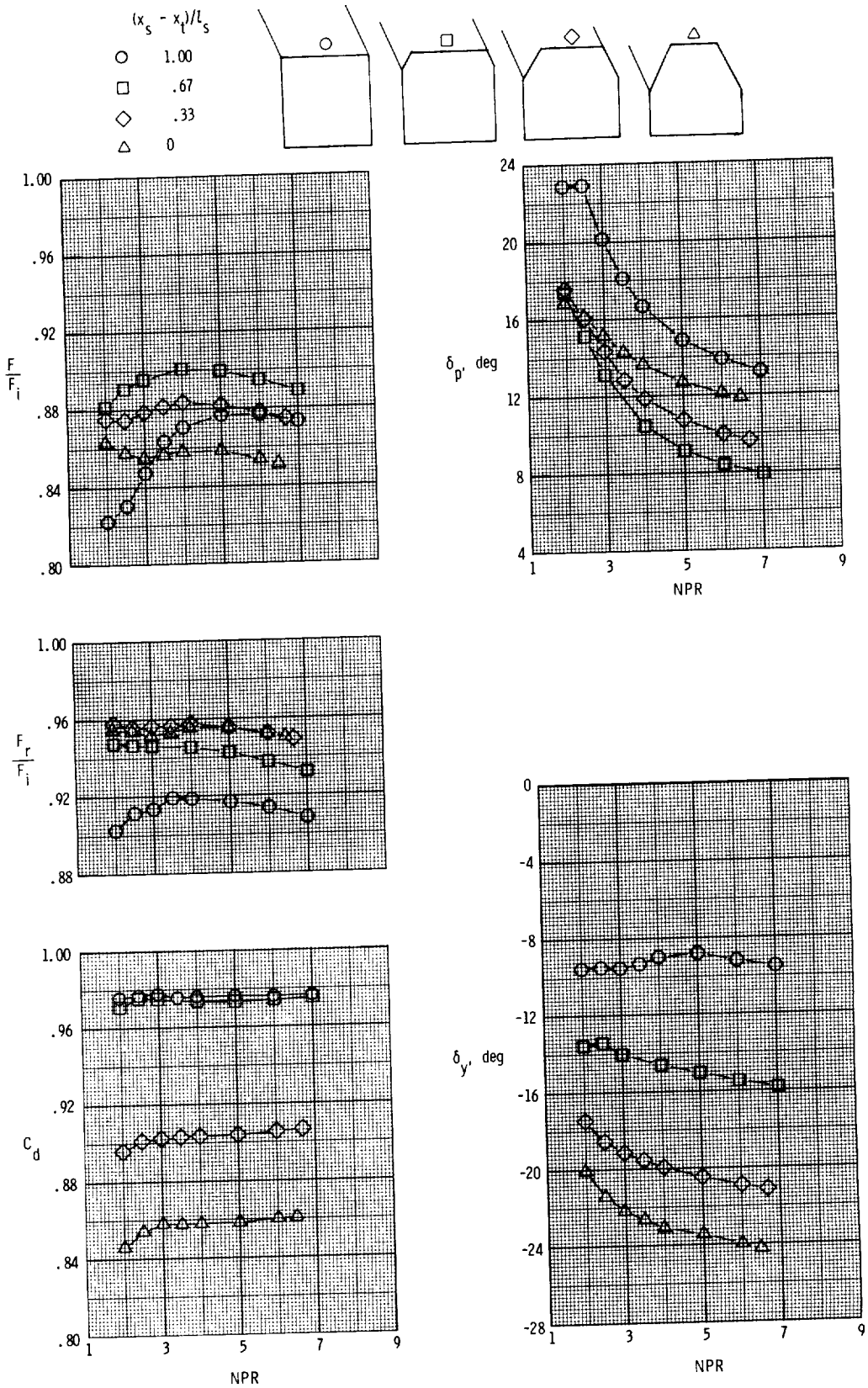

(b) Dry power; $\delta_{v,p} = 19.53°$; $l_y/l_s = 1.00$.

Figure 29. Continued.

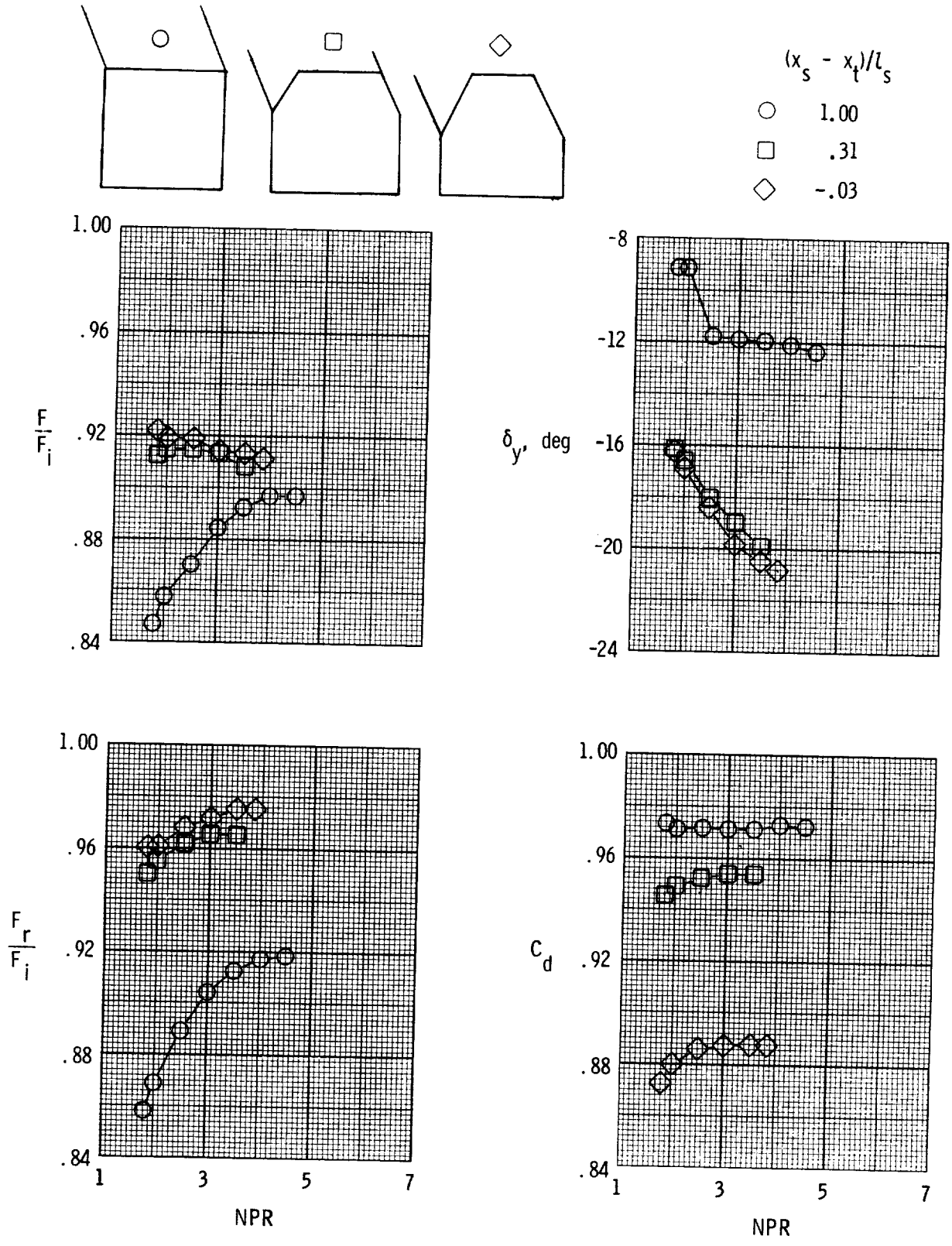

(c) A/B power; $\delta_{v,p} = 0°$; $l_y/l_s = 1.03$.

Figure 29. Continued.

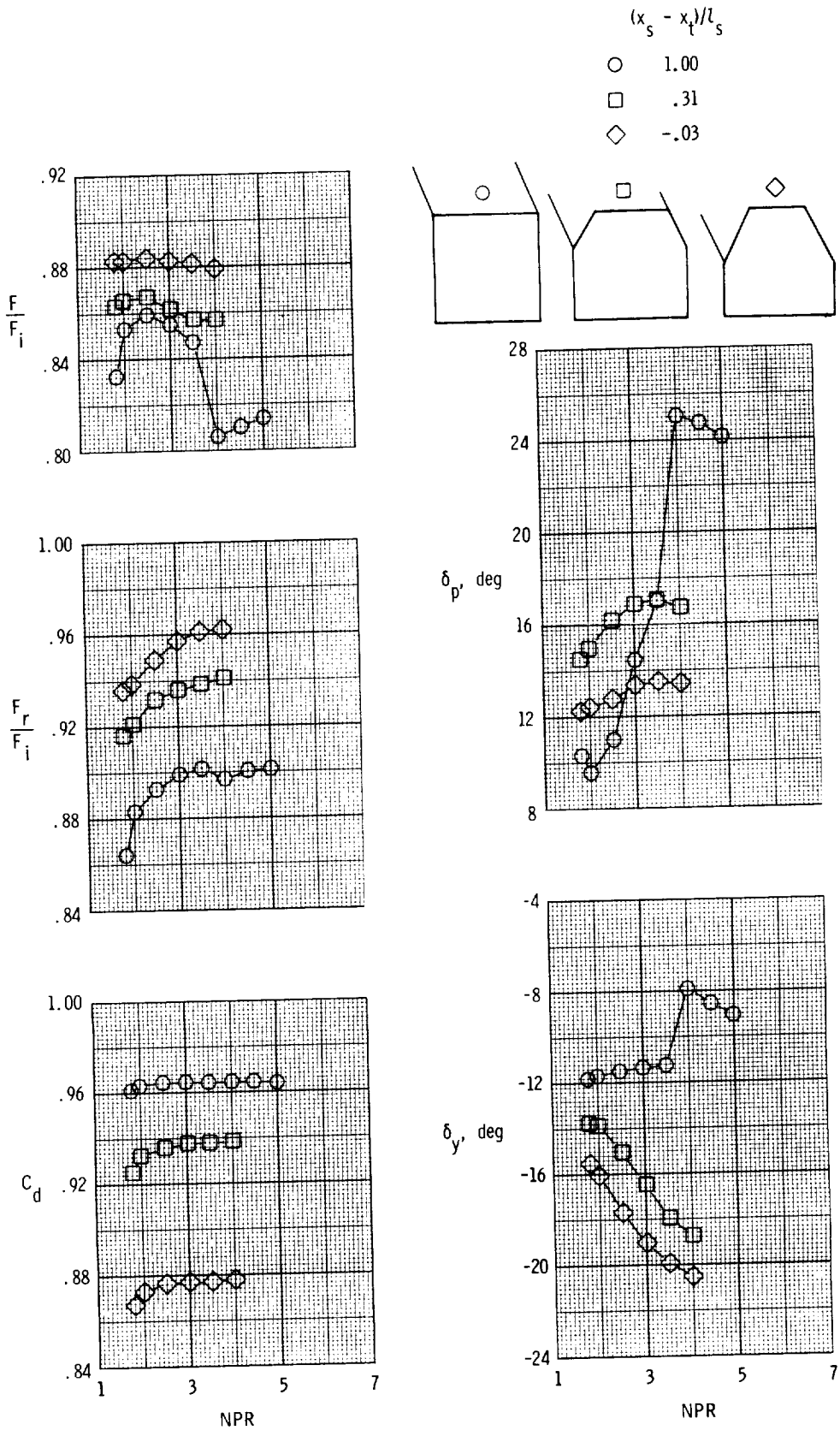

(d) A/B power; $\delta_{v,p} = 20.26°$; $l_y/l_s = 1.03$.

Figure 29. Concluded.

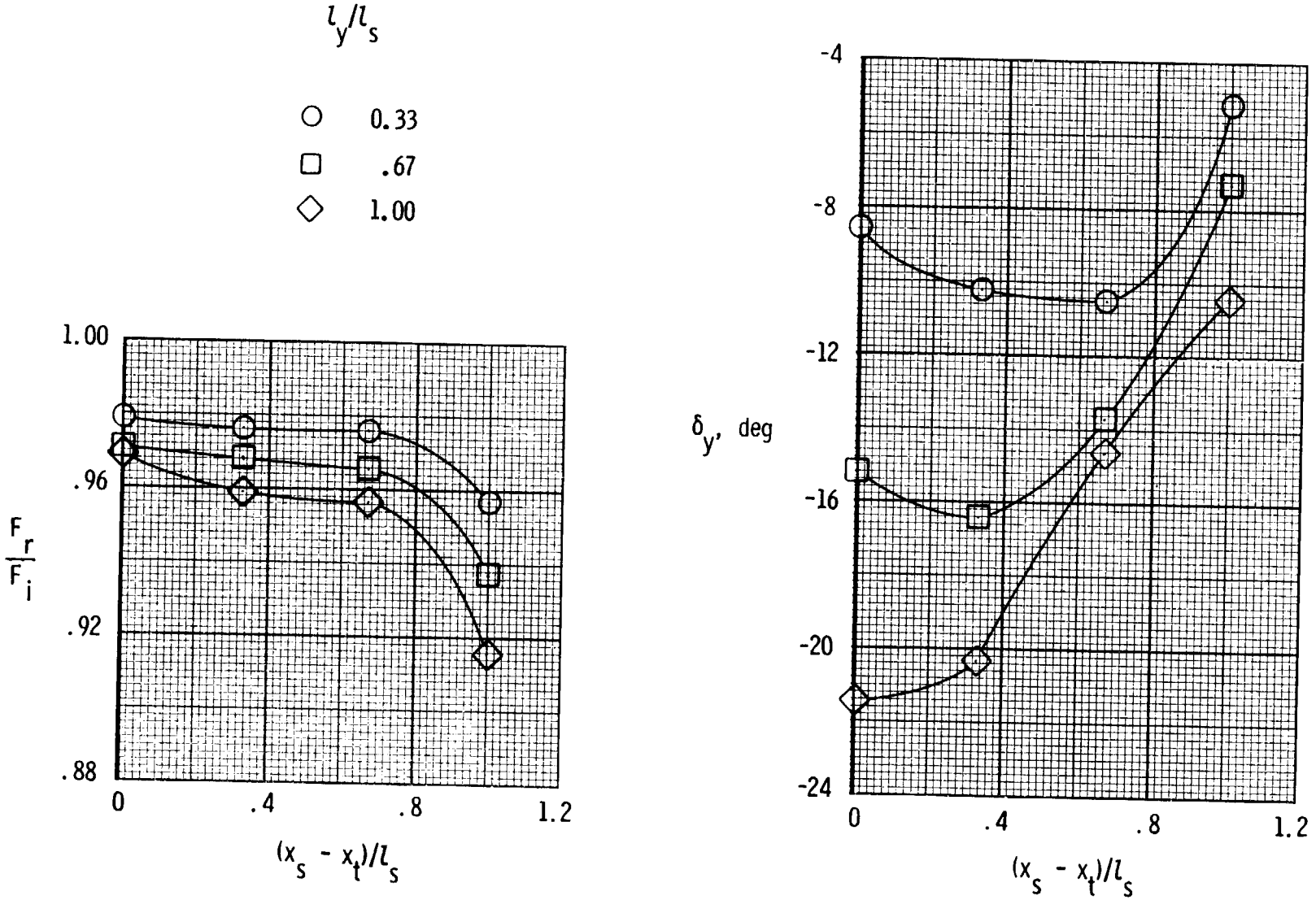

(a) Dry power; $\delta_{v,p} = 0°$; NPR ≈ 3.0.

Figure 30. Summary of effects of yaw-flap length and hinge location on nozzle internal performance characteristics for $\delta_{v,y} = -30°$.

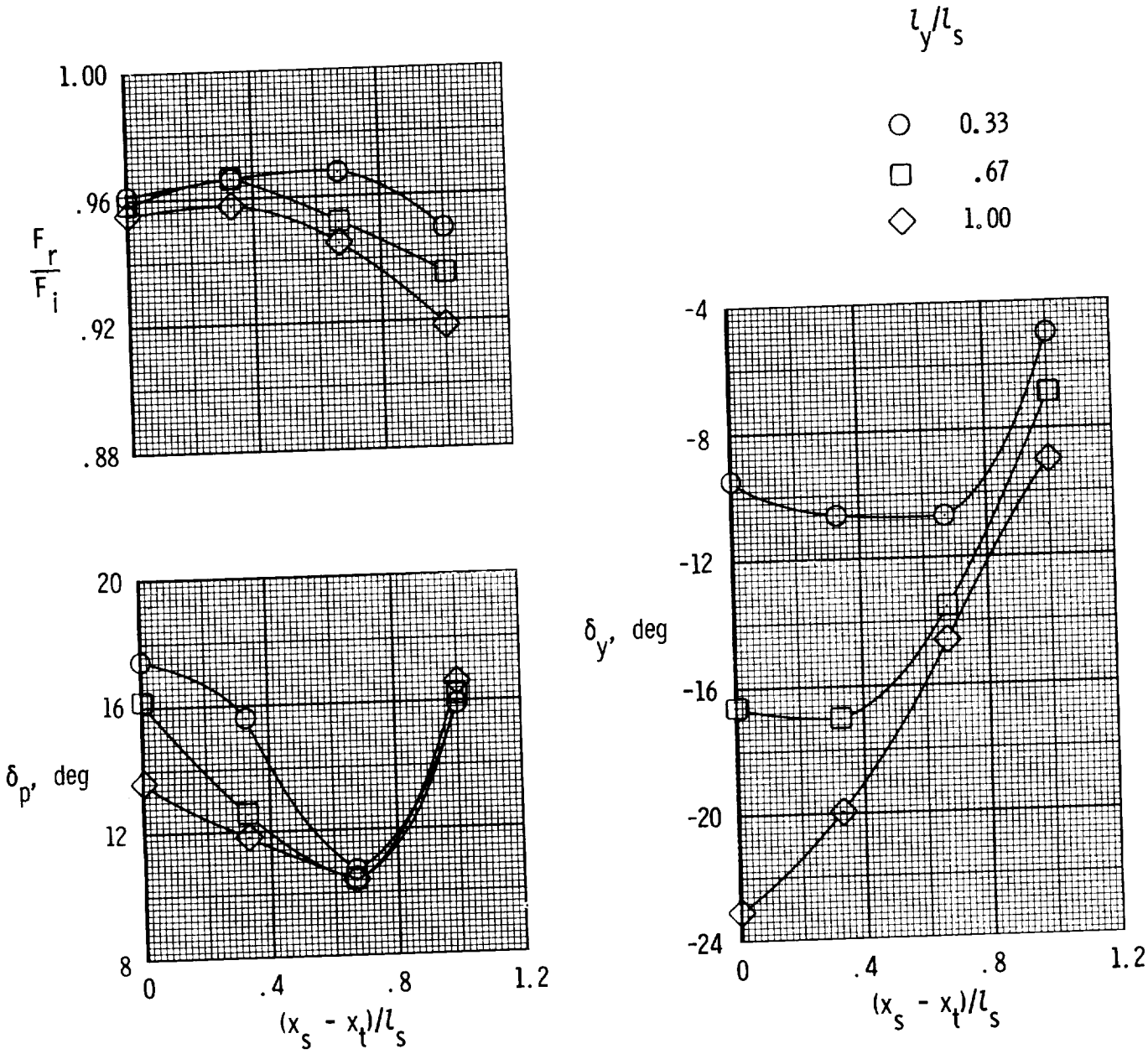

(b) Dry power; $\delta_{v,p} = 19.53°$; NPR ≈ 4.0.

Figure 30. Continued.

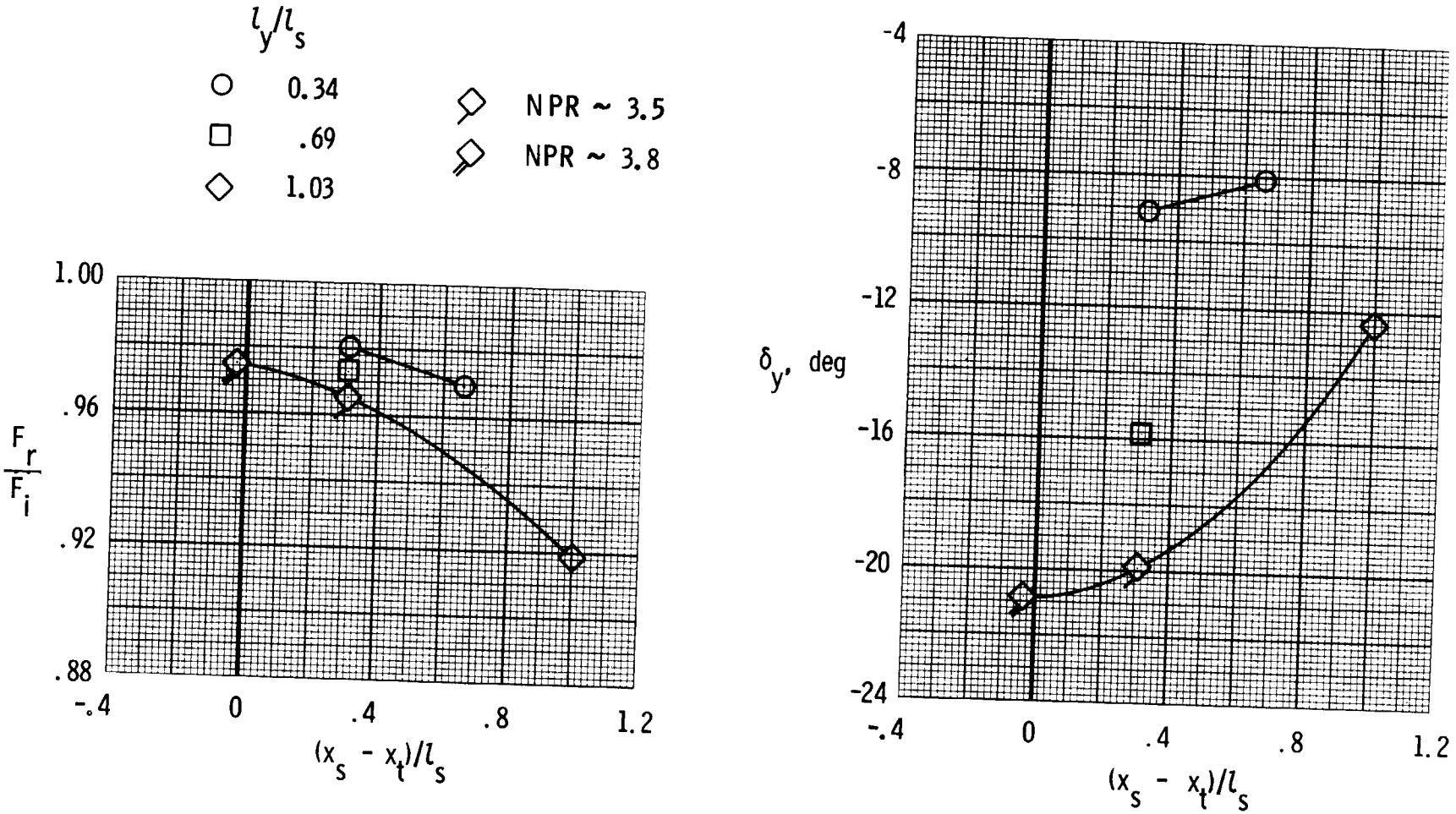

(c) A/B power; $\delta_{v,p} = 0°$; NPR ≈ 4.5.

Figure 30. Continued.

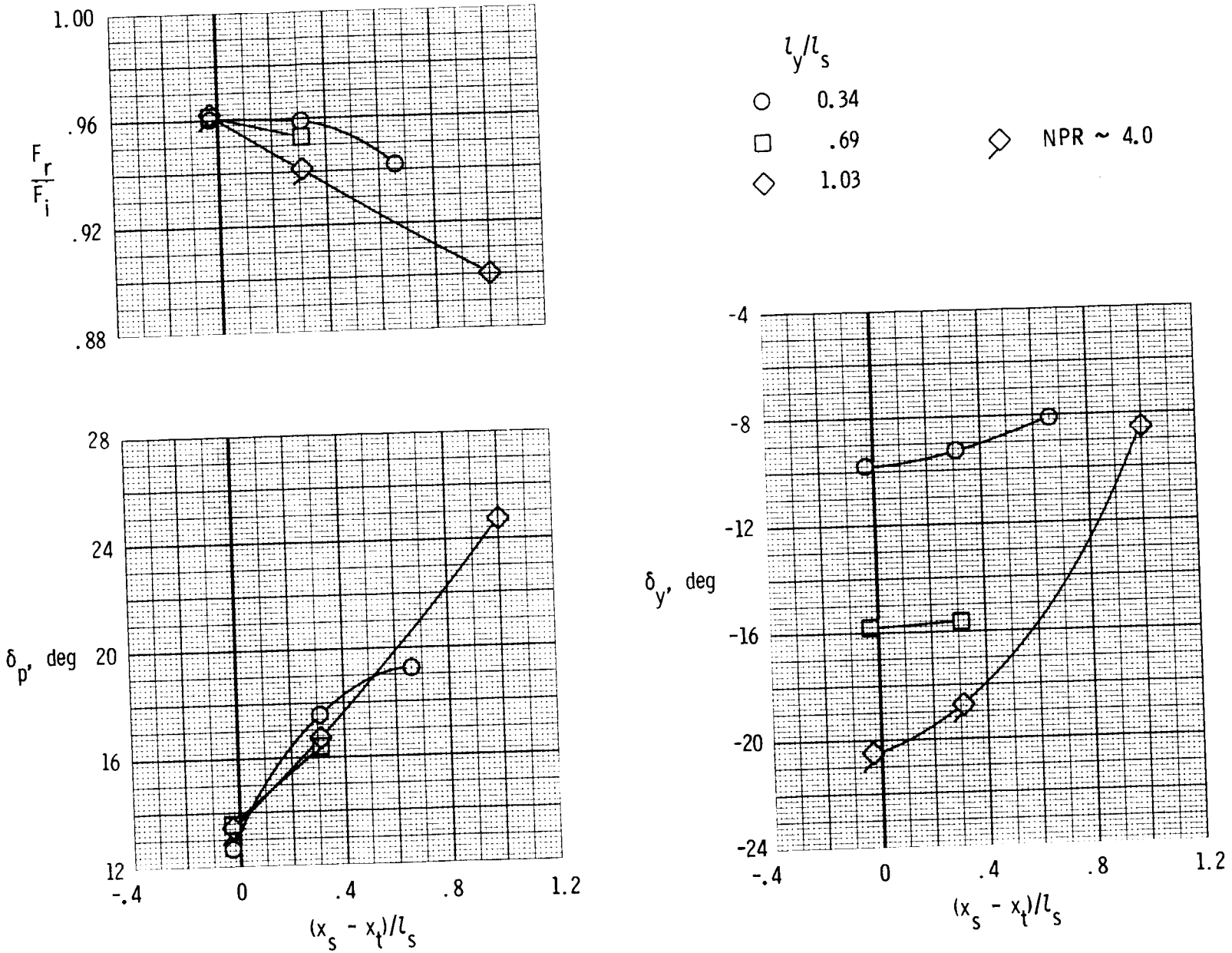

(d) A/B power; $\delta_{v,p} = 20.26°$; NPR ≈ 4.5.

Figure 30. Concluded.

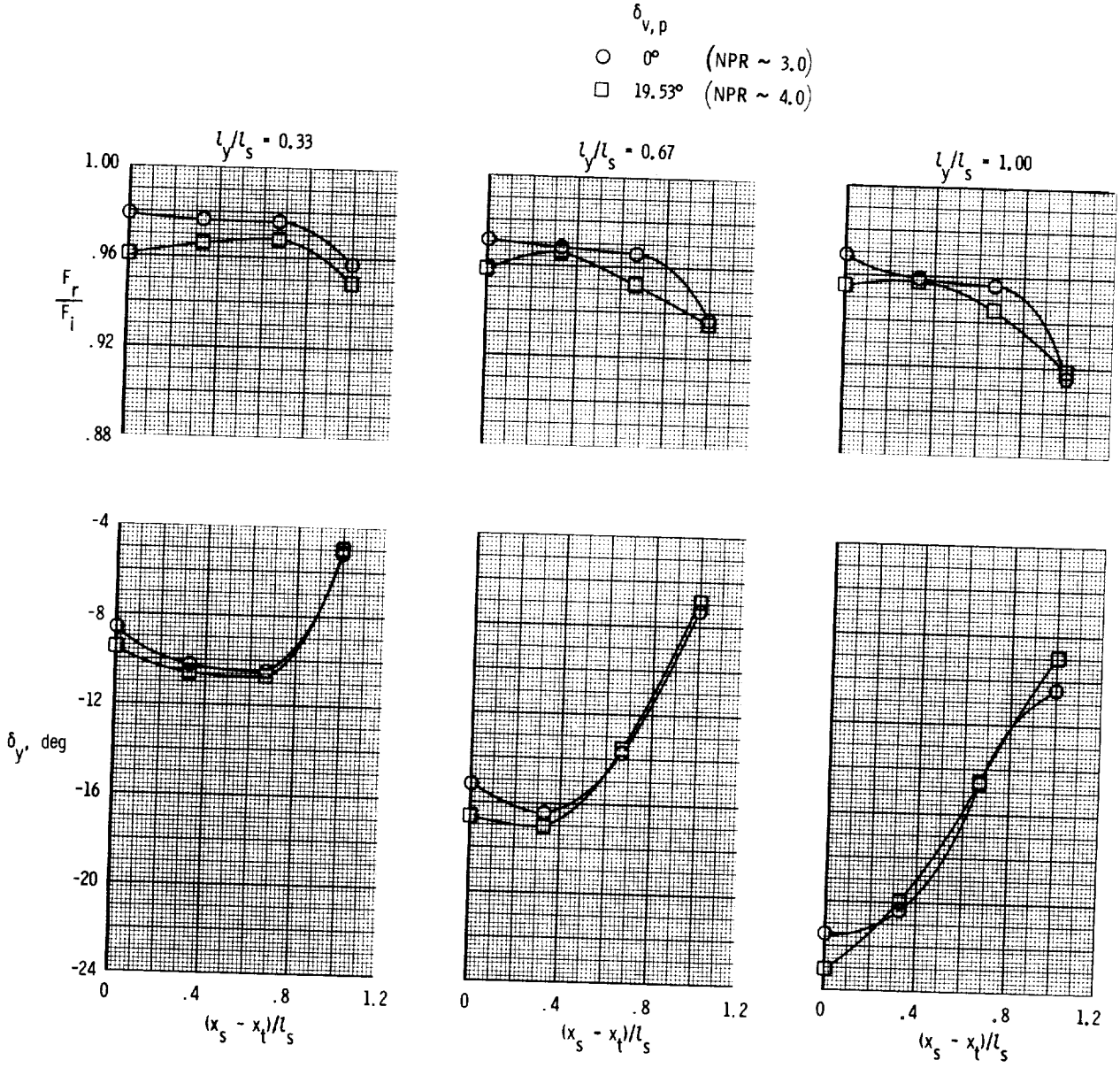

(a) Dry power.

Figure 31. Effect of pitch thrust vectoring on nozzle internal performance characteristics for $\delta_{v,y} = -30°$ and NPR ≈ 4.5 unless otherwise indicated.

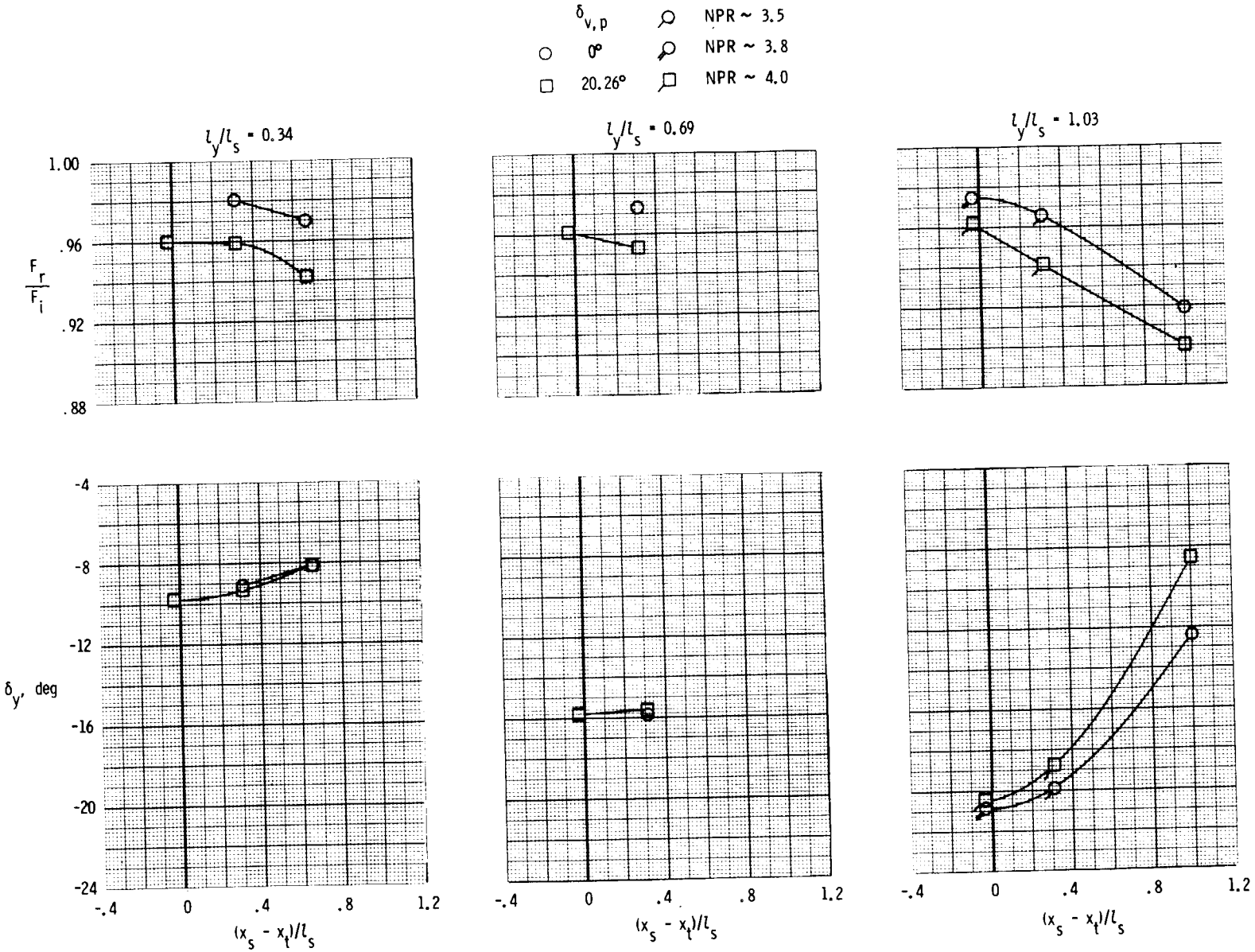

(b) A/B power; NPR ≈ 4.5.

Figure 31. Concluded.

Previous concepts; NPR near design						
Symbol	δ_y effector	$\delta_{v,y}$, deg	Power setting	Approx. AR	Reference	Comments
○	Round port	± 5.9	Dry	3.7	13	Conf. P1
□	1 powered rudder	± 20	↓	3.7	13	Conf. R4
◇	2 post-exit flaps	↓	↓	4.6	17	Vane V1
△	2 downstream flaps	↓	↓	3.7	13	Conf. F6
◺	2 downstream flaps	↓	A/B	2.8	14	
◺	Div. flaps (of canted nozzles)	↓	Dry	3.5	15	Conf. 3 (Dihedral angle = 45°)

Current test; $\delta_{v,y}$ = -30°; dry power; AR ≈ 3.9			
Symbol	δ_y effector	$(x_s - x_t)/l_s$	l_y/l_s
●	2 post-exit flaps	1.00	0.33
■	2 post-exit flaps	1.00	.67
◆	2 post-exit flaps	1.00	1.00
▲	2 sidewall flaps	.67	.33
◣	2 sidewall flaps	.33	.67
◣	2 sidewall flaps	0	1.00

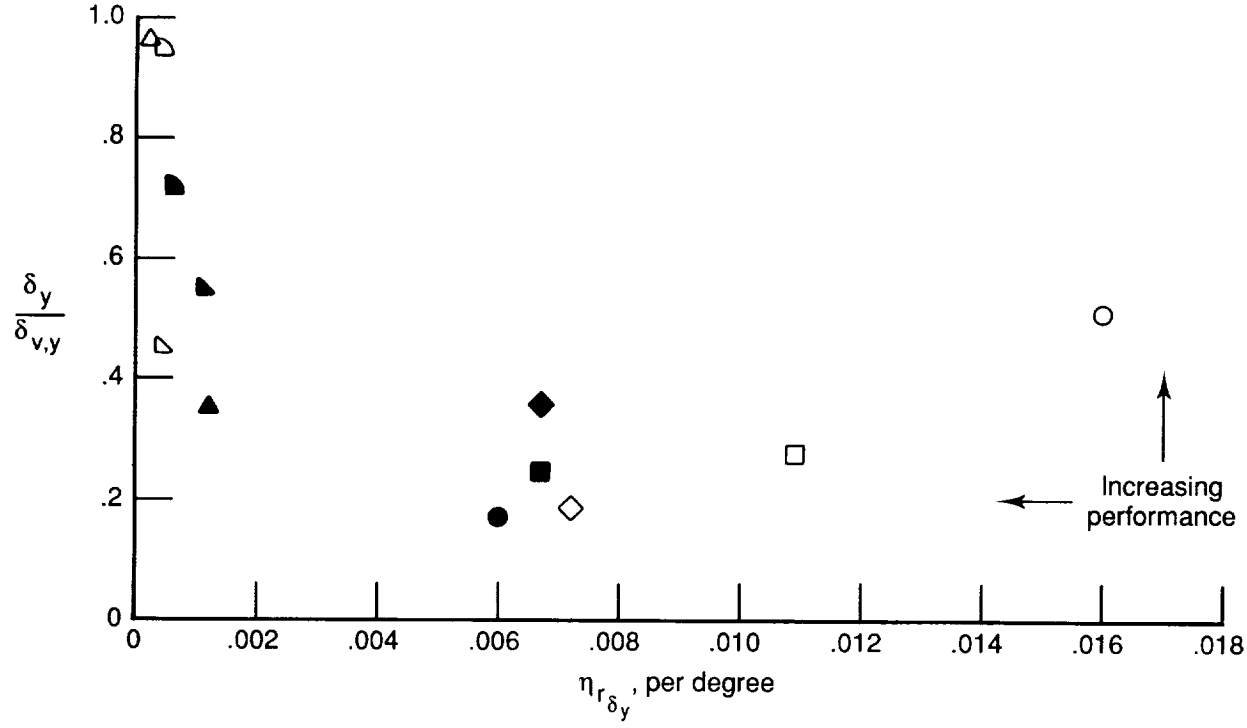

Figure 32. Comparison of yaw thrust-vectoring concepts of 2-D C-D nozzle at an NPR near design. Yaw-vectoring efficiency is given as function of vectoring performance-effectiveness parameter.

Previous concepts; NPR near design								
Symbol	δ_p effector	$\delta_{v,p}$, deg	δ_y effector	$\delta_{v,y}$, deg	Power setting	Approx. AR	Reference	Comments
○	Div. flaps	± 20.3	Round port	± 5.3	A/B	2.0	13	Conf. P16
□	Div. flaps	± 20.3	1 powered rudder	± 20	A/B	2.0	13	Conf. R16
◇	Conv./div. flaps	± 11.7	2 post-exit flaps	↓	Dry	4.0	17	Vane V1
△	Div. flaps	± 20.3	1 downstream flap	↓	A/B	2.0	13	Conf. F23
◺	Conv./div. flaps	± 15	2 downstream flaps	↓	A/B	2.3	14	
◺	Div. flaps (of canted nozzles)	± 14.1	Div. flaps (of canted nozzles)	± 14.1	Dry	3.5	15	(a)

[a] Conf. 3 (Dihedral angle = 45°; twin engine; single nozzle deffection of 20°).

Current test; dry power; AR ≈ 3.9						
Symbol	δ_p effector	$\delta_{v,p}$, deg	δ_y effector	$\delta_{v,y}$, deg	$(x_s - x_t)/l_s$	l_y/l_s
●	Div. flaps	± 19.5	2 yaw flaps	± 30	1.00	0.33
■	↓	↓	↓	↓	1.00	.67
◆	↓	↓	↓	↓	1.00	1.00
▲	↓	↓	↓	↓	.67	.33
◣	↓	↓	↓	↓	.33	.67
◣	↓	↓	↓	↓	0	1.00

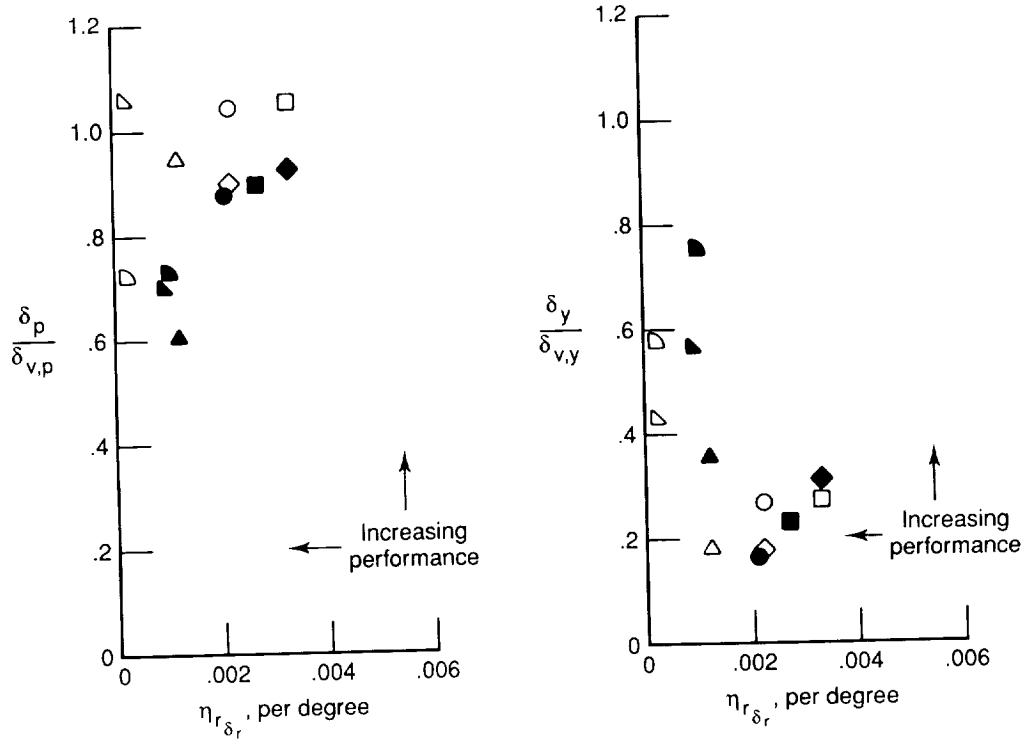

Figure 33. Comparison of multiaxis thrust-vectoring concepts of 2-D C-D nozzle at an NPR near design. Pitch and yaw thrust-vectoring efficiency is given as function of vectoring performance-effectiveness parameter.

NASA
National Aeronautics and Space Administration

Report Documentation Page

1. Report No.	2. Government Accession No.	3. Recipient's Catalog No.
NASA TP-2973		

4. Title and Subtitle	5. Report Date
Static Investigation of a Two-Dimensional Convergent-Divergent Exhaust Nozzle With Multiaxis Thrust-Vectoring Capability	April 1990
	6. Performing Organization Code
7. Author(s)	8. Performing Organization Report No.
John G. Taylor	L-16632
9. Performing Organization Name and Address	10. Work Unit No.
NASA Langley Research Center Hampton, VA 23665-5225	505-62-71-01
	11. Contract or Grant No.
12. Sponsoring Agency Name and Address	13. Type of Report and Period Covered
National Aeronautics and Space Administration Washington, DC 20546-0001	Technical Paper
	14. Sponsoring Agency Code

15. Supplementary Notes

16. Abstract

An investigation has been conducted in the static test facility of the Langley 16-Foot Transonic Tunnel to determine the internal performance of two-dimensional convergent-divergent nozzles designed to have simultaneous pitch and yaw thrust-vectoring capability. This concept utilized divergent flap rotation of thrust vectoring in the pitch plane and deflection of flat yaw flaps hinged at the end of the sidewalls for yaw thrust vectoring. The hinge location of the yaw flaps was varied at four positions from the nozzle exit plane to the throat plane. The yaw flaps were designed to contain the flow laterally independent of power setting. In order to eliminate any physical interference between the yaw flap deflected into the exhaust stream and the divergent flaps, the downstream corners of both upper and lower divergent flaps were cut off to allow for up to 30° of yaw-flap deflection. This investigation studied the impact of varying the nozzle pitch vector angle, throat area, yaw-flap hinge location, yaw-flap length, and yaw-flap deflection angle on nozzle internal performance characteristics. High-pressure air was used to simulate the jet exhaust at nozzle pressure ratios up to 7.0.

17. Key Words (Suggested by Authors(s))	18. Distribution Statement
Nonaxisymmetric nozzles Multiaxis thrust vectoring Static internal performance Two-dimensional convergent-divergent nozzles	Unclassified—Unlimited Subject Category 02

19. Security Classif. (of this report)	20. Security Classif. (of this page)	21. No. of Pages	22. Price
Unclassified	Unclassified	102	A06

NASA FORM 1626 OCT 86

For sale by the National Technical Information Service, Springfield, Virginia 22161-2171

NASA-Langley, 1990